Reduced contribution of sulfur to the mass extinction associated with the Chicxulub impact event

This preprint posted on EarthArXiv was submitted to Nature Communications 23 April 2024 and is currently under review.

Author Information

Katerina Rodiouchkina[1,2,3], Steven Goderis[2], Cem Berk Senel[2,4], Pim Kaskes[2,5], Özgür Karatekin[4], Orkun Temel[4,6], Michael Ernst Böttcher[7,8,9], Ilia Rodushkin[3,10], Johan Vellekoop[11,12], Philippe Claeys[2], Frank Vanhaecke[1]

Affiliations

[1] Atomic and Mass Spectrometry – A&MS research unit, Department of Chemistry, Ghent University, Ghent, Belgium

[2] Archaeology, Environmental Changes & Geo-Chemistry, Vrije Universiteit Brussel, Brussels, Belgium

[3] Division of Geosciences, Luleå University of Technology, Luleå, Sweden

[4] Reference Systems and Planetology Department, Royal Observatory of Belgium, Uccle, Belgium

[5] Laboratoire G-Time, Université Libre de Bruxelles, 1050 Brussels, Belgium

[6] Institute of Astronomy, KU Leuven, Leuven, Belgium

[7] Geochemistry & Isotope Biogeochemistry, Leibniz-Institute for Baltic Sea Research Warnemünde, Rostock, Germany

[8] Marine Geochemistry, Greifswald University, Germany

[9] Interdisciplinary Faculty, University of Rostock, Germany

[10] ALS Scandinavia AB, ALS Laboratory Group, Luleå, Sweden

[11] Department of Geology, KU Leuven, Leuven, Belgium

[12] Institute for Natural Sciences, Brussels, Belgium

Corresponding author: Katerina Rodiouchkina (Katerina.Rodiouchkina@ltu.se)

Author contributions

K.R led the writing of the manuscript in close partnership with S.G. S.G was responsible for the conceptualization, selecting the samples of interest, and main supervision of the study. F.V contributed to the supervision of the study and was responsible for the project administration and funding acquisition. J.V, S.G, and P.K provided the samples. K.R carried out the sample preparation, analysis, and data treatment of the bulk S elemental/isotopic determinations with aid from I.R. K.R created Fig. 3 with input from S.G, Ö.K, and P.C. Fig. 6 was created by Ö.K, C.B.S, and K.R. C.B.S, O.T., and Ö.K. contributed with the paleoclimate simulations, including development, data acquisition, and data treatment, as well as created Fig. 4-5, and Supplementary Fig. S10-S17. P.K provided μXRF S concentrations, assisted with literature study, and created Fig. 1, Fig. 2, and Supplementary Fig. S1, S6-S9. M.E.B contributed with TRIS analysis and contributed with pyrite S isotopic analysis of selected samples. S.G, C.B.S, P.K, Ö.K, O.T, M.E.B, I.R, J.V, P.C, and F.V contributed to reviewing and editing the manuscript. All authors approved the final draft of the manuscript.

ORCID numbers

K.R: https://orcid.org/0000-0002-9986-2166, S.G: https://orcid.org/0000-0002-6666-7153,

C.B.S: https://orcid.org/0000-0002-7677-9597, P.K: https://orcid.org/0000-0002-2605-6366,

Ö.K: https://orcid.org/0000-0003-0153-7291, O.T: https://orcid.org/0000-0002-7222-0948,

M.E.B: https://orcid.org/0000-0002-8877-0303, I.R: https://orcid.org/0000-0003-4505-4590,

J.V: https://orcid.org/0000-0001-6977-693X, P.C: https://orcid.org/0000-0002-4585-7687,

F.V: https://orcid.org/0000-0002-1884-3853

Abstract (Max 150 words)

The Chicxulub asteroid impact event at the Cretaceous-Paleogene (K-Pg) boundary ~66 Myr ago is widely considered responsible for the mass extinction event leading to the demise of the non-avian dinosaurs. Short-term cooling due to massive release of climate-active agents is hypothesized to have been crucial, with S-bearing gases originating from the target rock vaporization considered a main driving force. Yet, the magnitude of the S release remains poorly constrained. Here, the amount of impact-released S is estimated empirically relying on the concentration of S and its isotopic composition within the impact structure and a set of terrestrial K-Pg boundary ejecta sites for the first time. The value of 67 ± 39 Gt obtained is ~5-fold lower than recent numerical estimates but concurs with

numerical estimates from the 1990s. The lower mass of S-released implies global average temperatures above freezing point with key implications for species survival during the first years following the impact.

Introduction

Approximately 66 million years ago, a 10-15 km sized carbonaceous chondritic asteroid[1] collided with Earth, on the northern Yucatán Peninsula in Mexico, forming the ~200 km in diameter sized Chicxulub crater[2]. This event is linked to the mass extinction of approximately 75% of all species[3], including the non-avian dinosaurs, and led to the near-global loss of vegetation[4,5] at the Cretaceous-Paleogene (K-Pg) boundary[4,6–11]. The mass extinction is hypothesized to be due to a rapid change of climatic conditions, resulting from the massive release of dust and climate-active gases, including water vapor, CO_2, CH_4, and sulfur (S)-bearing gases, by shock-vaporization of the seawater and the carbonate- and evaporite-rich sedimentary cover of the Yucatán target rock[4,9,12,13]. In addition, a massive release of fine-grained ejecta reduced the amount of solar radiation reaching the Earth's surface, leading to a global impact winter state[13]. These fine-grained ejecta consist of silicate dust originating from pulverization of the deep Yucatán granitic basement ejected following the impact[4,13,14], sulfate aerosols formed from the vaporized evaporites and seawater[15], and soot from buried hydrocarbons[16,17] and impact-induced wildfires[16,18–20]. The impact winter triggered a blockage of photosynthesis and an extreme cold that affected Earth at the scale of years to decades[13,21–24]. Current models consider sulfate aerosols to be a crucial contribution to this global perturbation as they induce a net cooling effect due to their strong backscattering of solar radiation[25,26]. The impact winter was followed by long-term global warming for tens of thousands of years steered by CO_2 emitted from the dissociation of the carbonate target[4,12,21–24,27–30]. The short-term global cooling is often regarded as the most critical step in the global extinction event, although the relative role of impact-released sulfur remains poorly constrained.

The amount of sulfate aerosols injected within the atmospheric column and the residence time of the corresponding particles determines the severity of the sulfur-induced global cooling[30]. Residence time in the atmosphere depends on the altitude to which the impact vaporized S was injected into the atmosphere[12] and the type of injected S-species[26]. Impact-vaporized S-species injected into the oxidizing Paleogene atmosphere[31] reacted with O_2, OH, and/or H_2O to form sulfate aerosol (H_2SO_4), usually through the following series of simplified reactions $SO_2+OH^- \rightarrow HSO_3^- + O_2 \rightarrow SO_3 + H_2O \rightarrow H_2SO_4$ [26]. Photodissociation reactions also occurred due to absorption of visible light or UV-radiation following $H_2SO_4 + h\nu \rightarrow SO_3 + H_2O$ [26] and $SO_2 + h\nu \rightarrow SO + O$ [32]. With time, the sulfate aerosols formed settled down onto the Earth's surface via wet and/or dry deposition. Reduced S-species have a longer residence time than oxidized species and the injection height of the particles influenced the reaction rates as at higher altitudes the atmospheric conditions are less oxidizing, dryer, and less shielded from sun light (residence times of days to weeks for the troposphere and years to decades for the stratosphere)[26,30,33]. Numerical modeling of these physical and chemical processes in the climate system document the environmental changes triggered by the impact. The accuracy of paleoclimate model studies focusing on the influence of the impact-released S[13,23,24] is highly dependent on adequate estimations of the total amount of impact-volatilized S.

Current estimates of impact-released S are based on numerical methods in which the amount is constrained by simulating the impact using assumed parameters for the target rock and impactor based on field observations and small-scale laboratory experiments. Early estimates of total volatilized S by Sigurdsson *et al.* in 1992 (1300 to 4300 Gt S)[15], Brett in 1992 (200 Gt S)[34], Chen *et al.* 1994 (90 and 558 Gt S assuming an asteroidal and cometary impactor, respectively)[35], Pope *et al.* in 1994 (35 to 210 Gt S if a 10 km diameter impactor is assumed)[22], and Ivanov *et al.* in 1996 (40 to 110 Gt S in the case of a 10 km diameter impactor and 180 km wide crater)[36] are now considered unreliable as the composition, size, and equation of state for the impact site and projectile were updated in recent years.

Further, the very high amount of S injected into the atmosphere reported by Sigurdsson *et al.*[15] is now considered a major overestimation due to underestimation of the required shock pressures, which assumed complete degassing at ≥40 GPa. Recent studies based on thermodynamic and experimental data re-evaluated the pressure required to volatilize S from the target at ≥120 GPa[12,37]. Pierazzo *et al.* (1998)[21] addressed some of these shortcomings, providing an estimate of 40 to 560 Gt of vaporized S, by considering projectile size, velocity, and porosity, as well as target rock stratigraphy. By constraining the impact parameters to an asteroid that produced a transient cavity of ~100 km in diameter (size based on seismic data collected across the offshore portion of the Chicxulub transient cavity[38]), the estimated S injection into the atmosphere decreased to 90-250 Gt and further to 40-130 Gt when assuming 50% recombination of the S-bearing gases with CaO in the impact gas plume[21]. In 2003, Pierazzo *et al.* [23] simulated the consequent climate changes by applying these estimates of released S and ignoring other climate-active gases and particles to propose a global cooling at the Earth's surface by 2 to 8 °C with prolonged effects up to 13 years. In 2017, Artemieva *et al.* [12] applied more advanced hydrocode impact simulation models and recent constraints on the shock pressure, composition of the target rock, as well as asteroid impact angle. This latest simulated estimate of impact-volatilized S provided a significantly higher amount of released S of 325 ± 130 Gt. In the model applied by Artemieva *et al.* in 2017[12], only S ejected with sufficiently high velocity to reach the stratosphere was included. However, the porosity of the anhydrite in the target was assumed to be zero and the equation of state for anhydrite as well as recombination of S within the gas plume were not considered risking possible overestimation.

Recently, Tabor *et al.* 2020[24] and Senel *et al.* 2023[13] use the numerical estimation of 325 Gt S from Artemieva *et al.* 2017 [12] in two short-term paleoclimate studies in which the individual and combined effects of S, soot, and silicate or iron dust released following the Chicxulub impact event are modeled. Based on these simulations, the latter authors suggest that initially S was a main driver of the impact winter and that 325 Gt of released S resulted in an intense global average surface temperature

decrease from 21 to 7°C during the first 4 years after the impact[24] or from 19 to -5°C during the first 1.5 years after the impact[13]. However, within a few years post-impact, the influence of S rapidly diminished, as most of the sulfate aerosols settled back to Earth. With longer residence times in the atmosphere, dust and soot became the key factors governing the residual, albeit less severe, impact winter lasting up to ~20 years[13].

Previously used numerical estimations of impact-released S rely heavily on assumption of the proportion and distribution of evaporite within the target. Considering the size of the impact structure (~200 km) and the limited volume of impactite recovered during several drilling projects (Gulick *et al.* 2019[29]), a rigorous estimation of the proportion of evaporites present in the target rock lithology remains challenging. Currently, this estimation mainly relies on the stratigraphy (~27% anhydrite with the remaining intervals dominated by limestones and dolomites) of the ICDP (International Continental Scientific Drilling Program) Yax-1 (Yaxcopoil-1) drilling in 2001-2002 that penetrated the upper half of a ~3 km sequence of target Cretaceous sediments located beneath the outer annular trough of the Chicxulub impact structure[39–41]. The lower half of the Yucatàn sedimentary target is estimated to be more evaporite-rich (22-63% anhydrite) based on geophysical logs and well cuttings of the PEMEX (Petróleos Mexicanos) boreholes sampled in the 1950s and 1960s south/east of the crater[21,42] and stratigraphy of the 1994-1995 UNAM (Universidad Nacional Autónoma de México) drill cores within the ejecta blanket south of the Chicxulub impact structure[43,44]. However, these drill cores outside the crater rim may be too shallow to be representative of the deepest part of the sedimentary target rock. In contrast, the 2016 offshore drill core M0077A recovered from the northern part of the Chicxulub peak ring by IODP (International Ocean Discovery Program)-ICDP Expedition 364 is largely devoid of gypsum and anhydrite, and sulfur-bearing phases are limited to pyrite, chalcopyrite, and minor accessory minerals[29,45]. The potential heterogeneous distribution of evaporite within the Yucatán target

constitutes a considerable source of uncertainty during numerical estimation, which makes this approach to document S release unreliable.

Instead of focusing on the impact itself, empirical estimates rely on the aftermath of the impact-injected S into the atmosphere, mainly the wet and dry deposition of the globally distributed sulfate aerosols back to Earth's surface. If massive amounts of impact-sulfate aerosols were deposited globally, a positive S concentration anomaly should be observed at and after the K-Pg boundary clays in the sedimentary profiles of known K-Pg boundary sites. The amount of S in these K-Pg boundary sediment profiles related to the impact can be quantified using an isotope dilution approach if the S isotopic fingerprint ($\delta^{34}S$) of the target rock evaporite can be constrained with sufficient precision and if it is sufficiently distinct compared to the $\delta^{34}S$ of the natural bedrock of the K-Pg boundary site. These S anomaly profiles can then be used to empirically estimate the total amount of impact-released S using mass balance calculations. In contrast with numerical estimations, assumptions about the projectile size, velocity, and porosity, target rock stratigraphy, and interactions within the impact-related gas plume are not required. Instead, calculations rely on the S isotope ratio of the target rock and the preservation of the deposition record.

To date, only a few studies have investigated S isotopic compositions at the K-Pg boundary, where S isotope ratios in combination with S concentrations have been mostly used to investigate changes to the biogeochemical S-cycle post-impact. This includes shifting sulfate levels in seawater[46,47], duration of oxic/anoxic conditions based in part on observed large negative $\delta^{34}S$ shifts due to bloom of sulfate reducing microbes[48–54], and input from impact-related atmospheric sulfur[30,49,52,55,56]. Only one of these studies used the empirical S data from a K-Pg boundary deposition site to estimate the total amount of impact-released S. Junium *et al.*[30] provided the first empirical estimate of 400 Gt S using mass balance calculations with unspecified methodology relying on S data obtained from a shallow marine K-Pg boundary site, Brazos River (Texas, USA), about 900 km from the Chicxulub impact structure.

However, the Brazos River site is a well-established tsunami deposit (tsunamite)[57–60] situated close to the Chicxulub impact structure. The measured S values do not exclusively originate from impact-vaporized atmospheric S, but are likely also derived from S-rich ejecta washed-in with impact-tsunami deposits, leading to a mixed and biased estimate.

The current study provides a novel empirical estimate of the amount of impact-vaporized S using an isotope dilution approach based on a set of K-Pg boundary deposition sites to investigate the role of S in triggering the post-impact winter. The S fingerprint of the target rock is constrained by investigating the S elemental and isotopic composition in drill cores located within the Chicxulub impact structure and the proximal ejecta blanket. Sulfur concentrations and $\delta^{34}S$ values in K-Pg boundary sections, varying from terrestrial to deep marine, and proximal to distal relative to the impact-site, are investigated. The short-term climate effects, induced as a consequence of the estimated amount of impact-released S, are assessed using a three-dimensional atmospheric general circulation model (AGCM) with a simplified ocean model described by Senel *et al*. 2023[13].

Results and discussion

Sulfur concentration and isotopic composition in the target

The concentration of S and its isotopic composition are determined in selected lithological units in Cretaceous sediments of five onshore drill cores: PEMEX Y6 (Yucatán 6, located outside the peak ring area ~50 km southwest from the center of the impact structure)[61,62], UNAM-5 (located outside the crater in the proximal ejecta blanket ~105 km south from the center of the impact structure), UNAM-6 (located outside the crater in the proximal ejecta blanket ~151 km southeast of the center of the impact structure), UNAM-7 (located outside the crater in the proximal ejecta blanket ~126 km southeast of the center of the impact structure)[43], and ICDP Yax-1 (Yaxcopoil-1, located in the outer part of an annular trough

~60 km south of the center of the impact structure)[39], as well as the offshore drill core IODP-ICDP Expedition 364 M0077A (located on the topographic peak ring ~46 km northwest of the center of the impact structure)[45]. The locations of these drill cores are shown in Fig. 1A. Measured bulk $\delta^{34}S$ values and S concentrations throughout the different lithological units of the M0077A drill core are shown in Fig. 1B (Fig. S1 in the supplementary information (SI) focuses only on the K-Pg boundary claystone interval). In addition, the range in $\delta^{34}S$ values and S concentrations for the five onshore drill cores are presented in Fig. 1.

Anhydrite within unshocked Cretaceous sediments at the impact site (Yax-1) and in the proximal ejecta blanket (UNAM-5, 6 and 7) shows variation between 6 and 23 wt% S and $\delta^{34}S$ values showing a narrow range between 18.0 and 19.5‰. Suevite and impact melt intervals within drill core Y6 show 0.5 to 2 wt% S and $\delta^{34}S$=17.1-17.9‰ (Fig. 1B; Fig. S2 and Table S1 in the SI). All onshore drill cores display $\delta^{34}S$ values (17.1-19.5‰) that agree with the previously determined average $\delta^{34}S$ value of 18.3‰ for the Yax-1 and Y6 drill cores (ranging between 18.0 to 19.8‰)[63] and the seawater sulfate $\delta^{34}S$ values ranging between 17 to 19‰ at the end of the Cretaceous [46,64]. The high S concentrations observed for Yax-1 and UNAM-6 (23 and 20 wt% S, respectively) indicate pure anhydrite and gypsum (19 to 24 wt% S), while the S content in the other drill core samples (0.5-10 wt% S) represents a mixed composition with a large admixture of evaporite as even the lower S concentrations found in the suevite and impact melt rock sections of the Y6 core have similar $\delta^{34}S$ values (Fig. S2 in the SI). The total reduced inorganic S (TRIS) content was measured for the suevite and impact melt sections in the Y6 drill core (24 and 52 μg g^{-1}, respectively, Table S3 in the SI). This corresponds to TRIS fractions of 0.1 and 1% of the bulk S concentration, respectively, indicating that these sections mostly contain oxidized S-species such as anhydrite and gypsum.

Detailed bulk S concentration and $\delta^{34}S$ profiles are provided for M0077A as evaporites had previously been observed to be largely absent from this drill core[29]. These profiles span different

lithological units[65], including the post-impact Paleogene sediments, suevite (impact-melt bearing polymict breccia), upper impact melt rock (UIM), lower impact melt rock-bearing rock (LIMB), and intermediate intervals below the UIM, including granitoid, dolerite, and dacite basement material to constrain the various contributing sources of S and determine the effects of post-impact processes overprinting the primary S isotopic signatures (Fig. 1B; Table S1 in the SI, detailed discussion found in SI). The TRIS fraction in selected samples throughout the M0077A drill core (140-7,000 μg g^{-1}) corresponds to 22-86% of the bulk S concentration. The lowest TRIS fractions (22-33%) are found in the graded suevite, a metamorphic clast, and lower LIMB units (Fig. S5 and Table S3 in the SI, detailed discussion found in SI), consistent with higher bulk $\delta^{34}S$ values (0.7-8.5‰), indicating that traces of evaporite may be preserved within the M0077A drill core. Among them, the graded suevite section has the highest bulk $\delta^{34}S$ value and the largest shift (14.0‰) between the bulk $\delta^{34}S$ and the sulfide-specific $\delta^{34}S$ (-5.5‰, Table S3 in the SI). As the bulk S concentrations (500-1500 μg g^{-1}) and $\delta^{34}S$ values are lower in these lithological units compared to the five onshore drill cores (Yax-1, Y6, and UNAM-5-7), the measured signals of the target bedrock are likely influenced by later post-impact processes. For instance, in contrast to the graded suevite section, the bedded suevite section right above has significantly lower bulk $\delta^{34}S$ (-7.4 to -5.3 ‰), a higher TRIS fraction (85%), and a small shift (1.9‰) between the bulk $\delta^{34}S$ and the sulfide-specific $\delta^{34}S$ (-9.2‰) (Table S1 and S3 in the SI). Similarly low sulfide $\delta^{34}S$ values have previously been observed in the post-impact sediment sections in the M0077A drill core by Schaefer *et al.* 2020[53] (Fig. 1B), and suggested by Kring *et al.* 2020[66], 2021[54] to result from late-stage microbial reduction of S in an impact-generated hydrothermal systems. The bulk $\delta^{34}S$ value of the target rock is therefore determined based on the $\delta^{34}S$ values observed for the evaporite-containing lithological units in five different drill cores located at the Chicxulub impact structure (Yax-1, Y6, and UNAM-5-7), which leads to a target rock $\delta^{34}S$ value of 18.5 ± 1.4‰ (2SD).

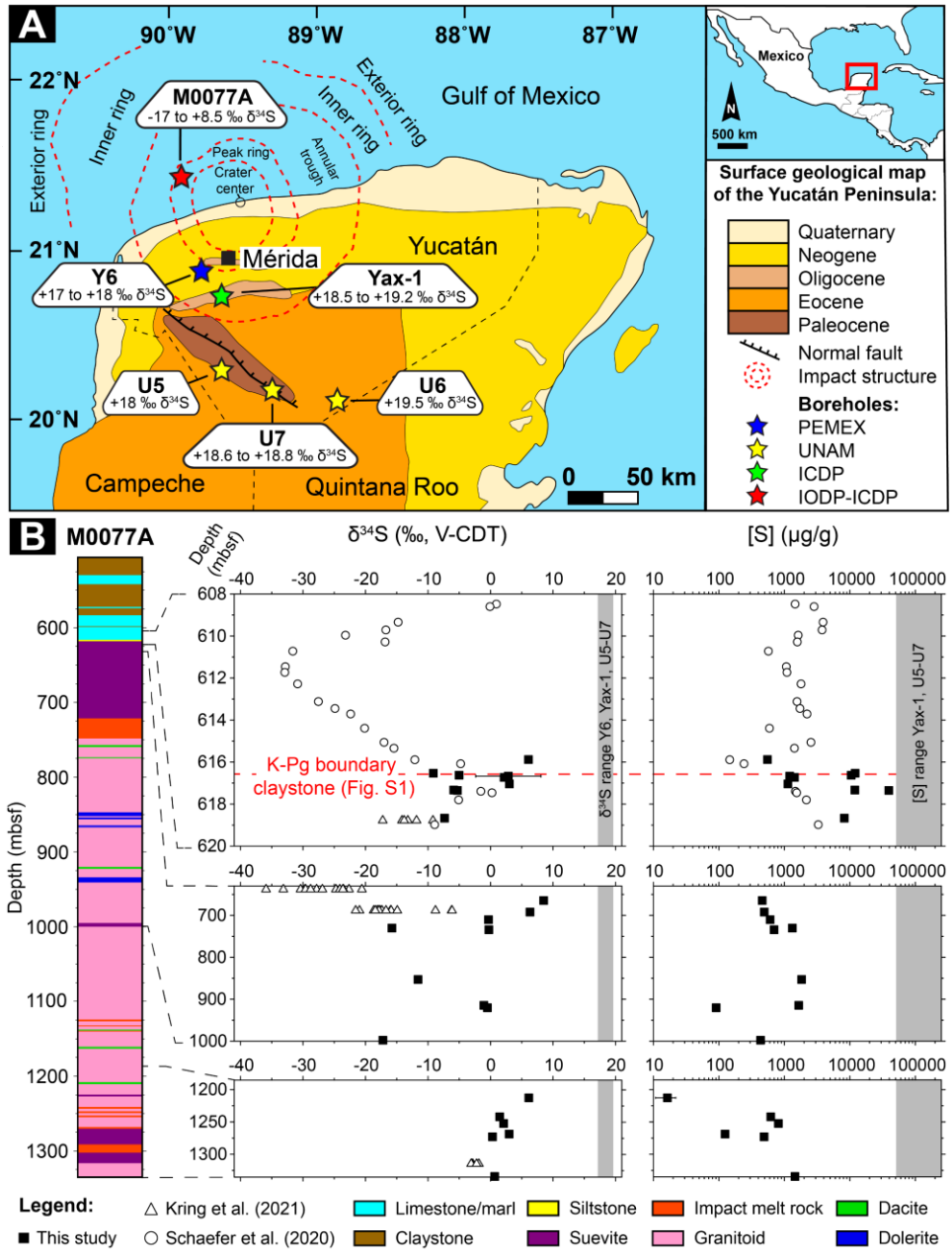

Fig. 1. (A) Simplified geological surface map of the Yucatán Peninsula in Mexico (modified from Kaskes *et al.* 2022[65], 2024[67]) with the subsurface features of the Chicxulub impact structure marked. On the map, drill core locations are highlighted using stars in different colors. Next to each star, the corresponding measured bulk $\delta^{34}S$ range is presented. **(B)** Simplified lithological column for the IODP-ICDP Expedition 364 M0077A drill core with corresponding measured bulk $\delta^{34}S$ values and S

concentrations (on a logarithmic scale). The equivalent of the K-Pg boundary claystone, characterized by an Ir anomaly based on Goderis *et al.* 2021[68], is shown here by a red dashed line. A more high-resolution visualization of the interval surrounding the K-Pg boundary claystone is displayed in Fig. S1. For comparison, previously published pyrite-related S concentrations and $\delta^{34}S$ values from two studies of the M0077A drill core are included, Schaefer *et al.* 2020[53] (circular markers) and Kring *et al.* 2021[54] (triangular markers). The range of measured bulk $\delta^{34}S$ values and S concentrations for the five other drill core samples (Y6, Yax-1, UNAM 5-7 and Yax-1, UNAM 5-7, respectively) obtained in the present study are highlighted by a gray area in the graphs.

Sulfur concentration and isotopic profiles for K-Pg boundary sites

The locations of all the K-Pg boundary deposition sites included in this study are presented in Fig. 2A, while Fig. 2B-I shows the bulk S concentration and $\delta^{34}S$ profiles. Full profiles across the K-Pg boundary were measured for four of these K-Pg boundary sites (Fig. 2B-E). The localities selected for full profiles include the distal mid-shelf marine site at Stevns Klint (Denmark, neritic with estimated water depths at K-Pg boundary times of 100-150 m[69]), a distal deep marine site at Caravaca (Spain, bathyal with estimated water depths of 500-1,000 m[69]), an intermediate terrestrial site at Tanis (Hell Creek formation, North Dakota, USA[70]), and another proximal mid-shelf marine K-Pg boundary section, sampled in the same region as the one previously used[30], Brazos River (Texas, USA, neritic with estimated water depths of 75-100 m[10]) located approximately 6,400; 5,500; 3,000; and 900 km from the Chicxulub impact structure, respectively. Siderophile elements, such as Cr, Co, Ni, Re, and Ir were also measured in these profiles to correlate S input with a meteoritic contribution (Fig. S6-9 and Table S4, detailed discussion in the SI).

For comparison, the bulk S concentration and the $\delta^{34}S$ value were additionally investigated for other K-Pg boundary sites but using only a single sample located precisely within the K-Pg boundary

claystone (Table S2 in the SI). These sites included a proximal bathyal marine site at Beloc (Haiti, 150 μg g^{-1} and 17 ‰), several intermediate terrestrial sites at Long Canyon (Raton Basin, Colorado, USA, 1,500 μg g^{-1} and 4.0 ‰), Dogie Creek (Powder River Basin, Wyoming, USA, 3,300 μg g^{-1} and -0.89 ‰), Brownie Butte (Hell Creek area, Montana, USA, 4,200 μg g^{-1} and -3.2 ‰), and Seven Blackfoot Creek (Hell Creek area, Montana, USA, 500 μg g^{-1} and -2.0 ‰), as well as several distal bathyal and outer-neritic/upper-bathyal marine sites at Frontale (Italy, 90 μg g^{-1} and 16 ‰), Fonte d'Olio (Italy, 170 μg g^{-1} and 16 ‰), Siliana (Tunisia, 3,600 μg g^{-1} and 13 ‰), and Elles (Tunisia, 63,000 μg g^{-1} and 18 ‰) located approximately 500; 2,250; 3,000; 3,100; 3,100; 6,300; 6,300; 6,700; and 6,700 km from the Chicxulub impact structure[71], respectively (Fig. 2A).

A positive peak in S concentration coinciding with positive $\delta^{34}S$ values, as expected for atmospherically deposited target anhydrite, is observed in the boundary claystone and coal interval of the terrestrial Tanis K-Pg site (600-8,000 μg g^{-1} and -6 ‰ to 5 ‰, respectively) (Fig. 2E; Table S2 in the SI). This positive S anomaly coincides with positive siderophile element anomalies (Ir, Re, Co, Cr, Ni,), chondritic inter-element ratios (e.g., Ni/Cr), and previously published significantly finer and unimodal median grain-sizes[13] (Fig. S5 and Table S4 in the SI, detailed discussion found in the SI), which combined indicate airfall of finely mixed impactor and target rock material directly on top of the Tanis silty event deposit[70]. The positive S offset is similar to the previously documented S-profiles for other terrestrial K-Pg sites. These sites include Dogie Creek (~500 μg g^{-1} to ~26,000 μg g^{-1} and -5 ‰ to 1 ‰, Fig. 2F) and Brownie Butte (~2,000 μg g^{-1} to ~22,000 μg g^{-1} and -3 ‰ to 6 ‰, Fig. 2G) in Maruoka *et al.* 2002[52] and Knudsen's Coulee (Canada at ~4300 km, ~300 μg g^{-1} to ~9,000 μg g^{-1} and 2 ‰ to 17 ‰, Fig. 2H) and Knudsen's Farm (Canada at ~4300 km, ~2.5 km from Knudsen's Coulee site, ~500 μg g^{-1} to ~8,000 μg g^{-1} and 2 ‰ to 9 ‰, Fig. 2I) in Cousineau 2013[56]. The two additional terrestrial K-Pg deposition sites investigated in this study, Long Canyon and Seven Blackfoot Creek, show similar bulk $\delta^{34}S$ values in the K-Pg boundary clay (4 ‰ and -2 ‰, respectively), but only Long

Canyon display bulk S concentrations (~1,500 μg g^{-1}) similar to those observed at the other terrestrial sites. The S concentration at Seven Blackfoot Creek (~500 μg g^{-1}) (Table S2 in the SI) is likely too low to reflect vaporized anhydrite target deposition. The $\delta^{34}S$ values for the Long Canyon site are similar to previously published[55] $\delta^{34}S$ values for another Raton Basin terrestrial site, Sugarite (Raton Basin, New Mexico, USA, 2,100 km from the Chicxulub impact structure), where an incomplete profile indicates that the $\delta^{34}S$ values increased (4.6 to 8.0 ‰) in the K-Pg boundary claystone in a similar manner comparable to what is observed for the terrestrial sites discussed above.

In contrast to the terrestrial Tanis site, a positive peak in S and siderophile element concentrations coincides with a negative $\delta^{34}S$ peak for the marine Stevns Klint (400-11,000 μg g^{-1} and 18 ‰ to -39 ‰, respectively) and Caravaca (300-800 μg g^{-1} and 19 ‰ to -32 ‰, respectively) K-Pg site profiles (Fig. 2B-C; Fig. S7-8; Table S2 and S4 in the SI). This is likely a result of S fractionation during microbial reduction of sulfate followed by pyrite sedimentation[48]. The Caravaca site additionally shows a positive $\delta^{34}S$ peak in the limestone/marl section below the K-Pg claystone, which does not correspond to a positive peak in the S concentration, possibly indicating impact-related sulfate deposition, although it could also result from incorporation of seawater sulfate (e.g. carbonate-associated sulfate in the limestone/marl sections[72]) at this marine site. The S profiles obtained for the previously used[30] marine Brazos River site display positive peaks in S concentration coinciding with a positive $\delta^{34}S$ anomaly (6,000-30,000 μg g^{-1} and -40 ‰ to -33 ‰), similarly as observed in previously published[49] S profiles for the distal marine Kawaruppu K-Pg boundary section (Tokachi District, Hokkaido, Japan, 11,000 km from the Chicxulub impact structure, 900-5,400 μg g^{-1} and -35 ‰ to 0 ‰). In contrast to the other sites the S-profiles for these two marine sites are jagged (Fig. 2D and Fig. 1 in Kajiwara and Kaiho 1992[49]), indicating heterogenous S input in these K-Pg sediments. For the Brazos River site, the siderophile element profiles are also jagged (Fig. S9 in the SI) and large variations are observed in the bulk S concentration and $\delta^{34}S$ values for multiple sub-samples in the sandstone section

(Fig. 2D), likely resulting from the mixing of S deposition from the atmosphere and, due to the proximity of Brazos River to the impact site, the wash-in of anhydrite-rich material derived from the crater region[73] (detailed discussion found in the SI).

The low $\delta^{34}S$ values observed across the entire K-Pg boundary interval at the Stevns Klint (Fig. 2B), Brazos River (Fig. 2D), and Kawaruppu (Fig. 1 in Kajiwara and Kaiho 1992[49]) sites and in selected samples at the K-Pg boundary at the Caravaca site (Fig. 2C) may result from large S fractionation during microbial reduction, which has been suggested for these sites in previous studies[30,48,50,51]. The K-Pg sections in the mid-shelf marine sites, Stevns Klint and Brazos River, are additionally marked by sedimentary enrichment of Mo and blooms of stress-tolerant endobenthic foraminifera, indicating increased input of organic matter and hypoxic seafloor conditions at these sites following the K-Pg impact event[69]. These low oxygen conditions additionally support the hypothesis of larger S isotope fractionation during microbial reduction of sulfate to form pyrite at these sites post-impact, as overall sulfur isotope fractionation increases with increasing sulfate concentration above a critical level (reservoir effect[74]) and is physiologically further supported by an elevated input of poorly reactive organic substrates[75,76]. At the deep marine Caravaca site, hypoxic conditions were brief[69], which also agrees with very low $\delta^{34}S$ values measured only < 0.25 cm above the K-Pg boundary. Therefore, post-impact microbial S reduction leading to large fractionation of the $\delta^{34}S$ values cannot be ruled out for these sites, meaning that the S concentration and $\delta^{34}S$ signals determined at these sites likely do not exclusively reflect deposition of atmospheric S.

Terrestrial environments, more specifically paludal to lacustrine settings, are considered to be more suitable for investigation of impact-derived S as the background S concentrations are generally low and the deposited S is considered less perturbed in relation to marine environments[52,77]. The impact-deposited sulfate at terrestrial sites may also undergo microbial reduction that could result in underestimation of the total amount of impact-released S, however, these sites typically have lower

sulfate concentrations, so S isotope fractionations are typically considered to be small[74]. Depending on the local environment, a substantial addition of sulfate to terrestrial environments has been observed to result in significantly higher S isotope fractionations. For example, large S fractionation up to 50.5‰ has recently been observed in samples from a Cretaceous (~85 Myr ago) terrestrial inland rift basin located in northeast China[78]. Sulfur isotope fractionation between sulfate and sulfide, and gypsum and marcasite between 44 and 78‰ was observed at Haughton Crater in the Canadian High Arctic, and a sulfur isotope spread of 77‰ was reported for the Miocene German Nördlinger Ries crater[77]. Thus, the large $\delta^{34}S$ shift is attributed to singular or repeated seawater incursion events, during which the influx of sulfate-rich marine water into a sulfate-poor basin likely led to increased S isotope fractionation during microbial reduction. Negative correlation between S concentrations and $\delta^{34}S$ values are only observed briefly in the S profiles for one terrestrial site included in this study (in the K-Pg boundary claystone of Dogie Creek, Fig. 2F), attributed to microbial reduction during anoxic conditions in the Dogie Creek wetlands around the K-Pg boundary by Maruoka *et al.* 2002[52]. However, this negative $\delta^{34}S$ shift is small (1.7 ‰, -2.9 to -4.6 ‰) and the rest of the Dogie Creek S profiles exclusively show positive correlations. In contrast to the marine site sediment profiles included in this study and the aforementioned previously published terrestrial sediment profiles[77,78], microbial reduction fractionation effects are assumed to be small for all terrestrial sediment profiles discussed in this study (Tanis, Dogie Creek, Brownie Butte, Knudsen's Coulee, and Knudsen's Farm; Fig. 2E-I). All these terrestrial profiles display a comparable positive $\delta^{34}S$ excursion and none of the 5 sites show any type of highly negative $\delta^{34}S$ values, despite deposition in strongly different local environments.

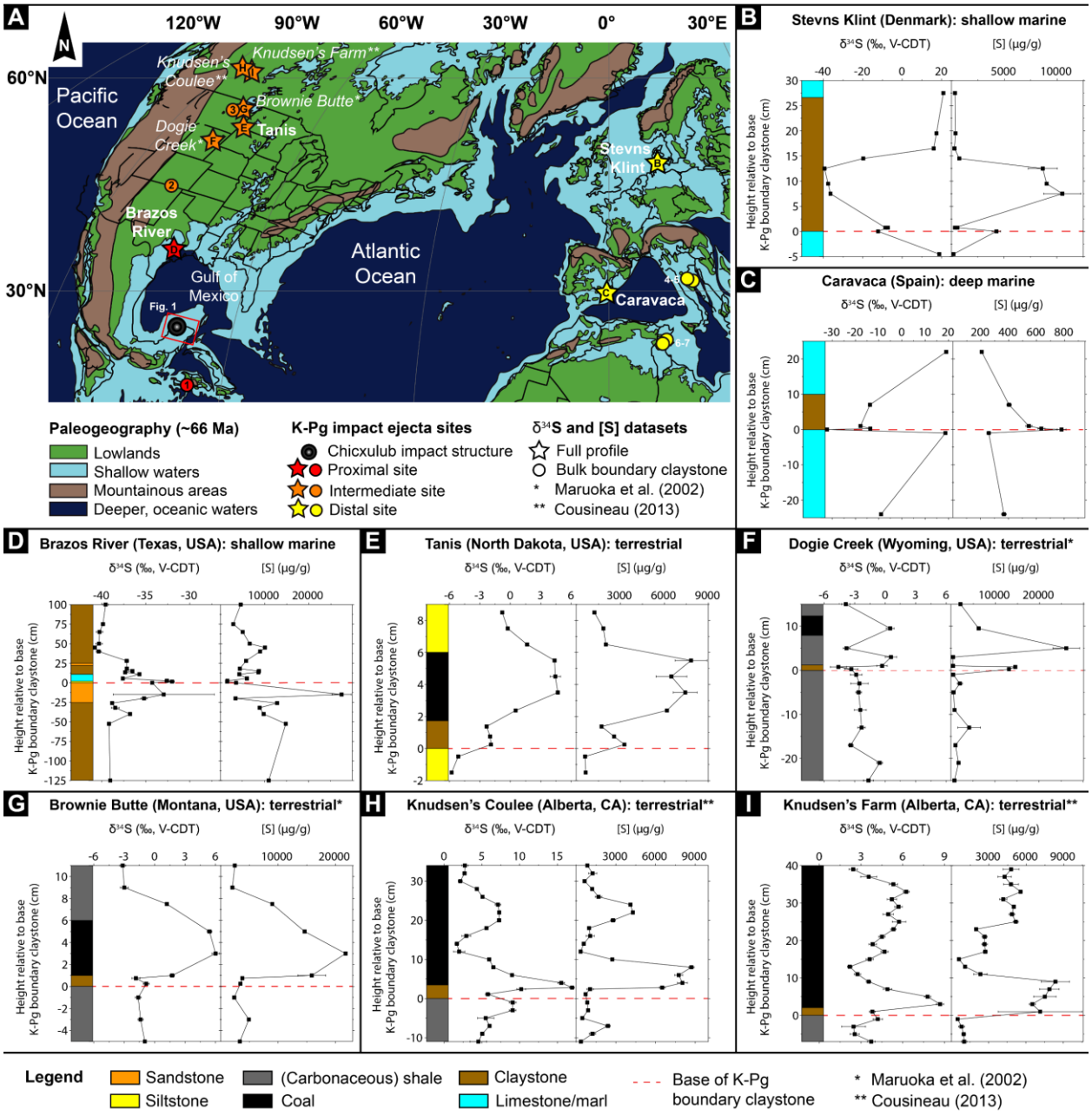

Fig. 2. (A) Simplified paleogeographic map reconstructed for the Late Cretaceous with K-Pg impact ejecta sites included in this study highlighted. Different colors represent proximity of the site to the Chicxulub impact structure, from 500 to 6,700 km (modified from Goderis *et al.* 2021[68]). The stars represent K-Pg sites for which both bulk S concentration and $\delta^{34}S$ profiles around the K-Pg boundary were determined, while circles represent K-Pg sites for which the bulk S concentration and $\delta^{34}S$ value

were determined in the K-Pg boundary claystone only. The numbers correspond to K-Pg sites: (1) Beloc; (2) Long Canyon; (3) Seven Blackfoot Creek; (4) Frontale; (5) Fonte D'Olio; (6) Siliana; (7) Elles. **(B-I)** Simplified lithological profiles with corresponding measured bulk $\delta^{34}S$ and S concentration profiles for 8 K-Pg boundary sites, ranging from deep marine to terrestrial environments and from proximal to distal sites. These include: (B) Stevns Klint; (C) Caravaca; (D) Brazos River; (E) Tanis; (F) Dogie Creek (from Maruoka *et al.* 2002[52]); (G) Brownie Butte (from Maruoka *et al.* 2002[52]); (H) Knudsen Coulee (from Cousineau 2013[56]); and (I) Knudsen Farm (from Cousineau 2013[56]). Error bars represent the external uncertainty or 2SD and are often smaller than the markers. The dashed red line represents the base of the K-Pg boundary claystone or equivalent thereof.

Estimated total amount of impact-released sulfur

The empirical estimate of the total amount of impact-vaporized S is calculated by combining large-scale isotope dilution and mass balance calculations, using the $\delta^{34}S$ fingerprint of the target rock evaporite (18.5 ± 1.4‰ based on Yax-1, Y6, and UNAM-5-7), as well as S concentration and $\delta^{34}S$ profiles in well-preserved K-Pg boundary deposition sites (Fig. S3 in the SI). The possible post-impact processes observed in the Stevns Klint, Caravaca, Brazos River, and Kawaruppu S profiles (Fig. 2B-D and Fig. 1 in Kajiwara and Kaiho 1992[49]) hamper the use of marine K-Pg profiles for accurate estimations of the amount of impact-released S into the atmosphere. Indeed, these processes can lead to under- or overestimations, as illustrated by the likely overestimated value for the Brazos River site provided by Junium *et al.* 2022[30] and in this study (Fig. 3, detailed discussion in the SI). Terrestrial K-Pg boundary sites are more likely to preserve the airborne S component and are therefore more reliable for calculating the impact-released S.

The empirical estimate of the amount of impact-released S is determined based on five terrestrial K-Pg boundary depositional profiles, and is estimated to be 67 ± 39 Gigatonnes (Gt) (2SD).

These sites include Tanis (58 ± 9 Gt S, 2SD), for which bulk S concentrations and $\delta^{34}S$ values were obtained in this study, Dogie Creek[52] (48 ± 14 Gt S, 2SD), Brownie Butte[52] (104 ± 13 Gt S, 2SD), Knudsen's Coulee[56] (71 ± 11 Gt S, 2SD), and Knudsen's Farm[56] (57 ± 5 Gt S, 2SD), for which the estimates were calculated using published bulk S concentrations and $\delta^{34}S$ values. While these five terrestrial sites all occur within 3,000-4,300 km of the Chicxulub impact structure and are all located on the North American continent, thus reflecting a limited spread across the globe, we presume that the highly reproducible S volumes obtained for these sites support their representativeness for the global non-ballistic atmospheric fallout of S-rich ejecta components. The highly reproducible impact-released S amounts (67 ± 39 Gt, 2SD) of these 5 sites also suggest that the airborne S component was preserved with minimal influence of post-impact processes, such as significant S isotopic fractionation during microbial reduction of the sulfate or wash-out of the sulfate.

The new empirical estimate range of 28-106 Gt S, with an average of 67 ± 39 Gt S, is in excellent agreement with numerical estimate ranges published in the 1990's, particularly the data reported in Chen *et al.* 1994[35] (90 Gt S), Pope *et al.* 1994[22] (35-210 Gt S), Ivanov *et al.* 1996[36] (40-110 Gt S), and Pierazzo *et al.* 1998[21] (40-130 Gt S, assuming 50% recombination of vaporized S) (Fig. 3). However, the new value is a 5-fold lower relative to more recent numerical estimates of 325 ± 130 Gt S[12] (Fig. 3).

One possible explanation for the lower estimates is the occurrence of post-depositional effects at the terrestrial K-Pg boundary sites, which may affect the anhydrite signal and result in an underestimation of the true amount of deposited S in mass balance calculations. However, in this case, a large spread in the estimates between the different K-Pg boundary sites examined is expected. In contrast, a close match is observed between the estimated amount of impact-released S between the five localities, rendering the possibility of a local overprint unlikely. A more likely explanation is that other approaches overestimated the atmospheric impact-derived load of S by i) underestimating the

heterogeneity of the evaporites within the target rock, ii) assuming zero porosity of the anhydrite in the target, iii) using no equations of state for the anhydrite in the simulations, iv) not taking into account the occurrence of impact fragmentation followed by low-velocity ejection of sulfate blocks, and/or v) not considering recombination of S-bearing species within the gas plume. Firstly, the lack of anhydrite and gypsum in the most recent M0077A drill core, compared to previous drill cores of the impact crater (detailed discussion in the SI), likely illustrates a more heterogeneous distribution of evaporites within the impact structure than previously considered. To date, numerical simulations have mostly assumed a homogenous block of 22-63% anhydrite over the entire ~200 km impact structure, which is not consistent with results from the M0077A drill core compared to e.g. Yax-1 and Y6. Therefore, it reflects a considerable source of error that must be taken into account in future simulations. Another important source of error is the occurrence of recombination effects, as observed for carbonates[67]. Based on clumped-isotope data and petrographic observations for carbonate-bearing samples in several drill cores from the Chicxulub impact structure, Kaskes *et al.* 2024[67] suggests that prior work likely overestimates the volume of impact-released CO_2 due to insufficient consideration of recombination effects. Consequently, the volume of impact-released S gases into the atmosphere is likely also overestimated by not considering possible recombination of the S-bearing gases with CaO within the gas plume. The agreement between the new empirical estimate of impact-released S obtained in the current study (67 ± 39 Gt S) and the numerical estimate range of 40 to 130 Gt S by Pierazzo *et al.* 1998[21], where 50 % recombination of the S-bearing gases in the impact gas plume is assumed, supports such recombination effects (Fig. 3). Overall, several lines of evidence indicate that the Chicxulub cratering event released approximately 5-fold less S into the atmosphere than the most current numerical estimate, hinting towards a different climatic and biotic response in the earliest Paleogene than previously assumed.

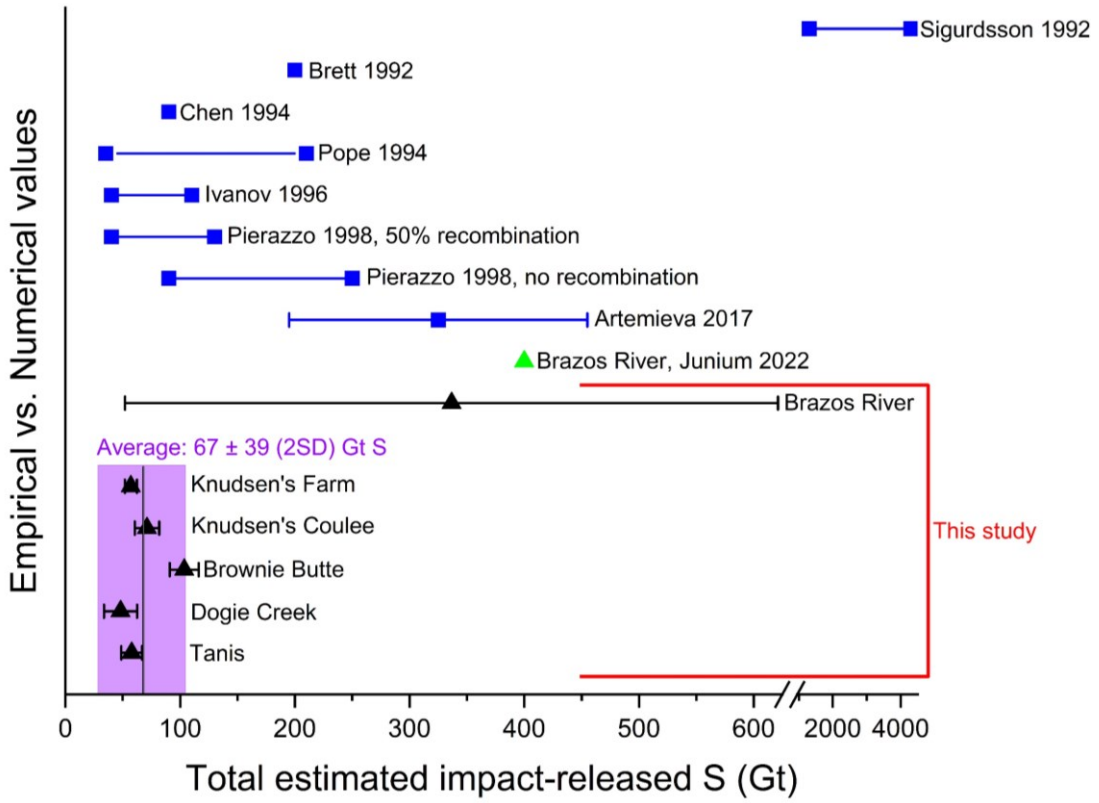

Fig. 3. Comparison between empirical (triangle markers) and numerical (square markers) estimations of the amount of S (in Gigatonnes; Gt) vaporized following the Chicxulub impact event. The black markers represent empirical S estimations based on $\delta^{34}S$ and S-concentration values from various K-Pg boundary sites, with the error bars representing 2SD uncertainty of the values. The purple shadowed region shows the average of all these 5 K-Pg boundary sites (67 ± 39 Gt), excluding the Brazos River site due to the corresponding large uncertainties. Previously published empirical (Junium *et al.* 2022[30], green marker) and numerical estimates (Sigurdsson *et al.* 1992[15], Brett 1992[34], Chen *et al.* 1994[35], Pope *et al.* 1994[22], Ivanov *et al.* 1996[36], Pierazzo *et al.* 1998[21], Artemieva *et al.* 2017[12], blue markers) are also included.

Impact of released S on the global climate

Paleoclimate simulations focusing on the influence of atmospheric S were performed using the empirical estimate for ~70 Gt impact-released S (Fig. 4a and 5). This value results in global effects with a significant initial drop in average global surface temperatures, from 19 °C[79–81] to 2 °C, reaching the minimum value ~8 months post-impact (Fig. 4a and 5). After this initial temperature drop, global-average surface temperatures start to recover as the concentration of sulfate aerosols in the atmosphere decreases due to dry and wet deposition (Fig. 4b). Seasonal temperature variability starts to return ~2 years post-impact (Fig. 4a). The climate gradually recovers, with global-average surface temperatures reaching pre-impact values approximately 5.5 years post-impact (Fig. 4a and 4b) and showing negligible effects 10 years post-impact (Fig. 4a and 5).

The lowest (~30 Gt) and highest (~110 Gt) values in this new range were also evaluated with paleoclimate simulations (Fig. 4a; Fig. S10 and S11 in the SI). Similar global effects are observed as for the average of ~70 Gt S, but with the temperature drop and duration of the impact winter being less severe for the ~30 Gt S and more severe for ~110 Gt S (Fig. 6; Fig. S10 and S11 in the SI). No value within this new empirical estimated range of impact-released S gives rise to global-average temperatures below freezing point (Fig. 6).

For comparison purposes, simulations were performed for the most recent and significantly larger numerical estimate of 325 ± 130 Gt by Artemieva *et al.* 2017[12], using both the minimum (~200 Gt S) and average (325 Gt S) values. Large differences in both the magnitude and duration of the simulated temperature drop are observed when comparing the respective simulated paleoclimate results with that based on the ~70 Gt S empirical estimate (Fig. 4-6; Fig. S12-14 in the SI). The corresponding differences in temperature decrease with time, with the largest difference in temperature between these two total impact-released S estimations observed 1 year after the impact, while 10 years post-impact no considerable difference in temperature is observed any longer (compare Fig. 5 with Fig. S12-13 in the SI).

The injection of ~70 Gt instead of 325 Gt of S, as advocated in this study, decreases the importance of the release of S as the killing mechanism as it leads to a less drastic short-term climate perturbation as compared to the previous paleoclimate scenarios simulated by Tabor *et al.* 2020[24] and Senel *et al.* 2023[13] using the 325 Gt S from Artemieva *et al.* 2017[12]. The milder impact winter scenario generated by the release of 67 ± 39 Gt (2SD) of S could have important repercussions on the extinction and survival patterns across the K-Pg boundary. An approximate 4 °C higher global-average surface temperature over a 0.5-1.5 years period post-impact (Fig. 6), larger terrestrial regional differences up to 20 °C (Fig. S14 in the SI), and a duration of the initial impact winter that is about 8-10 months shorter is significant (Fig. 4a), particularly as the new estimate does not result in global average temperatures below freezing point (Fig. 6). Combined, these conditions allow for a crucial 'survival window' for many species[5,82–95] compared to the most recent numerical estimate by Artemieva *et al.* 2017[12], aiding in the persistence of at least 25% of species on Earth[3]. Additionally, regional temperature differences could aid in understanding variations in survivorship within different habitats, providing refugia in certain geographic locations that could have been less affected by the impact winter induced cooling. Using these simulations, oceans were least impacted by cooling, because of the high thermal inertia, followed by tropical continental regions, and lastly by temperate and polar regions (Fig. 5). However, this simulated scenario does not take into account the additional influence of other climate-active particles, such as soot and dust, as well as their interactions with sulfate aerosol in the atmosphere.

Senel *et al.* 2023[13] investigated the combined effects of S (325 Gt S from Artemieva *et al.* 2017[12]), silicate dust, and soot using the same GCM model as employed in this study. They observed that the S ejected into the atmosphere is the main driver of the major cooling occurring during the first years of the impact winter, consistent with the finding of Brugger *et al.* 2017[28]. The other impact-released climate-active agents, such as soot and dust affect the temperature to a smaller degree, however, they act at longer time scales. Differently, Tabor *et al.* 2020[24] suggest that the prime factor

contributing to the extreme cold is soot instead, with the S agent playing a secondary role. Following the present work, using the lower S estimate decreases the extent and duration of the initial cooling spike even in the combined scenario. While our simulations show an earlier onset of initial cold than Brugger *et al.* 2017[28], both studies indicate an earlier spike relative to Tabor *et al.* 2020[24]. Additionally, our S-only estimate for the recovery timescale (~15 years) agrees with the finding of Tabor *et al.* 2020[24], which also projects normalization of the temperatures ~15 years after impact. Yet, the simulations by Brugger *et al.* 2017[28] show a more extended period (~30 years) needed for recovery. These variations in models could be attributed to the thermal inertia settings of land areas and oceans, or the interplay of other factors considered across different modeling studies, encompassing emission, aerosol, land, and ocean physics.

Importantly, while the cooling was a contributor to the mass extinction, Senel *et al.* 2023[13] demonstrated that the main killing mechanism of the impact winter appeared to be the drastic decrease in photosynthetic active radiation (PAR, solar radiation from 400-700 nm is being used by organisms in the process of photosynthesis) reaching the Earth's surface, leading to photosynthetic shut-down. Both S and soot lead to a significantly faster PAR recovery (~1 year post-impact) compared to the micrometer-sized silicate dust (~4 years post-impact), implying that instead the dust may be the principal killer in the K-Pg mass extinction, with S and soot as important "accomplices"[13]. The lower estimates of the amount of impact-released S obtained in this study induce an even faster PAR recovery related to S, which further decreases the role of S in the killing mechanism of the K-Pg mass extinction.

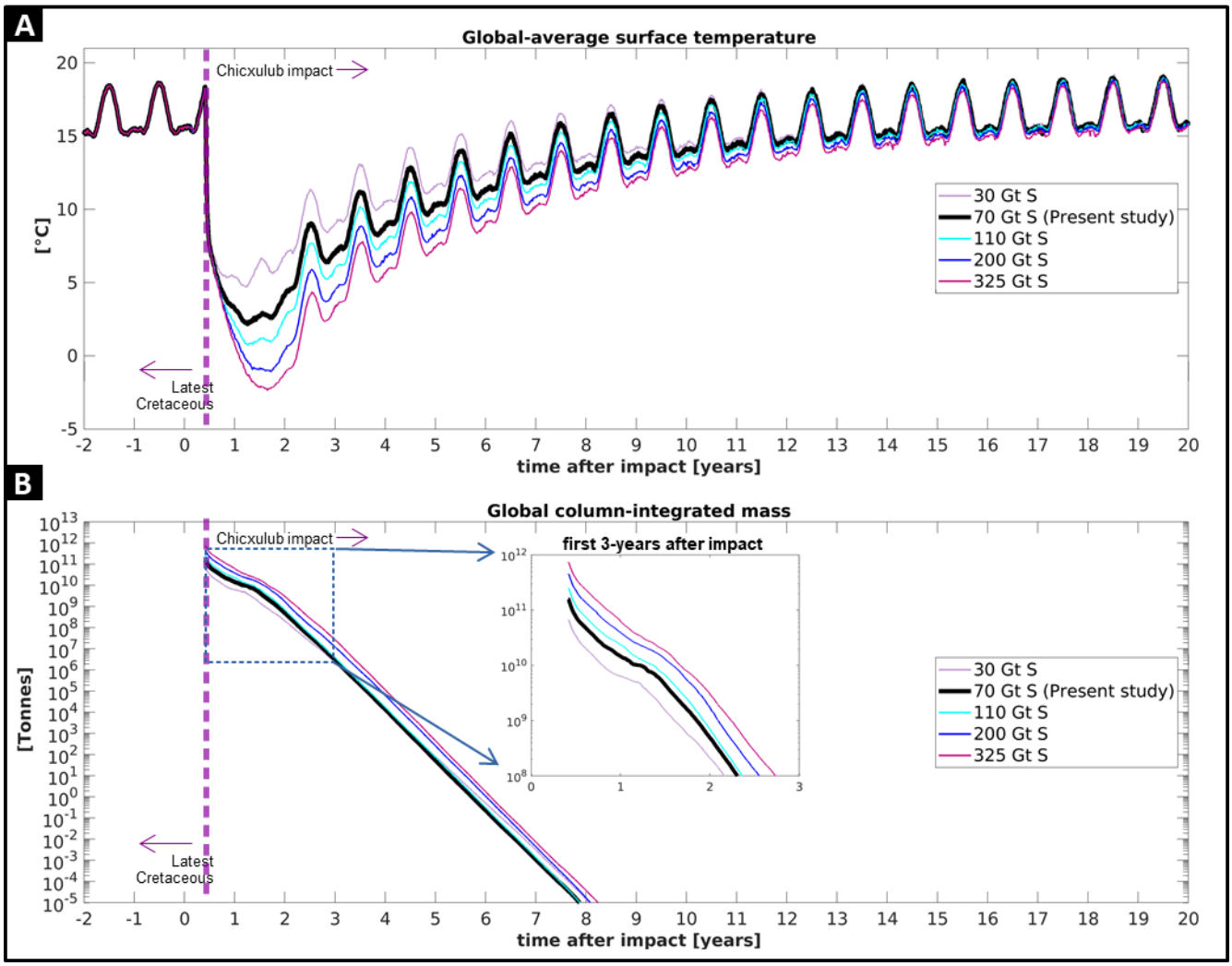

Fig. 4. Simulated temporal evolution of the climatic response related to estimates of the amount of Chicxulub impact-released S. The 0 on the x-axis represents the start of the year of the impact event and the purple dashed line represents the moment of the impact event, during the boreal spring season[96], at approximately 0.25 years on the x-axis. The x-axis represents the time before and after occurrence of the impact, spanning up to 20 years post-impact. In **A** global-average surface temperatures (i.e., surface skin temperature, Ts) and **B** global column-integrated fine-grained ejecta masses are presented for 30, 70, 110, 200, and 325 Gt of impact-released S.

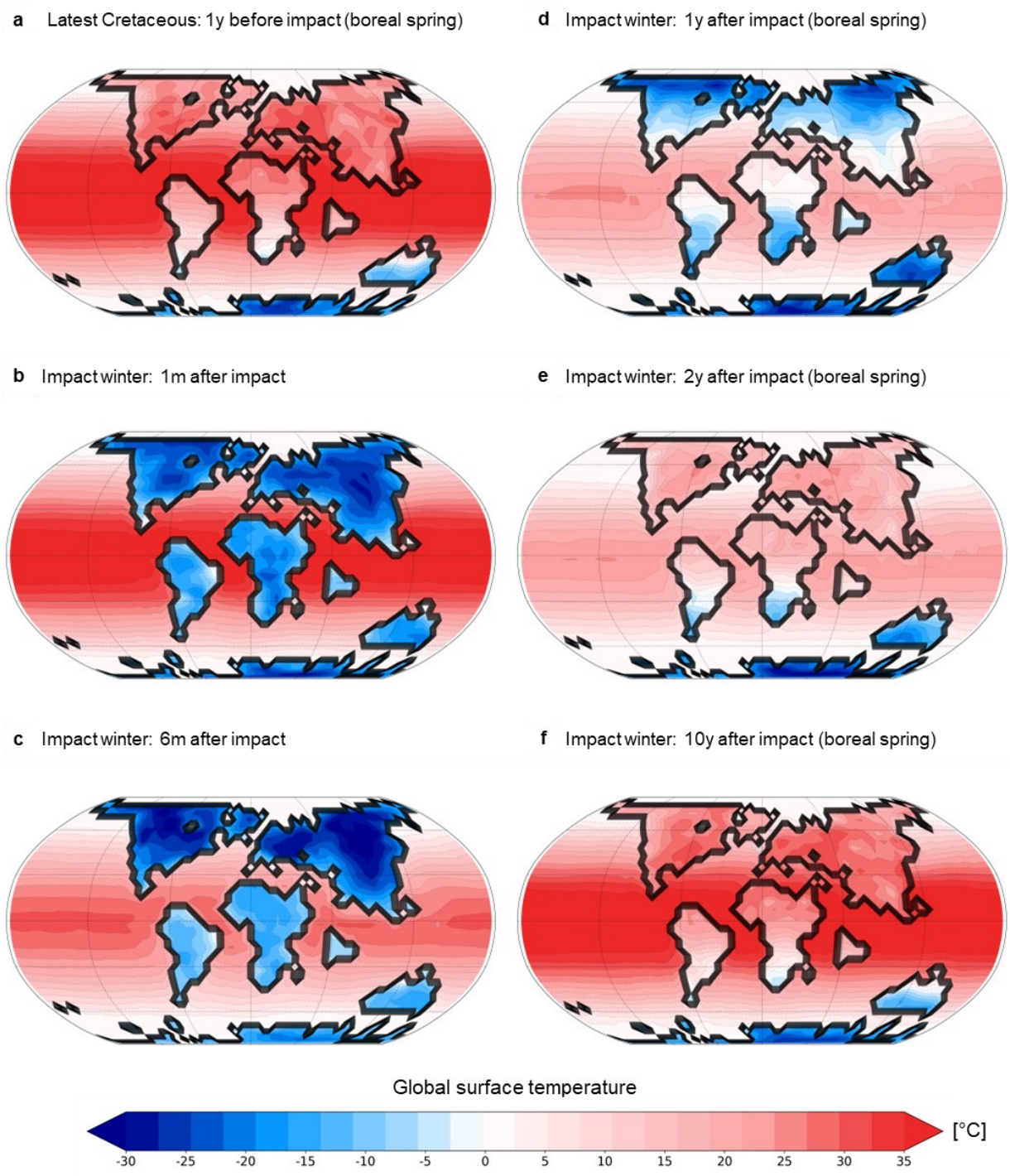

Fig. 5. Simulated global land and ocean surface temperatures (i.e., surface skin temperature, Ts) at different points of time before and after the Chicxulub impact event, using the average estimate of 70

Gt of released S. The time points include: **a)** 1 year before impact as well as **b)** 1 month, **c)** 6 months, **d)** 1 year, **e)** 2 years, and **f)** 10 years after impact.

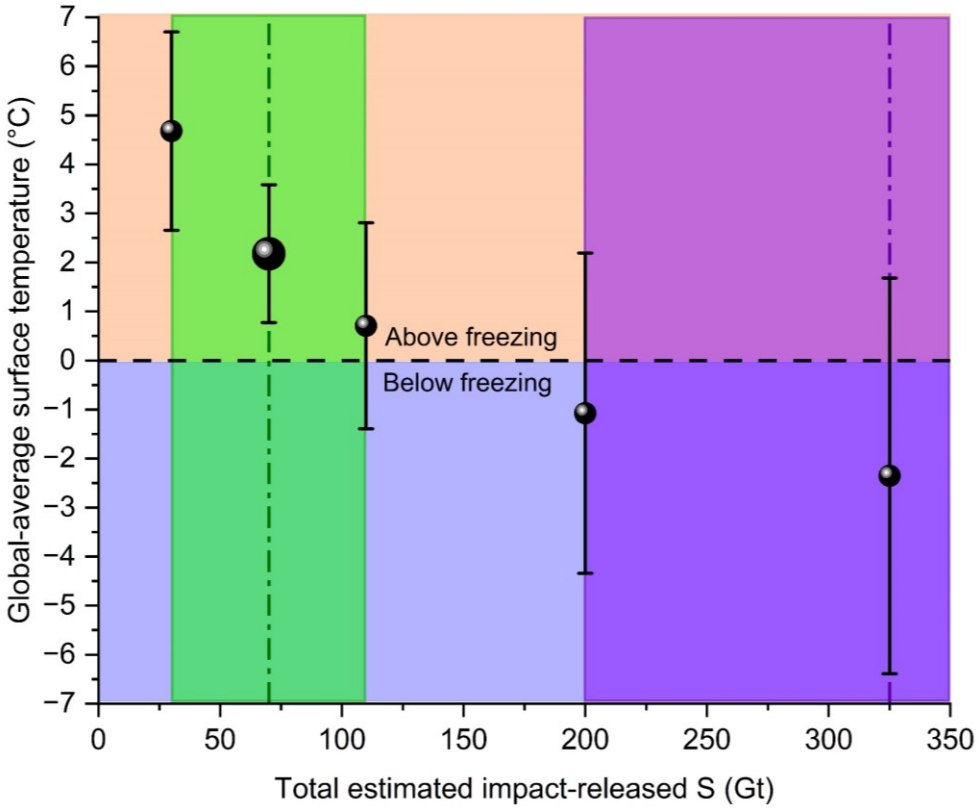

Fig. 6. Global-average surface temperature (Ts) as a function of impact-released S (Gt). The filled circle markers illustrate mean surface temperatures during 0.5-1.5 years after impact, the period with the coldest surface environment. The vertical black bar refers to the range of minimum and maximum temperatures during this timeframe. The green shadowed region highlights the results from the present study (67 ± 39 Gt) while the purple shaded region represents the recently simulated value from Artemieva *et al.* 2017 (325 ± 130 Gt[12]). Temperatures above freezing are represented by an orange region and temperatures below freezing are represented by a blue region.

References

1. Desch, S., Jackson, A., Noviello, J. & Anbar, A. The Chicxulub impactor: comet or asteroid? *Astronomy & Geophysics* **62**, 3.34-3.37 (2021).

2. Gulick, S. P. S. *et al.* Importance of pre-impact crustal structure for the asymmetry of the Chicxulub impact crater. *Nat Geosci* **1**, 131–135 (2008).

3. Jablonski, D. & Chaloner, W. G. Extinctions in the Fossil Record [and Discussion]. *Philosophical Transactions: Biological Sciences* **344**, 11–17 (1994).

4. Kring, D. A. The Chicxulub impact event and its environmental consequences at the Cretaceous-Tertiary boundary. *Palaeogeogr Palaeoclimatol Palaeoecol* **255**, 4–21 (2007).

5. Vajda, V. & Bercovici, A. The global vegetation pattern across the Cretaceous-Paleogene mass extinction interval: A template for other extinction events. *Glob Planet Change* **122**, 29–49 (2014).

6. Vajda, V. & Bercovici, A. The global vegetation pattern across the Cretaceous-Paleogene mass extinction interval: A template for other extinction events. *Glob Planet Change* **122**, 29–49 (2014).

7. Smit, J. & Hertogen, J. An extraterrestrial event at the Cretaceous-Tertiary boundary. *Nature* **285**, 198–200 (1980).

8. Alvarez, L. W., Alvarez, W., Asaro, F. & Michel, H. V. Extraterrestrial Cause for Cretaceous-Tertiary Extinction. Experimental results and theoretical interpretation. *Science* **208**, 1095–1108 (1980).

9. Schulte, P. *et al.* The Chicxulub Asteroid Impact and Mass Extinction at the Cretaceous-Paleogene Boundary. *Science* **327**, 1214–1218 (2010).

10. Vellekoop, J. *et al.* Rapid short-term cooling following the Chicxulub impact at the Cretaceous-Paleogene boundary. *Proc Natl Acad Sci U S A* **111**, 7537–7541 (2014).

11. Chiarenza, A. A. *et al.* Asteroid impact, not volcanism, caused the end-Cretaceous dinosaur extinction. *PNAS* **117**, 17084–17093 (2020).

12. Artemieva, N., Morgan, J. & Expedition 364 Science Party. Quantifying the Release of Climate-Active Gases by Large Meteorite Impacts With a Case Study of Chicxulub. *Geophys Res Lett* **44**, 10,180-10,188 (2017).

13. Senel, C. B. *et al.* Chicxulub impact winter sustained by fine silicate dust. *Nat Geosci* (2023) doi:10.1038/s41561-023-01290-4.

14. Sharpton, V. L., Schuraytz, B. C., Burke, K., Murali, A. V. & Ryder, G. Detritus in K/T boundary clays of western North America; Evidence against a single oceanic impact. *Geological Society of America* **Special paper 247**, 349–357 (1990).

15. Sigurdsson, H., D'hondt, S. & Carey, S. The impact of the Cretaceous/Tertiary bolide on evaporite terrane and generation of major sulfuric acid aerosol. *Earth Planet Sci Lett* **109**, 543–559 (1992).

16. Kaiho, K. *et al.* Global climate change driven by soot at the K-Pg boundary as the cause of the mass extinction. *Sci Rep* **6**, 1–13 (2016).

17. Lyons, S. L. *et al.* Organic matter from the Chicxulub crater exacerbated the K-Pg impact winter. *PNAS* **117**, 25327–25334 (2020).

18. Wolbach, W. S., Lewis, R. S. & Anders, E. Cretaceous Extinctions: Evidence for Wildfires and Search for Meteoritic Material. *Science* **230**, 167–170 (1985).

19. Belcher, C. M., Finch, P., Collinson, M. E., Scott, A. C. & Grassineau, N. V. Geochemical evidence for combustion of hydrocarbons during the K-T impact event. *PNAS* **106**, 4112–4117 (2009).

20. Bardeen, C. G., Garcia, R. R., Toon, O. B. & Conley, A. J. On transient climate change at the Cretaceous−Paleogene boundary due to atmospheric soot injections. *PNAS* **114**, E7415–E7424 (2017).

21. Pierazzo, E., Kring, D. A. & Melosh, H. J. Hydrocode simulation of the Chicxulub impact event and the production of climatically active gases. *J Geophys Res* **103**, 28607–28625 (1998).

22. Pope, K. O., Baines, K. H., Ocampo, A. C. & Ivanov, B. A. Impact winter and the Cretaceous/Tertiary extinctions: Results of a Chicxulub asteroid impact model. *Earth Planet Sci Lett* **128**, 719–725 (1994).

23. Pierazzo, E., Hahmann, A. N. & Sloan, L. C. Chicxulub and Climate: Radiative Perturbations of Impact-Produced S-Bearing Gases. *Astrobiology* **3**, 99–118 (2003).

24. Tabor, C. R., Bardeen, C. G., Otto-Bliesner, B. L., Garcia, R. R. & Toon, O. B. Causes and Climatic Consequences of the Impact Winter at the Cretaceous-Paleogene Boundary. *Geophys Res Lett* **47**, e60121 (2020).

25. Hegg, D. A., Ferek, R. J. & Hobbs, P. V. LIGHT SCATTERING AND CLOUD CONDENSATION NUCLEUS ACTIVITY OF SULFATE AEROSOL MEASURED OVER THE NORTHEAST ATLANTIC OCEAN. *J Geophys Res* **98**, 887–901 (1993).

26. Kremser, S. *et al.* Stratospheric aerosol—Observations, processes, and impact on climate. *Reviews of Geophysics* vol. 54 278–335 Preprint at https://doi.org/10.1002/2015RG000511 (2016).

27. Toon, O. B., Bardeen, C. & Garcia, R. Designing global climate and atmospheric chemistry simulations for 1 and 10 km diameter asteroid impacts using the properties of ejecta from the K-Pg impact. *Atmos Chem Phys* **16**, 13185–13212 (2016).

28. Brugger, J., Feulner, G. & Petri, S. Baby, it's cold outside: Climate model simulations of the effects of the asteroid impact at the end of the Cretaceous. *Geophys Res Lett* **44**, 419–427 (2017).

29. Gulick, S. P. S. *et al.* The first day of the Cenozoic. *PNAS* **116**, 19342–19351 (2019).

30. Junium, C. K. *et al.* Massive perturbations to atmospheric sulfur in the aftermath of the Chicxulub impact. *PNAS* **119**, 1–7 (2022).

31. Glasspool, I. J. & Scott, A. C. Phanerozoic concentrations of atmospheric oxygen reconstructed from sedimentary charcoal. *Nat Geosci* **3**, 627–630 (2010).

32. Whitehill, A. R., Jiang, B., Guo, H. & Ono, S. SO2 photolysis as a source for sulfur mass-independent isotope signatures in stratospheric aerosols. *Atmos Chem Phys* **15**, 1843–1864 (2015).

33. Tilmes, S. *et al.* Sensitivity of aerosol distribution and climate response to stratospheric SO2 injection locations. *Journal of Geophysical Research: Atmospheres* **122**, 591–615 (2017).

34. Brett, R. The Cretaceous-Tertiary extinction: A lethal mechanism involving anhydrite target rocks. *Geochim Cosmochim Acta* **56**, 3603–3606 (1992).

35. Chen, G., Tyburczy, J. A. & Ahrens, T. J. Shock-induced devolatilization of calcium sulfate and implications for K-T extinctions. *Earth Planet Sci Lett* **128**, 615–628 (1994).

36. Ivanov, B. A. *et al.* Degassing of sedimentary rocks due to Chicxulub impact: Hydrocode and physical simulations. *Geological Society of America* **Special paper 307**, 125–139 (1996).

37. Toon, O. B., Zahnle, K., Morrison, D., Turco, R. P. & Covey, C. Environmental perturbations caused by the impacts of asteroids and comets. *Reviews of Geophysics* **35**, 41–78 (1997).

38. Morgan, J. *et al.* Size and morphology of the Chicxulub impact crater. *Nature* **390**, 472–476 (1997).

39. Dressler, B. O. *et al.* Investigating a 65-Ma-Old smoking gun: Deep drilling of the Chicxulub impact structure. *Eos* **84**, 125–136 (2003).

40. Belza, J., Goderis, S., Keppens, E., Vanhaecke, F. & Claeys, P. An emplacement mechanism for the mega-block zone within the Chicxulub crater, (Yucatán, Mexico) based on chemostratigraphy. *Meteorit Planet Sci* **47**, 400–413 (2012).

41. Kenkmann, T., Wittmann, A. & Scherler, D. Structure and impact indicators of the Cretaceous sequence of the ICDP drill core Yaxcopoil-1, Chicxulub impact crater, Mexico. *Meteorit Planet Sci* **39**, 1069–1088 (2004).

42. Ramos, E. L. Geological Summary of the Yucatan Peninsula. in *The Gulf of Mexico and the Caribbean257–282* (eds. Nairn, A. E. M. & Stehli, F. G.) 257–282 (Springer, Boston, MA, 1975). doi:10.1007/978-1-4684-8535-6_7.

43. Urrutia-Fucugauchi, J., Marin, L. & Trejo-Garcia, A. UNAM Scientific drilling program of Chicxulub impact structure - Evidence for a 300 kilometer crater diameter. *Geophys Res Lett* **23**, 1565–1568 (1996).

44. Rebolledo-Vieyra, M. & Urrutia-Fucugauchi, J. Magnetostratigraphy of the Cretaceous/Tertiary boundary and early Paleocene sedimentary sequence from the Chicxulub Impact Crater. *Earth Planets Space* **58**, 1309–1314 (2006).

45. Morgan, J. V. *et al.* The formation of peak rings in large impact craters. *Science* **354**, 878–882 (2016).

46. Paytan, A., Kastner, M., Campbell, D. & Thiemens, M. H. Seawater Sulfur Isotope Fluctuations in the Cretaceous. *Science* **304**, 1663–1665 (2004).

47. Witts, J. D. *et al.* The impact of the Cretaceous–Paleogene (K–Pg) mass extinction event on the global sulfur cycle: Evidence from Seymour Island, Antarctica. *Geochim Cosmochim Acta* **230**, 17–45 (2018).

48. Schmitz, B., Andersson, P. & Dahl, J. Iridium, sulfur isotopes and rare earth elements in the Cretaceous-Tertiary boundary clay at Stevns Klint, Denmark. *Geochim Cosmochim Acta* **52**, 229–236 (1988).

49. Kajiwara, Y. & Kaiho, K. Oceanic anoxia at the Cretaceous/Tertiary boundary supported by the sulfur isotopic record. *Palaeogeogr Palaeoclimatol Palaeoecol* **99**, 151–162 (1992).

50. Heymann, D. *et al.* Geochemical markers of the Cretaceous-Tertiary boundary event at Brazos River, Texas, USA. *Geochim Cosmochim Acta* **62**, 173–181 (1998).

51. Kaiho, K. *et al.* Oceanic primary productivity and dissolved oxygen levels at the Cretaceous/Tertiary boundary: Their decrease, subsequent warming, and recovery. *Paleoceanography* **14**, 511–524 (1999).

52. Maruoka, T., Koeberl, C., Newton, J., Gilmour, I. & Bohor, B. F. Sulfur isotopic compositions across terrestrial Cretaceous-Tertiary boundary successions. *Geological Society of America* **Special Paper 356**, 337–344 (2002).

53. Schaefer, B. *et al.* Microbial life in the nascent Chicxulub crater. *Geology* **48**, 328–332 (2020).

54. Kring, D. A., Whitehouse, M. J. & Schmieder, M. Microbial Sulfur Isotope Fractionation in the Chicxulub Hydrothermal System. *Astrobiology* **21**, 103–114 (2021).

55. Holmes, C. W. & Bohor, B. F. Stable isotope (C, S, N) distributions in coals spanning the Cretaceous/Tertiary boundary in the Raton Basin, Colorado and New Mexico [abs.]. *U.S. Geological Survey Circular* **1107**, 141 (1994).

56. Cousineau, M. L. Tracing biogeochemical processes using sulfur stable isotopes: two novel applications. (University of Ottawa, Ottawa, Ontario, 2013).

57. Bourgeois, J., Hansen, T. A., Wiberg, P. L. & Kauffman, E. G. A Tsunami Deposit at the Cretaceous-Tertiary Boundary in Texas. *Science (1979)* **241**, 567–570 (1988).

58. Smit, J. *et al.* Coarse-grained, clastic sandstone complex at the K/T boundary around the Gulf of Mexico: Deposition by tsunami waves induced by the Chicxulub impact? in *The Cretaceous-Tertiary Event and Other Catastrophes in Earth History* (eds. Ryder, G., Fastovsky, D. & Gartner, S.) vol. Special Paper 307 151–182 (Geological Society of America, Boulder, Colorado, 1996).

59. Gale, A. S. The Cretaceous—Palaeogene boundary on the Brazos River, Falls County, Texas: is there evidence for impact-induced tsunami sedimentation? *Proceedings of the Geologists' Association* **117**, 173–185 (2006).

60. Schulte, P., Speijer, R., Mai, H. & Kontny, A. The Cretaceous-Paleogene (K-P) boundary at Brazos, Texas: Sequence stratigraphy, depositional events and the Chicxulub impact. *Sediment Geol* **184**, 77–109 (2006).

61. Sharpton, V. L. *et al.* A model of the Chicxulub impact basin based on evaluation of geophysical data, well logs, and drill core samples. *Geological Society of America* **Special Paper 307**, 55–74 (1996).

62. Claeys, P., Heuschkel, S., Lounejeva-Baturina, E., Sanchez-Rubio, G. & Stöffler, D. The suevite of drill hole Yucatàn 6 in the Chicxulub impact crater. *Meteorit Planet Sci* **38**, 1299–1317 (2003).

63. Strauss, H. & Deutsch, A. The Chicxulub event—sulfur-bearing minerals and lithologies. *Geophysical Research Abstracts* **5**, (2003).

64. Paytan, A. & Gray, E. T. Sulfur isotope stratigraphy. in *The Geologic Time Scale 2012* (eds. Gradstein, F. M., Ogg, J. G., Schmitz, M. & Ogg, G.) 167–180 (Elsevier B.V., 2012). doi:10.1016/B978-0-444-59425-9.00009-3.

65. Kaskes, P. *et al.* Formation of the crater suevite sequence from the Chicxulub peak ring: A petrographic, geochemical, and sedimentological characterization. *GSA Bulletin* **134**, 895–927 (2022).

66. Kring, D. A. *et al.* Probing the hydrothermal system of the Chicxulub impact crater. *Sci. Adv* **6**, 3053–3082 (2020).

67. Kaskes, P., Marchegiano, M., Peral, M., Goderis, S. & Claeys, P. Hot carbonates deep within the Chicxulub impact structure. *PNAS Nexus* **3**, 1–14 (2024).

68. Goderis, S. *et al.* Globally distributed iridium layer preserved within the Chicxulub impact structure. *Sci Adv* **7**, 1–13 (2021).

69. Vellekoop, J. *et al.* Shelf hypoxia in response to global warming after the Cretaceous-Paleogene boundary impact. *Geology* **46**, 683–686 (2018).

70. DePalma, R. A. *et al.* A seismically induced onshore surge deposit at the KPg boundary, North Dakota. *Proc Natl Acad Sci U S A* **116**, 8190–8199 (2019).

71. Goderis, S. *et al.* Reevaluation of siderophile element abundances and ratios across the Cretaceous-Paleogene (K-Pg) boundary: Implications for the nature of the projectile. *Geochim Cosmochim Acta* **120**, 417–446 (2013).

72. Di, P. *et al.* Carbonate-associated sulfate as an archive of sulfur and oxygen stable isotope composition of seawater sulfate: Evidence from reef carbonate rocks of the southern South China Sea. *Chem Geol* **638**, 121699 (2023).

73. Range, M. M. *et al.* The Chicxulub Impact Produced a Powerful Global Tsunami. *AGU Advances* **3**, (2022).

74. Habicht, K. S., Gade, M., Thamdrup, B., Berg, P. & Canfield, D. E. Calibration of Sulfate Levels in the Archean Ocean. *Science (1979)* **298**, 2372–2374 (2002).

75. Sim, M. S., Bosak, T. & Ono, S. Large Sulfur Isotope Fractionation Does Not Require Disproportionation. *Science (1979)* **333**, 74–77 (2011).

76. Sim, M. S. *et al.* What Controls the Sulfur Isotope Fractionation during Dissimilatory Sulfate Reduction? *ACS Environmental Au* **3**, 76–86 (2023).

77. Tino, C. J. *et al.* Are Large Sulfur Isotope Variations Biosignatures in an Ancient, Impact-Induced Hydrothermal Mars Analog? *Astrobiology* **23**, 1027–1044 (2023).

78. Xu, Y. *et al.* Multiple S-isotopic evidence for seawater incursions during the deposition of the upper Cretaceous source rocks in the Songliao Basin, northeastern China. *Chem Geol* **642**, 121790 (2023).

79. Upchurch, G. R., Kiehl, J., Shields, C., Scherer, J. & Scotese, C. Latitudinal temperature gradients and high-latitude temperatures during the latest Cretaceous: Congruence of geologic data and climate models. *Geology* **43**, 683–686 (2015).

80. O'Brien, C. L. *et al.* Cretaceous sea-surface temperature evolution: Constraints from TEX86 and planktonic foraminiferal oxygen isotopes. *Earth Sci Rev* **172**, 224–247 (2017).

81. Niezgodzki, I., Knorr, G., Lohmann, G., Tyszka, J. & Markwick, P. J. Late Cretaceous climate simulations with different CO2 levels and subarctic gateway configurations: A model-data comparison. *Paleoceanography* **32**, 980–998 (2017).

82. Vellekoop, J. *et al.* Type-Maastrichtian gastropod faunas show rapid ecosystem recovery following the Cretaceous–Palaeogene boundary catastrophe. *Palaeontology* **63**, 349–367 (2020).

83. Alegret, L., Arreguín-Rodríguez, G. J. & Thomas, E. Oceanic productivity after the Cretaceous/Paleogene impact: Where do we stand? The view from the deep. in *From the Guajira Desert to the Apennines, and from Mediterranean Microplates to the Mexican Killer Asteroid: Honoring the Career of Walter Alvarez, Christian Koeberl, Philippe Claeys, Alessandro Montanari* vol. Special Paper 557 449–470 (The Geological Society of America, 2022).

84. Robertson, D. S., Lewis, W. M., Sheehan, P. M. & Toon, O. B. K-Pg extinction patterns in marine and freshwater environments: The impact winter model. *J Geophys Res Biogeosci* **118**, 1006–1014 (2013).

85. Whittle, R. J. *et al.* Nature and timing of biotic recovery in Antarctic benthic marine ecosystems following the Cretaceous–Palaeogene mass extinction. *Palaeontology* **62**, 919–934 (2019).

86. Sheehan, P. M. & Fastovsky, D. E. Major extinctions of land-dwelling vertebrates at the Cretaceous- Tertiary boundary, eastern Montana. *Geology* **20**, 556–560 (1992).

87. Schueth, J. D., Bralower, T. J., Jiang, S. & Patzkowsky, M. E. The role of regional survivor incumbency in the evolutionary recovery of calcareous nannoplankton from the Cretaceous/ Paleogene (K/Pg) mass extinction. *Paleobiology* **41**, 661–679 (2015).

88. Wolfe, J. A. Late Cretaceous-Cenozoic History of Deciduousness and the Terminal Cretaceous Event. *Paleobiology* **13**, 215–226 (1987).

89. Sheehan, P. M. & Hansen, T. A. Detritus Feeding as a Buffer to Extinction at the End of the Cretaceous. *Geology* **14**, 868–870 (1986).

90. Hughes, J. J., Berv, J. S., Chester, S. G. B., Sargis, E. J. & Field, D. J. Ecological selectivity and the evolution of mammalian substrate preference across the K–Pg boundary. *Ecol Evol* **11**, 14540–14554 (2021).

91. Longrich, N. R., Bhullar, B. A. S. & Gauthier, J. A. Mass extinction of lizards and snakes at the Cretaceous-Paleogene boundary. *PNAS* **109**, 21396–21401 (2012).

92. Longrich, N. R., Tokaryk, T. & Field, D. J. Mass extinction of birds at the cretaceous-paleogene (K-Pg) boundary. *PNAS* **108**, 15253–15257 (2011).

93. Longrich, N. R., Scriberas, J. & Wills, M. A. Severe extinction and rapid recovery of mammals across the Cretaceous-Palaeogene boundary, and the effects of rarity on patterns of extinction and recovery. *J Evol Biol* **29**, 1495–1512 (2016).

94. Wilson, G. P. Mammals across the K/Pg boundary in northeastern Montana, U.S.A.: Dental morphology and body-size patterns reveal extinction selectivity and immigrant-fueled ecospace filling. *Paleobiology* **39**, 429–469 (2013).

95. Lovegrove, B. G., Lobban, K. D. & Levesque, D. L. Mammal survival at the Cretaceous–Palaeogene boundary: Metabolic homeostasis in prolonged tropical hibernation in tenrecs. *Proceedings of the Royal Society B* **281**, 20141304 (2014).

96. During, M. A. D. *et al.* The Mesozoic terminated in boreal spring. *Nature* **603**, 91–94 (2022).

Materials and methods

Sample materials

All samples analyzed in this study are pulverized aliquots of samples used in prior studies. In previous publications reporting on these studies, field collection, removal of external debris, homogenization, and geophysical and geochemical characterization are explained in detail[9,39,43,45,62,69,71,97,98]. A full

overview, including sample identification and lithological information, for all the samples characterized in this study is provided in Tables S1 and S2 in the SI.

Bulk S concentration and S isotope ratio determination

Sample preparation and analysis – including digestion, chromatographic S isolation, S and siderophile element concentration determination, and S isotope ratio measurements – were carried out at the UGent-A&MS laboratory at Ghent University in Ghent, Belgium, and the ALS Scandinavia AB laboratory in Luleå, Sweden. All sample preparations at both labs were carried out in clean laboratory areas and followed the procedures described in detail in Rodiouchkina *et al.* 2023[99].

To minimize waste of precious samples, preliminary S concentrations were obtained by non-destructive micro X-ray fluorescence spectrometry (μXRF) for all samples and these concentrations were relied on to select the sample weights to be used for analysis. The μXRF measurements were carried out using an M4 Tornado benchtop μXRF surface scanner (Bruker nano GmbH, Germany) with a Rh X-ray source at the AMGC Laboratory at the Vrije Universiteit Brussel in Brussels, Belgium[100,101].

For drill core samples that consisted for a large part of anhydrite (UNAM and Yax-1), sample amounts of ~10 mg were digested by adding 3 M HCl until no powder residue was observed. Aliquots of the sample digests were used for concentration determination. The digest was then diluted to 0.24 M HCl and loaded onto a conditioned cation exchange chromatography resin (Dowex 50W-X8), through which S, in the form of sulfate, passes, while the matrix cations are removed from the matrix by strong adsorption onto the resin. All other samples and matrix-matched elemental certified reference materials, soil (GBW07410), river sediment (NIST SRM 2704), and brick clay (NIST SRM 679), were digested using *aqua regia* (3:1 HCl:HNO_3) in closed beakers on a 110°C hot plate for >24 h. Aliquots of the standard and sample digests were used for concentration determination. The digests were evaporated at 70°C and residuals were taken up in 0.24 M HCl before S was separated from matrix cations using the

cation exchange protocol mentioned above. As many of these samples have a low S content (10 to 1,000 μg g^{-1}) compared to matrix elements, the eluates were purified by submitting them to a second round of this cation exchange protocol, followed by an anion exchange chromatography protocol to separate S from residual matrix oxyanions. This protocol consisted of sulfate and other oxyanions adsorbing onto the anion exchange resin (AG-1-X8) and matrix cations passing through the column at 0.03 M HNO_3, followed by sulfate elution at 0.3 M HNO_3. Aliquots of all solutions were taken for S concentration determination after digestion, but also for assuring that the recovery of S was >95% after chemical purification.

Determination of the concentrations of S and matrix elements was carried out using single-collector double-focusing inductively coupled plasma-sector field mass spectrometry (ICP-SFMS). Element XR (Thermo Fisher Scientific, Germany) instruments were used for this purpose at the UGent-A&MS laboratory and at the ALS laboratory. Sulfur isotope ratios were determined using multi-collector inductively coupled plasma-mass spectrometry (MC-ICP-MS) using a Neptune XT (Thermo Fisher Scientific, Germany) at the UGent-A&MS laboratory (determination of both $\delta^{34}S$ and $\delta^{33}S$) and using a Neptune Plus, at the ALS laboratory (determination of $\delta^{34}S$ only). In both cases, an Aridus II (Teledyne CETAC Technologies, USA) desolvating sample introduction system was used.

All S isotope ratios obtained ($^{34}S/^{32}S$ and $^{33}S/^{32}S$), are presented using the δ-notation according to equation 1, expressing deviations with respect to the international standard Vienna-Canyon Diablo Troilite (V-CDT) in per mil (‰). The given '‰' values are equivalent to 'mUr' (milliUrey[87]). Correction for the bias caused by instrumental mass discrimination was accomplished as described in Rodiouchkina *et al.* 2023[99]. Mass-independent anomalies are presented using the MIF tracer, $\Delta^{33}S$, which is calculated according to equation 2.

$$\delta^{3x}S = \left(\frac{(^{3x}S/^{32}S)_{sample}}{(^{3x}S/^{32}S)_{V-CDT}} - 1\right) \times 1000 \quad (1)$$

$$\Delta^{33}S = \delta^{33}S - 0.515 \times \delta^{34}S \quad (2)$$

Accuracy of the $\delta^{34}S$ values was assessed using International Atomic Energy Agency (IAEA) Ag_2S reference materials S1 ($\delta^{34}S$ = −0.30 ‰), S2 ($\delta^{34}S$ = +22.62 ‰), and S3 ($\delta^{34}S$ = −32.49 ‰) and both the $\delta^{34}S$ and $\delta^{33}S$ values using the recently produced ^{33}S-enriched $NaSO_4$ standards[102] S-MIF-1 ($\delta^{34}S$ = +10.26 ‰, $\delta^{33}S$ = +14.81 ‰, $\Delta^{33}S$ = +9.54 ‰) and S-MIF-2 ($\delta^{34}S$ = +21.53 ‰, $\delta^{33}S$ = +22.42 ‰, $\Delta^{33}S$ = +11.39 ‰). The IAEA standards were digested following the procedure described by Craddock *et al.* 2008[103] and Rodiouchkina *et al.* 2023[99], according to which 5 mL of 7 M HNO_3 was added to the standards and the mixture left to evaporate to dryness on a 70°C hot plate. The dry residue was further digested and Ag precipitated using 3 mL of concentrated HNO_3 and 2 mL of 6 M HCl before taking the mixture to dryness on a 70°C hot plate again. When dry, the residuals were taken up with 0.24 M HCl and chemically purified in the same way as the samples. The MIF standards were dissolved using 0.24 M HCl and S was isolated using the same chemical purification method as used for the samples.

The expanded uncertainty (U) is calculated using the sum square approach[104,105,106] according to equation (3), where u_c is the combined uncertainty of the internal precision of one measurement (SD_{int}), the within-session repeatability (SD_{within}), the between-session repeatability ($SD_{between}$), and the repeatability between separate sample preparations (SD_{sample_prep}). These were estimated using matrix-matched standards and by digesting at least one sample of each lithology more than once.

$$U = k \times u_c = 2 \times \sqrt{SD_{int}^2 + SD_{within}^2 + SD_{between}^2 + SD_{sample\_prep}^2} \quad (3)$$

Total reduced inorganic S and sulfide isotope ratio determination

Chromium-reducible sulfur (CRS; essentially pyrite; FeS_2), was extracted with hot acidic Cr(II)chloride solution (Fossing and Jørgensen, 1989[107]). The released H_2S was precipitated as ZnS and then total reduced inorganic S (TRIS) was determined spectrophotometrically (Specord 40 spectrophotometer) following the method of Cline[108]. For sulfur isotope ratio ($^{34}S/^{32}S$) determination, the ZnS was converted to Ag_2S by the addition of 0.1 M $AgNO_3$ solution with subsequent filtration, washing, and drying of the Ag_2S precipitate. Isotope ratio measurements were carried out using CirmMS using a Thermo elemental analyzer connected to a Thermo Finnigan MAT 253 gas isotope ratio mass spectrometer via a Thermo ConFlo IV split interface in the BGC lab at IOW. IAEA-S1, -S2, -S3, and NBS127 isotopic reference materials were used to calibrate the mass spectrometric signals[109].

Calculation of the estimated amount of impact-vaporized S

The estimated amount of impact-vaporized S is calculated by combining traditional isotope dilution and mass balance calculations. In the post-impact winter hypothesis, S-species injected into the atmosphere following the Chicxulub impact event would first distribute globally, causing cooling and darkness before they would gradually return to the Earth's surface via dry or wet deposition processes. In bedrock with naturally low S content and a $\delta^{34}S$ value significantly different from that of the sulfate aerosols related to vaporized target anhydrite, the global event is recorded in the impact event deposit sediments as a S offset in both the S concentration and the $\delta^{34}S$ value. The thickness of the post-impact event deposits is dependent on the sedimentation rate, but also on the state of preservation of the record. To determine the amount of S released during the Chicxulub impact event, sediment profiles of K-Pg boundary sites outside of the impact crater were therefore investigated for possible positive offsets due to deposition of the ejected S. The K-Pg boundary sites selected all contain the classic ejecta layer, comprising markers such as microkrystites, shocked quartz and the positive iridium anomaly[68,69,71] .

For example, a clear positive spike in both the S concentration and the $\delta^{34}S$ value is observed at the terrestrial Tanis (North Dakota, USA) site (Fig. 2E; Fig. S3 in the SI). We assume that impact-deposited S is solely responsible for this offset and that the S concentration and $\delta^{34}S$ value in the sediment profile before this spike represents the background values for this site, not attributable to atmospheric S deposition. These background values are therefore subtracted to obtain the S concentration (equation 4) and $\delta^{34}S$ value (equation 5) stemming from post-impact atmospheric deposition at the K-Pg boundary sites. The amount of ^{34}S-enriched impact event deposition in each sediment sample at the K-Pg boundary sites ($C_{Deposit\ per\ sample}$) is then calculated for each profile interval by multiplying the background-corrected offset S concentration ($C_{K-Pg\_site\_deposit}$) with the ratio of the background-corrected $\delta^{34}S$ value related to the K-Pg boundary site ($\delta^{34}S_{K-Pg\_site\_deposit}$) to that of the target anhydrites ($\delta^{34}S_{Impact-target}$) according to equation 6. This amount ($C_{Deposit\ per\ sample}$) is then multiplied by the density determined gravimetrically (or average tabulated values taken for each lithology type) at each sample point in the profile ($\rho_{For\ each\ sample\ in\ profile}$) and subsequently integrated across the entire profile using the vertical thickness of each sample unit ($VL_{Per\ sample}$) to obtain the amount of impact-deposited S collected over the entire K-Pg site profile ($M_{Deposit\ over\ entire\ profile}$) according to equation 7. The total amount of impact-vaporized S is calculated by extrapolating this value to the entire surface of the Earth (A_{Earth}=510000000 km^2), assuming equal global deposition, according to equation 8. The reported uncertainty on this value is calculated using the 2SD and expanded uncertainties of the $\delta^{34}S$ values for the target anhydrite as well as for the measured S concentration and $\delta^{34}S$ value of the sample points in the distal site profile.

$$C_{K-Pg\_site\_deposit} = C_{K-Pg\_site\_total} - C_{K-Pg\_site\_background} \quad (4)$$

$$\delta^{34}S_{K-Pg\_site\_deposit} = \delta^{34}S_{K-Pg\_site\_total} - \delta^{34}S_{K-Pg\_site\_background} \quad (5)$$

$$C_{Deposit\ per\ sample} = C_{K-Pg\_site\_deposit} \times \frac{\delta^{34}S_{K-Pg\_site\_deposit}}{\delta^{34}S_{Impact-target}} \quad (6)$$

$$M_{Deposit\ over\ entire\ profile} = \sum(C_{Deposit\ per\ sample} \times \rho_{For\ each\ sample\ in\ profile} \times VL_{Per\ sample}) \quad (7)$$

$$M_{Total\ imact-released} = M_{Deposit\ over\ entire\ profile} \times A_{Earth} \quad (8)$$

Description of the paleoclimate modeling simulation

A detailed description of the paleoclimate modeling simulation can be found in Senel *et al*. 2023[13]. The only parameter changed in the present study is the newly estimated amount of impact-released S. Simulations were performed using average, minimum, and maximum empirical estimates of the amount of impact-released S (70, 30, 110 Gt, respectively), as well as the average and minimum value for the recently simulated value from Artemieva *et al.*, 2017 [12] of 325 ± 130 Gt (325 and 200 Gt, respectively). To estimate a threshold value for global effects, also the effects of injection of 1 and 5 Gt of impact-released S were simulated, with 1 Gt causing regional effects only and 5 Gt leading to global effects (Fig. S15 in SI), indicating that the threshold value falls in-between 1 and 5 Gt S.

The model used here[13] is a 3D atmospheric general circulation model (AGCM) coupled with a simplified ocean mixed layer (OML) parameterization[110–112], implementing PaleoEarth[13,113] into the planetWRF (Weather, Research and Forecasting) general-purposes planetary atmosphere model[114,115]. It is specialized in simulating atmospheric conditions as a result of the Chicxulub impact event at the K-Pg boundary using the latest Cretaceous paleogeography for boundary conditions[116] and simplified plant functional types to describe surface conditions on land areas[81]. This model comprises three major components. The first module governs the atmospheric transport dynamics of impact-generated ejecta (here consisting of sulfur), the second covers radiative transfer following the impact, and the third module models the microphysical processes of the impact ejecta. The second module includes impact-ejecta induced radiative effects, such as the absorption, reflection, and scattering of the shortwave and longwave spectrum by ejected particles, implemented within the NASA Goddard shortwave/longwave radiation scheme[117,118]. Here, the specific extinction, single scattering albedo and asymmetry factor for

sulfate were set as a function of the wavelength in 8 and 3 spectral bands in shortwave and longwave ranges of the spectrum, respectively[119]. The third module focuses on the microphysics of the impact-ejecta, such as dry and wet deposition processes of the sulfur, soot, and silicate dust. Understanding the atmospheric deposition is essential for determining the lifespan of the impact-ejected particles in the atmosphere. The modeling assumed monodisperse sulfate. For sulfate particles, the dry deposition rate was set to 0.1 cm/s on land and ocean fitting within previously reported values[119,120]. No photochemical reactions were included in the sulfur cycle simulations, as a maximum scenario was assumed, according to which the injected S is fully converted into sulfate in the atmosphere. The wet deposition is modeled by representing washout and in-cloud rainout processes[121,122]. The design of S emission configuration is described in Senel *et al*. 2023[13].

The current paleoclimate model involves a WRF five-layer thermal diffusion scheme to model land-surface physics[123]. Purdue-Lin microphysics scheme is used to employ water cycle, cloud, and precipitation microphysics[124]. The modified Tiedtke scheme is used to resolve the cumulus parameterization[125,126]. To model planetary boundary layer (PBL) turbulence, a stability-aware one-and-a-half-order turbulence kinetic energy (TKE) closure is used[127], and the revised MM5 scheme to model the atmospheric surface layer[128].

Regarding ocean modelling, an ocean mixed layer model (WRF-OML) [110–112] was used. The WRF-OML is a single layer one-dimensional ocean parameterization that involves wind stress induced mixing and mixed layer deepening in the ocean. 3D ocean models are capable of resolving oceanic circulations from surface to deep oceanic layers, providing detailed information from marine biogeochemistry to the carbon cycle, thus the ocean acidification. One challenge for 3D models is their computationally-heavy nature with a long model spin-up period of 1000s of years[81]. Additionally, the number of unknowns in physical parameterizations substantially increases, primarily tuned for present oceans. Unlike 3D ocean models, the horizontal advection (meridional or zonal) is not accounted for in

1D ocean mixed layer models (e.g., WRF-OML, here). In other words, the mixing process in WRF-OML is redistributed vertically, being confined in the ocean mixed layer, and no heat transport occurs across horizontal grid points, as a model limitation. Therefore, to ensure the validity of the simplified ocean parameterization (WRF-OML), simulated surface temperatures before emitting impact ejecta were validated with proxy-based latest Cretaceous temperature reconstructions[79], see the pre-impact model-proxy comparison in Extended Data Fig. 4 from Senel *et al.* 2023[13].

The WRF-OML solves the heat exchange between the atmospheric boundary layer (ABL) and ocean mixed layer (OML), incorporating wind stresses, buoyancy fluxes, and the evolution of mixed layer depth as a function of the Richardson number for turbulent instabilities. Consequently, there are two parameters to prescribe, the initial mixed layer depth and deep layer thermal lapse rate. The initial condition for the mixed layer depth is assumed to be homl=100 m, while the deep layer thermal lapse rate is Γoml=0.14 K/m.

The current model does not include a sea ice model considering the temperate greenhouse climate of the Late Cretaceous based on multiple lines of evidence from paleoclimatic proxies[79], and paleontological records. For example, the palynological and macrofloral evidence[129–131] indicates that the coastal lowlands of Antarctica were covered by podocarp-dominated cool to warm-temperate rainforests, inhabited by various (thermophyllic) reptiles, including non-avian dinosaurs[132]. Paleoclimate proxy data (e.g. the organic-biomarker based paleothermometer MBT-CBT) suggests that these regions were characterized by mean annual air temperatures of 10-15°C[131,133] during these times. These data are inconsistent with the frigid winter temperatures required to build up sea ice. Likewise, the presence of marine reptiles such as plesiosaurs and mosasaurs[132], and a fish assemblage dominated by temperate to subtropical taxa of sharks and teleostid fish[134] in the Late Maastrichtian López de Bertodano Fm on Vega Island and Seymour Island, Antarctica is inconsistent with extensive sea ice build-up. Rather, a compilation of TEX86 and planktic foraminiferal $\delta^{18}O$ paleothermometry data[135]

suggests that higher latitudes were characterized by sea surface temperatures of 5-10°C, while clumped-isotope thermometry based on fossil mollusc carbonate indicates mean annual sea water temperatures of 7-9°C around Antarctica just prior to the impact[136], similarly inconsistent with the presence of sea-ice in the latest Cretaceous. However, it may play a critical role post-impact when global surface temperatures drop to freezing levels that could initiate the formation of sea ice in polar oceans. Previous AOGCM simulations[28] analyzed the post-impact sea ice fraction depending on three different stratospheric aerosol residence times (2.1, 4.3, and 10.6 years). Those simulations assumed S emission (100 Gt) in a 500 ppm CO_2 atmosphere, resulting in <34% and <17% of global sea ice fraction for the residence times of 10.6 and 4.3 years, with a global surface air temperature (Ta) minimum of -15°C and -11°C, respectively. In the present study, the S residence time is <7.5 years, which may fall in-between the residence times of 10.6 and 4.3 years, corresponding to an average of <25% global sea ice fraction based on the results of Brugger *et al.* 2017[28]. This fraction (<25% of global sea ice) would likely experience a significant decline due to the warmer surface temperatures in the present study. Even under the largest S emission scenario (325 Gt), the minimum global-average Ts is -3°C post-impact. With a reduced amount of S injected into the atmosphere (70 Gt, proposed value in the present study), the surface environment warms further with the global-average Ts exceeding 2°C (above freezing), therefore decreasing the likelihood of post-impact sea ice formation even more. In a regional context, present surface temperatures indicate lower values in polar regions. However, temperature levels are not below freezing, slightly exceeding 0°C. By including a sea-ice model, the influence of the sea-ice albedo feedback, thus the surface heat exchange, would have been more accurately represented, potentially leading to improved circulation patterns in polar regions. However, given the limited plausibility of sea ice formation and S residence times in our simulations, its effect is expected to be localized and minor.

The latest Cretaceous climatic conditions were included in the PaleoEarth implement, with global-average atmospheric CO_2 concentrations set to 560 parts per million (ppm)[24,28]. Similarly to other paleoclimate studies, a circular orbit with an obliquity of 23.5° and a solar constant of ~1354 W/m^2 were assumed to model orbital forcing[24,28,81]. The Chicxulub impact event is assumed to have occurred in the boreal spring based on recent osteohistological and isotopic studies from uniquely preserved fossil fish from the Tanis K-Pg site[96,97]. The GCM has a horizontal model resolution of 5ºx5º over longitudinal and latitudinal directions and 27 vertical sigma layers extending through the stratopause. Each impact simulation is carried out for a time window of 35 years following an initial 10-year spin-up simulation to stabilize the latest Cretaceous conditions.

Data availability

All numeric data is provided in tabular form in the electronic supplementary material (SI). Bulk S concentrations, $\delta^{34}S$, $\delta^{33}S$, and $\Delta^{33}S$ values are presented in Table S1 and S2 in the SI. Total reduced inorganic S (TRIS) and sulfide specific $\delta^{34}S$ values are presented in Table S3 in the SI. Siderophile element concentrations and median grain-size are presented in Table S4. Source data are provided with this paper. The paleoclimate modeling output data are publicly available in the Open Science Framework (OSF) repository, via https://doi.org/10.17605/OSF.IO/AFGBD. The proxy-based latest Cretaceous temperature data are available in the PANGEA repository, doi.org/10.1594/PANGAEA.879763.

Code availability

The Python and Matlab source codes developed for reproducing figures in the present study are publicly available at the GitHub repository, via github.com/cem-berk-senel/naturecomms-chicxulub/. The PlanetWRF model is available upon request via https://planetwrf.com/.

Materials availability

All powdered selected lithological units of the drill cores within and around the Chicxulub impact structure (PEMEX Y6, UNAM-5, UNAM-6, UNAM-7, ICDP Yax-1, and IODP-ICDP Expedition 364 M0077A) as well as all profiles and bulk samples taken from K-Pg boundary deposition sites (Tanis, Stevns Klint, Caravaca, and Brazos River) measured in this study were collected in previous studies[9,39,43,45,62,69,71,97,98]. Requests for samples should be sent to S.G, J.V, P.K, or P.C.

97. DePalma, R. A. *et al.* Seasonal calibration of the end-cretaceous Chicxulub impact event. *Sci Rep* **11**, 23704 (2021).

98. Belza, J., Goderis, S., Montanari, A., Vanhaecke, F. & Claeys, P. Petrography and geochemistry of distal spherules from the K–Pg boundary in the Umbria–Marche region (Italy) and their origin as fractional condensates and melts in the Chicxulub impact plume. *Geochim Cosmochim Acta* **202**, 231–263 (2017).

99. Rodiouchkina, K., Rodushkin, I., Goderis, S. & Vanhaecke, F. A comprehensive evaluation of sulfur isotopic analysis (δ34S and δ33S) using multi-collector ICP-MS with characterization of reference materials of geological and biological origin. *Anal Chim Acta* **1240**, (2023).

100. Kaskes, P., Déhais, T., de Graaff, S. J., Goderis, S. & Claeys, P. Micro–X-ray fluorescence (μXRF) analysis of proximal impactites: High-resolution element mapping, digital image analysis, and quantifications. *The Geological Society of America Special Paper* **550**, 171–206 (2021).

101. Wouters, S. *et al.* Late orogenic gold mineralization in the western domain of the Karagwe-Ankole Belt (Central Africa): Auriferous quartz veins from the Byumba deposit (Rwanda). *Ore Geol Rev* **125**, (2020).

102. Geng, L. *et al.* Intercomparison measurements of two 33S-enriched sulfur isotope standards. *J Anal At Spectrom* **34**, 1263–1271 (2019).

103. Craddock, P. R., Rouxel, O. J., Ball, L. A. & Bach, W. Sulfur isotope measurement of sulfate and sulfide by high-resolution MC-ICP-MS. *Chem Geol* **253**, 102–113 (2008).

104. Miller, J. N. & Miller, J. C. *Statistics and Chemometrics for Analytical Chemistry*. (Prentice Hall, 2010).

105. Joint Committee For Guides in Metrology (JCGM). *Evaluation of Measurement Data-Guide to the Expression of Uncertainty in Measurement, in Metrology JCGM 100:2008*. (2008).

106. Joint Committee for Guides in Metrology (JCGM). *Guide to the Expression of Uncertainty in Measurement — Part 6: Developing and Using Measurement Models, in Metrology JCGM GUM-6:2020*. (2020).

107. Fossing, H. & Jørgensen, B. B. Measurement of Bacterial Sulfate Reduction in Sediments: Evaluation of a Single-Step Chromium Reduction Method. *Biogeochemistry* **8**, 205–222 (1989).

108. Cline, J. D. Spectrophotometric determination of hydrogen sulfide in natural waters. *Limnol Oceanogr* **14**, 454–458 (1969).

109. Mann, J. L., Vocke, R. D. & Kelly, W. R. Revised δ34S reference values for IAEA sulfur isotope reference materials S-2 and S-3. *Rapid Communications in Mass Spectrometry* **23**, 1116–1124 (2009).

110. Pollard, R. T., Rhines, P. B. & Thompson, R. O. R. Y. The deepening of the wind-Mixed layer. *Geophysical Fluid Dynamics* **4**, 381–404 (1973).

111. Davis, C. *et al.* Prediction of landfalling hurricanes with the advanced hurricane WRF model. *Mon Weather Rev* **136**, 1990–2005 (2008).

112. Nellipudi, N. R., Viswanadhapalli, Y., Challa, V. S., Vissa, N. K. & Langodan, S. Impact of surface roughness parameterizations on tropical cyclone simulations over the Bay of Bengal using WRF-OML model. *Atmos Res* **262**, 105779 (2021).

113. Senel, C. B. *et al.* Relative roles of impact-generated aerosols on photosynthetic activity following the Chicxulub asteroid impact. in *GSA Connects* vol. 16 (Portland, Oregon, USA, 2021).

114. Richardson, M. I., Toigo, A. D. & Newman, C. E. PlanetWRF: A general purpose, local to global numerical model for planetary atmospheric and climate dynamics. *J Geophys Res Planets* **112**, (2007).

115. Skamarock, W. C. *et al. A Description of the Advanced Research WRF Version 3*. (2008).

116. Markwick, P. J. & Valdes, P. J. Palaeo-digital elevation models for use as boundary conditions in coupled ocean–atmosphere GCM experiments: a Maastrichtian (late Cretaceous) example. *Palaeogeogr Palaeoclimatol Palaeoecol* **213**, 37–63 (2004).

117. Chou, M.-D., Suarez, M. J. & Chou, M.-D. *A Solar Radiation Parameterization for Atmospheric Studies*. http://www.sti.nasa.gov/STI-homepage.html (1999).

118. Chou, M.-D., Suarez, M. J., Liang, X.-Z. & Yan, M. M.-H. *A Thermal Infrared Radiation Parameterization for Atmospheric Studies*. vol. 19 http://climate.gsfc.nasa.gov/-chou/clirad_lw. (2001).

119. Feichter, J. *et al.* Simulation of the tropospheric sulfur cycle in a global climate model. *Atmos Environ* **30**, 1693–1707 (1996).

120. Xu, Y. & Carmichael, G. R. American Meteorological Society Modeling the Dry Deposition Velocity of Sulfur Dioxide and Sulfate in Asia. *Journal of Applied Meteorology* **37**, 1084–1099 (1988).

121. Tsarpalis, K. *et al.* The implementation of a mineral dust wet deposition scheme in the GOCART-AFWA module of the WRF model. *Remote Sensing* **10**, 1–23 (2018).

122. Feichter, J., Brost, R. A. & Helmann, M. Three-Dimensional Modeling of the Concentration and Deposition of 21øpb Aerosols. *J Geophys Res* **96**, 447–460 (1991).

123. Dudhia, J. *Preprints, The Sixth PSU/NCAR Mesoscale Model Users' Workshop, 22-24 July*. (1996).

124. Chen, S.-H. & Sun, W.-Y. A One-dimensional Time Dependent Cloud Model. *Journal of the Meteorological Society of Japan* **80**, 99–118 (2002).

125. Tiedtke, M. A comprehensive mass flux scheme for cumulus parameterization in large-scale models. *American Meteorological Society* **117**, 1779–1800 (1989).

126. Zhang, C., Wang, Y. & Hamilton, K. Improved representation of boundary layer clouds over the southeast pacific in ARW-WRF using a modified tiedtke cumulus parameterization scheme. *Mon Weather Rev* **139**, 3489–3513 (2011).

127. Senel, C. B., Temel, O., Porchetta, S., Muñoz-Esparza, D. & van Beeck, J. A new planetary boundary layer scheme based on LES: Application to the XPIA campaign. *J Adv Model Earth Syst* **11**, 2655–2679 (2019).

128. Jiménez, P. A. *et al.* A revised scheme for the WRF surface layer formulation. *Mon Weather Rev* **140**, 898–918 (2012).

129. Francis, J. E. & Poole, I. Cretaceous and early Tertiary climates of Antarctica: evidence from fossil wood. *Palaeogeogr Palaeoclimatol Palaeoecol* **182**, 47–64 (2002).

130. Bowman, V. C., Francis, J. E., Askin, R. A., Riding, J. B. & Swindles, G. T. Latest Cretaceous-earliest Paleogene vegetation and climate change at the high southern latitudes: Palynological evidence from Seymour Island, Antarctic Peninsula. *Palaeogeogr Palaeoclimatol Palaeoecol* **408**, 26–47 (2014).

131. Scasso, R. A. *et al.* A high-resolution record of environmental changes from a Cretaceous-Paleogene section of Seymour Island, Antarctica. *Palaeogeogr Palaeoclimatol Palaeoecol* **555**, 109844 (2020).

132. Reguero, M. A., Tambussi, C. P., Coria, R. A. & Marenssi, S. A. Late Cretaceous dinosaurs from the James Ross Basin, West Antarctica. *Geological Society, London, Special Publications* **381**, 99–116 (2013).

133. Kemp, D. B. *et al.* A cool temperate climate on the Antarctic Peninsula through the latest Cretaceous to early Paleogene. *Geology* **42**, 583–586 (2014).

134. Kriwet, J., Lirio, J. M., Nuñez, H. J., Puceat, E. & Lécuyer, C. Late Cretaceous Antarctic fish diversity. *Geol Soc Spec Publ* **258**, 83–100 (2006).

135. O'Brien, C. L. *et al.* Cretaceous sea-surface temperature evolution: Constraints from TEX86 and planktonic foraminiferal oxygen isotopes. *Earth Sci Rev* **172**, 224–247 (2017).

136. Petersen, S. V., Dutton, A. & Lohmann, K. C. End-Cretaceous extinction in Antarctica linked to both Deccan volcanism and meteorite impact via climate change. *Nat Commun* **7**, (2016).

Acknowledgements

The authors acknowledge the Research Foundation Flanders (FWO) for financial support for this study through the EOS-Excellence of Science program (ET-HoME - ID 30442502). FWO is also acknowledged for providing the funding for the acquisition of MC-ICP-MS instrumentation for the A&MS laboratory (ZW15-02 – G0H6216N). S.G. and P.C. acknowledge support from the VUB Strategic Research Program, FWO, and the Belgian Science Policy Office (BELSPO).C.B.S was supported by grant 12AM624N of the FWO. PK was financially supported by FWO PhD fellowship 11E6621N. Ö.K. was supported by the BELSPO through Chicxulub BRAIN-be (Belgian Research Action through Interdisciplinary Networks) project. O.T. was financially supported by grant 12ZZL23N of FWO. J.V. is funded by the Belgian Science Policy Office (BELSPO) through the FED-tWIN project MicroPAST (Prf-2020-038). We sincerely thank ALS Scandinavia AB for participating in this study, giving K.R. permission to use their facilities and for the invaluable technical support. Robert DePalma is thanked for providing access to the Tanis K-Pg site and assistance in sediment sampling. Additionally, the authors want to express their gratitude towards Aleksei Rodushkin for actualization of the graphical abstract.

Ethics declarations

The authors declare that there are no competing financial interests.

Supplementary Information for

Reduced contribution of sulfur to the mass extinction associated with the Chicxulub impact event

Authors: Katerina Rodiouchkina, Steven Goderis, Cem Berk Senel, Pim Kaskes, Özgür Karatekin, Orkun Temel, Michael Ernst Böttcher, Ilia Rodushkin, Johan Vellekoop, Philippe Claeys, Frank Vanhaecke.

Sulfur concentration and isotopic composition in the target

The highest bulk S concentrations and $\delta^{34}S$ values in the drill cores are observed for the Yax-1 and UNAM-6 cores (20-23 wt% and $\delta^{34}S$ = 18.5 to 19.5 ‰), followed by the UNAM-5 and 7 cores (6-10 wt% and $\delta^{34}S$ = 18.0 to 18.8 ‰), then the Y6 core (0.5-2 wt% and $\delta^{34}S$ = 17.1 to 17.9 ‰), while the lowest are observed for the M0077A core (0.002-4 wt% and $\delta^{34}S$ = -17.2 to 8.5 ‰) (Fig. 1B; Table S1). Pure anhydrite and gypsum have S concentrations of 19 to 24 wt% and their $\delta^{34}S$ values mirror the $\delta^{34}S$ value of the sulfate in the water source from which it originates[1]. All the onshore drill cores located in the southern semicircle composing the Chicxulub impact structure (Yax-1, Y6, UNAM-5-7) have similar $\delta^{34}S$ values that agree well with the previously determined average $\delta^{34}S$ value of 18.3‰ for the Yax-1 and Y6 drill cores (ranging between 18.0 to 19.8‰)[2] and the seawater sulfate $\delta^{34}S$ values ranging between 17 to 19‰ at the end of the Cretaceous[1,3]. The high S concentrations observed for the Yax-1 and UNAM-6 indicate pure anhydrite, while the other represent a mixed composition with high inclusion of evaporites as even the lower S concentrations found in the suevite and impact melt rock sections of the Y6 core show similar $\delta^{34}S$ values (Fig. S2).

The latest offshore M0077A drill core is clearly an outlier when comparing lithology as well as bulk S concentrations and $\delta^{34}S$ values around the K-Pg boundary to those of the previously characterized Yax-1, Y6, and UNAM 5-7 drill cores. In a previous study[4], bulk powder X-ray diffraction (XRD) analysis of the M0077A drill core recorded total percentages of gypsum and anhydrite of 0.73 and 0.04%, respectively. Petrographic examination showed no anhydrite or gypsum minerals present in the

M0077A drill core stratigraphy[4]. In another study[5], the bulk S concentrations determined using micro X-ray fluorescence spectrometry (μXRF) were <7,000 μg g^{-1} throughout the M0077A drill core, except for outliers up to 80,000 μg g^{-1} found in the transitional unit and upper impact melt rock section, which are attributed to the occurrence of pyrite and other sulfides[5]. This is largely consistent with what was observed in the present study, where the highest bulk S concentrations are identified in the bedded suevite and the post-impact units around the K-Pg boundary, but remain <40,000 μg g^{-1}. The bulk $\delta^{34}S$ values determined for these units range from -9 to -5 ‰, and are clearly distinct from the $\delta^{34}S$ values determined for the anhydrite sections in the other onshore drill cores from the southern part of the Chicxulub impact structure (Fig. S2).

The highest bulk $\delta^{34}S$ value in the M0077A drill core profile is observed in the middle part of the graded suevite unit, with an average value of 8.5 ‰ (Fig. 1B; Table S1), indicating the presence of evaporites. Further, this section also shows the largest shift (14.0‰) between the bulk S isotope ratio and the sulfide-specific isotope ratio ($\delta^{34}S_{sulfide}$=-5.5‰) and has a calculated sulfate-specific isotope ratio ($\delta^{34}S_{sulfate}$=14.7‰, assuming that all S in this section is either related to sulfides or sulfates, Table S3) close to the bulk S isotope ratio range found in the evaporite-containing sections located in the five onshore drill cores ($\delta^{34}S$=17.1-19.5‰, Yax-1, Y6, and UNAM-5-7). However, this unit does not coincide with a high S concentration (500 μg g^{-1}), which would be expected if a significant amount of evaporite was mixed in. This S concentration level of the graded suevite unit is approximately 80-fold lower than that of the bedded suevite unit (39,000 μg g^{-1}) and between 10- to 500-fold lower than the S concentrations of the five onshore drill cores (5000-230,000 μg g^{-1}) (Fig.1B; Table S1).

The TRIS fraction throughout the M0077A drill core (22-86%) is higher than the TRIS fraction for the Y6 drill core (≤1 %) (Fig. S5 and Table S3) that shows the lowest bulk S concentration of the onshore drill cores. Still the lower TRIS fraction (29%) coinciding with a higher $\delta^{34}S$ value for the graded suevite unit (Fig. 1B and S5; Table S1 and S3) could be linked to anhydrite and gypsum present

in this section. In general, the units with lower TRIS fractions (<36%) display higher bulk $\delta^{34}S$ values, with values of 0.7-2.2‰ observed for the post-impact and lower LIMB units, while the values with high TRIS fractions (>50%) show a large spread in $\delta^{34}S$ values between -17.2 and 0.3 ‰ (Fig. 1B and S5; Table S1 and S3).

The lowest bulk $\delta^{34}S$ values are found in the Paleogene sediment (-9.1 to -5.0 ‰), bedded suevite (-7.4 to -5.3 ‰), UIM (-15.8 to -0.27 ‰), dolerite (-11.6 to -1.06 ‰), and upper LIMB (-17.2 ‰) units. This is in agreement with the previously published pyrite $\delta^{34}S$ value for the Paleogene sediment (608.48-618.98 mbsf, -32.9 to 0.9 ‰)[6] and for the suevite (618.72-685.47 mbsf, -35.9 to -6.2 ‰)[7] units of the M0077A drill core (Fig. 1B; Table S1). These low $\delta^{34}S$ values observed in the M0077A drill core are suggested by Kring *et al.* 2020[8], 2021[7] to result from late-stage microbial reduction of S in the impact-generated hydrothermal systems, both in the porous, permeable subsurface rock of the crater and in the water column above. In the deepest LIMB (1242-1334 mbsf, 0.32 to 3.0 ‰) unit, the bulk $\delta^{34}S$ values compare well with previously published pyrite $\delta^{34}S$ values for samples at a similar depth in the M0077A drill core (1313.92 mbsf, -3.1 to -1.8 ‰)[7] (Fig. 1B; Table S1). These near-zero $\delta^{34}S$ values found deep within the drill core are similar to the $\delta^{34}S$ value for the upper mantle of -1.40 ± 1.00‰ (2SD) based on mid-ocean-ridge basalts[9–12], indicating that the majority of the S in this unit is likely related to igneous rocks.

In line with previous studies, the S concentrations and $\delta^{34}S$ values determined for the new M0077A drill core also show that it is largely devoid of evaporites in contrast to previous onshore drill cores[4,5]. The reason for this lack of evaporite in the M0077A core is not yet fully understood. It has been suggested that this absence of evaporites can be explained by the non-porous evaporites present in the target rock not vaporizing efficiently and more likely to fragment into larger clasts, transported as low-velocity ejecta and deposited outside of the peak ring[4]. A heterogeneous distribution of evaporites within the sedimentary layers of the pre-impact target rock[13] can also be advocated;

considerable variation in the evaporite proportion could be expected considering the size of the structure. Therefore, it might be interesting to focus future drilling projects on the more northern part of the crater in order to test this hypothesis and better assess the exact amount of evaporite involved in the event.

Traces of possible evaporite content are present in the offshore M0077A drill core as higher $\delta^{34}S$ values and lower TRIS fractions are observed in the graded suevite (Fig. 1B and S5; Table S1 and S3). As the S concentrations are low, the measured signals likely do not exclusively reflect the target bedrock, but are potentially influenced by later post-impact processes, such as microbial S reduction generated by the hydrothermal system active within the Chicxulub peak ring[7]. Therefore, the five onshore drill cores are preferably used to determine the S isotopic 'fingerprint' in the target rock as these have higher S concentrations. Moreover, similar $\delta^{34}S$ values are observed for the unshocked anhydrite (Yax-1, UNAM-5, and UNAM-7) and deposited anhydrite clasts in the K-Pg boundary sediments (UNAM-6) (Table S1). Here, the bulk $\delta^{34}S$ value of the target rock is determined based on the $\delta^{34}S$ values observed for the evaporite-containing lithological units in five different cores drilled in and near the Chicxulub impact structure (Yax-1, Y6, and UNAM-5-7), which yield a mean value of 18.5 ± 1.4‰ (2SD).

K-Pg boundary ejecta deposition sites: Brazos River

The S profiles obtained for the previously studied[14] marine Brazos River site display a positive peak in S concentration coinciding with a positive $\delta^{34}S$ shift (6,000-30,000 μg g^{-1} and -40 ‰ to -33 ‰), possibly also indicating an influx of impact-deposited target anhydrite. The TRIS content in selected samples from the Brazos River K-Pg site profile ranges from 2,600 to 12,000 μg g^{-1}, corresponding to 34-100% of the bulk S concentration (Table S3), with the lowest TRIS fraction coinciding with the most ^{34}S-enriched sample at the K-Pg boundary (Table S2), further indicating that the observed increase in $\delta^{34}S$

is related to evaporate-originating sulfate deposition. However, in contrast to the other sites, the Brazos River S-profiles are jagged (Fig. 2D), indicating heterogenous S input in these K-Pg sediments. This is further demonstrated by large variations in the bulk S concentration and $\delta^{34}S$ value for multiple sub-samples taken from the same location depth (Fig. 2D). A similar jagged behavior is also observed in siderophile element concentrations (Fig. S9) and Ir concentration profiles, at sites across the Gulf of Mexico, indicative of wash-in from impact tsunamis[15,16]. Consequently, this observed heterogeneity likely results from the mixing of S deposition from the atmosphere and the wash-in of low-velocity clasts from within the crater due to the proximity to the impact site. If this site is used for the calculation of impact-released S into the atmosphere, this dual source of S causes an overestimation, which excludes this site from being representative for these types of calculations. This likely accounts for the much higher S estimation obtained by Junium *et al.* 2022[14] (400 Gt S) and the large uncertainty accompanying the estimate obtained in this study for the Brazos River site (337 ± 285 Gt S). However, the good correspondence between the average obtained in present study for this site (337 Gt S) and the value obtained by Junium *et al.* 2022[14] (400 Gt S) confirms the accuracy of the empirical estimation calculations performed in this study.

Mass-independent fractionation

Complementary to S concentrations and $\delta^{34}S$ values, impact-vaporized S depositions can be further traced using mass-independent fractionation (MIF) tracers ($\Delta^{33}S$ and $\Delta^{36}S$), as demonstrated by Junium *et al.* 2022[14]. A number of gas phase reactions can lead to MIF of S isotopes and these can be traced using the $\Delta^{33}S$ and $\Delta^{36}S$ values. Contributions to MIF include, but are not limited to, stabilization of asymmetric isotopologue intermediate species during extensive biomass burning[17] and/or the self-shielding effect of $^{32}SO_2$ compared to other isotopologues during photolysis with UV light due to its higher relative abundance in the gas column[18]. Generally, these MIF signatures are small and poorly preserved in sediments due to redox cycling of S deposited from the atmosphere in an oxidizing

Paleogene atmosphere[19]. Preservation of atmospheric MIF signals in sediments therefore requires a sufficiently large quantity of deposition in a short amount of time to transcend the S isotope ratios of the local sulfate flux to the sediments[14], in line with the hypothesis of massive amounts of impact-vaporized S into the atmosphere.

Similarly to Junium *et al.* 2022[14], negative mass-independent $\Delta^{33}S$ anomalies were observed for the K-Pg boundary section of the Brazos River site (Fig. S4), indicating that a portion of the deposited S had resided in the atmosphere. These negative mass-independent anomalies are also observed to coincide with the positive S concentration peak for the Stevns Klint site, indicating that impact-deposition of S might have occurred at this site, but that its S isotope ratio signature has been overprinted by post-impact processes. For the Caravaca site, this mass anomaly is less pronounced, probably due to the poor peak resolution owing to lower post-impact sedimentation rates (0.2–0.5 cm/k.y) compared to the other two marine sites (1–3 cm/k.y)[20], but the $\Delta^{33}S$ values at the K-Pg boundary are slightly lower than those measured in the Paleocene sediments. However, many of these observations are provisional as they are based on $\Delta^{33}S$ values that are = 0 ‰ within the expanded uncertainty of the method. The only samples for which the $\Delta^{33}S$ values are ≠ 0 ‰ taken into account the expanded uncertainty coincide with the S offset peaks in the Brazos River (-0.17 ± 0.14 ‰, -0.20 ± 0.15 ‰, -0.27 ± 0.11 ‰, -0.17 ± 0.09 ‰) and Stevns Klint (-0.13 ± 0.12 ‰, -0.15 ± 0.10 ‰) K-Pg boundary profiles, as well as for the Elles (-0.25 ± 0.23 ‰) K-Pg boundary clay sample (Table S2), supporting the hypothesis that a portion of the S in these K-Pg sediments originated from atmospheric S. However, this does not rule out influence of other post-impact processes in the K-Pg sediment of these sites.

Ir anomaly and other siderophile element concentrations

A more conventional way of assessing airfall following an impact is through studying concentrations of the siderophile elements, such as the platinum group elements (PGE: ruthenium, rhodium, palladium,

osmium, iridium, and platinum), Cr, Co, Ni, Re and Au and ratios between these element concentrations in impact-related sediment profiles. The presence of a meteoritic contribution is strongly indicated if Ir and the other siderophile element concentrations are highly elevated compared to background (i.e., continental crustal) values and the ratios between these elements are roughly similar to chondritic ratios in impact-related lithologies (melt rocks, impact ejecta material, etc.)[21]. Highly elevated Ir concentrations, *i.e.* the so-called Ir anomaly, have previously been observed for Brazos River [21–26], Caravaca[21,27], Stevns Klint[21,28], Dogie Creek[21], and Brownie Butte[21]. Iridium concentration data for the Knudsen Coulee or Knudsen Farm sites are not reported in literature.

A full elemental screening of 70 elements, including Ir, Re, Co, Cr, Ni, and S, was performed for the K-Pg boundary sediment profile for the Tanis site. Ir and Re concentrations (Fig. S6 and Table S4) were very close to the detection limit (DL) of the method and should therefore only be used as information values, but a consistent increase in both concentrations is observed around the post-impact claystone sediment and coincides with the increase in S concentration. Co, Cr, and Ni concentrations (Fig. S6 and Table S4) are well above the method DL and all show a similar increase in concentration as S in the post-impact claystone sediment. The Ni/Cr ratios (Fig. S6 and Table S4) around the S increase for the Tanis site are between 1.6 and 3.4, which is distinct from the Ni/Cr values of the Earth crust around ~0.5[21,29]. This range indicates meteoritic input as these values are more similar to the Ni/Cr values of 1.1-3.4 previously observed in smectites from a K-Pg boundary site at Beloc, Haiti[30]; the slope of 4.3±1.3 (Ni/Cr range between 0.09-7.42) for the regression line of Ni and Cr values for 48 different K-Pg boundary ejecta layers from all around the globe[21]; and the mean Ni/Cr for carbonaceous chondrites of CO-type (3.96±0.09), CM-type (4.01±0.30), CR-type (3.72±0.39)[31]; which have been suggested to match the Chicxulub impactor[32]. The previously published median grain-sizes for the Tanis K-Pg sediment profile[33] is lacking data in the Paleocene coal interval coinciding with the positive S anomaly, but the median grain size right below (in the claystone interval, right above the K-Pg boundary

line in Fig. S6) is significantly finer (2.88-3.83 μm) and unimodal compared to the event deposit siltstone right below (10.63-11.27 μm) and the Paleocene siltstone above (12.75-29.86 μm), indicating airborne deposition. Combining the Ir and Re information data with the Co, Cr, and Ni concentrations, Ni/Cr ratios, and grain-size data, the increase in S concentrations observed at the Tanis site is highly likely due to airfall following the impact.

A partial elemental screening of 20 elements was performed for Brazos River, Caravaca, and Stevns Klint, including concentrations for Co, Cr, Ni, and S, but not for Ir or Re. For both Stevns Klint and Caravaca an increase in Co, Cr, and Ni concentrations and a Ni/Cr ratio between 1.3–5.1 are observed following the impact, which coincides with increases in the S concentration (Fig. S7 and S8, Table S4). A portion of the S at these sites likely derives from airborn S related to the impact, supported by previously published Ir data, the Co, Cr, Ni, and Ni/Cr data, and negative mass-independent S anomalies that are observed at these sites (discussed in the previous section "Mass-independent fractionation"). However, the Co, Cr, and Ni profiles for the Brazos River site are scattered and a clear peak coinciding with the increase in S concentration is difficult to distinguish (Fig. S9 and Table S4), possibly due to tsunami/seiche waves. The Ni/Cr values are 0.2–0.7 throughout the entire profile (Fig. S9 and Table S4), which are more consistent with Earth crust values and indicate strong dilution of the meteoritic component.

Table S1. Bulk S concentration and isotopic composition in different drill cores of the Chicxulub impact structure. Expanded uncertainties (U) are presented for the bulk isotopic compositions and n represents the number of separate sample preparations.

Location	Core	Sample ID	Depth mbsf	Lithological unit	Bulk S µg g^{-1}	SD µg g^{-1}	$\delta^{34}S$	U	$\delta^{33}S$	U	$\Delta^{33}S$	U	n
Mexico	IODP-ICDP Expedition 364	39_3_11_12	615.88	Paleogene sediments	550	20	6.08	0.23	3.10	0.40	-0.03	0.39	1
		40_1_30_36	616.53	Paleogene sediments	12000	500	-9.14	0.36					1
		40_1_38_44	616.63	Paleogene sediments	10500	500	-5.02	0.26					1
		40_1_38_44	616.67	Transitional unit	1200	100	2.85	5.22	2.80	0.39	-0.01	0.38	2
		40_1_49_50	616.73	Transitional unit	1430	60	2.17	0.21	1.14	0.39	0.03	0.37	1
		40_1_80_82	617.04	Transitional unit	1130	40	3.02	0.24	1.59	0.40	0.04	0.37	1
		40_1_106_110	617.33	Transitional unit	11900	100	-5.88	0.28	-2.84	0.60	0.18	0.55	1
		40_1_111_113	617.35	Bedded suevite unit	39000	1800	-5.30	0.30	-2.69	0.43	0.03	0.39	1
		40_2_100_103	618.67	Bedded suevite unit	8240	80	-7.35	0.24	-3.69	0.39	0.10	0.37	1
		55_3_8_14	664.49	Graded suevite unit	460	20	8.50	0.22	4.32	0.39	-0.06	0.37	1
		68_1_67_70	692.13	Graded suevite unit	490	20	6.32	0.22	3.24	0.40	-0.01	0.38	1
		81_3_30_32	710.29	Non-graded suevite unit	610	30	-0.32	0.25	-0.21	0.38	-0.04	0.37	1
		90_2_48_50b	730.29	Granitoid clast inside UIM (Unit 3A)	1320	60	-15.77	0.22	-8.16	0.39	-0.05	0.38	1
		91_3_18_20	734.25	Upper impact melt rock unit (UIM, Unit 3A)	700	30	-0.27	0.24	-0.14	0.39	-0.01	0.37	1
		139_1_6_8	853	Dolerite	1830	80	-11.60	0.18	-5.96	0.23	0.01	0.28	1
		162_2_99.5_101.5	914.63	Dolerite	1660	70	-1.06	0.17	-0.68	0.31	-0.12	0.33	1
		164_3_14_16.5	920.36	Dacite	91	2	-0.50	0.35	-0.30	0.36	-0.07	0.28	2
		192_1_56_58	997.65	Lower impact melt-bearing unit (LIMB)	430	20	-17.21	0.21	-8.79	0.39	0.07	0.37	1
		264_1_53_55	1212.67	Granitoid	16	6	6.12	0.22	3.01	0.39	-0.14	0.38	1
		273_2_78_80	1242	LIMB	620	30	1.47	0.22	0.74	0.39	-0.01	0.38	1
		276_3_93_95	1252.33	Metamorphic clast (gneiss/amphibolite)	810	30	2.10	0.28	1.13	0.48	0.05	0.45	1
		282_1_80_82	1268.74	LIMB	120	10	2.98	0.30	1.72	0.43	0.20	0.45	2
		283_2_46_48	1272.97	LIMB	490	20	0.32	0.16	0.12	0.32	-0.05	0.36	1
		303_3_17.5_19.5	1334.33	LIMB	1450	60	0.66	0.21	0.41	0.52	0.07	0.51	1
Mexico	Yucatán-6	Y6_N14_P15	1208-1211	Suevite	5000	200	17.06	0.38	8.59	0.40	-0.11	0.23	3
	Yucatán-6	Y6_N17	1295.95-1299	Impact melt rock	22600	300	17.93	0.31	9.14	0.26	-0.10	0.20	3
Mexico	UNAM 5	500.55-500.65	500.55	Evaporite (anhydrite)	57700	2500	17.96	0.38					3
Mexico	UNAM 6	107_385.85-385.95	385.85	Evaporite clast	199200	8800	19.48	0.32					4
Mexico	UNAM-7	135_381.40-381.50	381.4	Evaporite (anhydrite)	102700	4500	18.80	0.31					4
	UNAM-7	97_267.40-267.50	267.4	Evaporite (anhydrite)	81700	3600	18.58	0.40					4
Mexico	Yaxcopoil-1	1576a	1080.35	Cretaceous megablock	229000	16000	19.01	0.30	9.78	0.24	-0.05	0.18	9
	Yaxcopoil-1	1568a	1057.99	Cretaceous megablock	229000	13000	18.47	0.22	9.43	0.27	-0.10	0.23	6
	Yaxcopoil-1	1606a	1165.24	Cretaceous megablock	200500	8900	19.24	0.47	9.75	0.24	-0.02	0.23	8

Table S2. Bulk S concentration and isotopic composition in different K-Pg boundary deposition sites. Expanded uncertainties (U) are presented for the bulk isotopic compositions and n represents the number of separate sample preparations.

Location	Section/Core	Sample ID	Depth cm	Lithological unit	Bulk S µg g^{-1}	SD µg g^{-1}	$\delta^{34}S$	U	$\delta^{33}S$	U	$\Delta^{33}S$	U	n
Denmark	Stevns Klint A	SK KSA 50	27.5	K-Pg section	360	30	20.88	0.18	10.74	0.09	-0.01	0.09	1
	Stevns Klint A	SK KSA 40	19.5	K-Pg section	410	40	17.40	0.18	8.92	0.20	-0.04	0.17	1
	Stevns Klint A	SK KSA 43	16.5	K-Pg section	310	30	15.98	0.18	8.21	0.20	-0.02	0.22	1
	Stevns Klint A	SK KSA 45	14.5	K-Pg section	770	70	-19.73	0.17	-10.14	0.24	0.02	0.23	1
	Stevns Klint A	SK KSA 47	12.5	K-Pg section	8700	1400	-39.38	0.37	-20.41	0.12	-0.13	0.12	2
	Stevns Klint A	SK KSA 20	9.5	K-Pg section	9000	100	-37.54	0.16	-19.50	0.16	-0.16	0.17	1
	Stevns Klint A	SK KSA 23	7.5	K-Pg section	10500	1800	-36.37	0.37	-18.89	0.08	-0.15	0.10	2
	Stevns Klint A	SK KSA 2	0.75	K-Pg section	360	30	-8.52	0.21	-4.27	0.23	0.12	0.19	1
	Stevns Klint A	SK KSA 1b	0.75	K-Pg section	590	50	-7.20	0.16	-3.56	0.30	0.15	0.30	1
	Stevns Klint A	SK KSA 1	0.015	K-Pg section	4300	410	-12.23	0.18	-6.25	0.17	0.05	0.16	1
	Stevns Klint A	SK KSB 98	-4.5	K-Pg section	220	10	18.81	0.18	9.61	0.10	-0.08	0.12	2
Spain	Caravaca	SM75 510	22	K-Pg section	210	10	19.07	0.14	9.80	0.20	0.03	0.19	1
	Caravaca	SM75 507	7	K-Pg section	410	20	-13.77	0.15	-7.09	0.17	0.00	0.14	1
	Caravaca	504	1	K-Pg section	550	20	-17.85	0.12	-9.17	0.12	0.02	0.11	1
	Caravaca	503C	0.25	K-Pg section	640	30	-13.63	0.14	-6.97	0.17	0.05	0.14	1
	Caravaca	503B	0	K-Pg section	780	30	-32.29	0.19	-16.63	0.15	0.00	0.11	1
	Caravaca	501A	-1	K-Pg section	260	10	18.73	0.12	9.60	0.14	-0.04	0.16	2
	Caravaca	SM75 515	-24	K-Pg section	370	20	-8.99	0.17	-4.74	0.18	-0.11	0.16	2
	Caravaca	SM75 517	-44	K-Pg section	580	10	-18.68	0.17	-9.69	0.24	-0.07	0.20	1
Texas, USA	Brazos River	JV-BR 18	100	K-Pg section	4600	100	-39.56	0.38					1
	Brazos River	JV-BR 41	75	K-Pg section	2900	100	-39.87	0.21	-20.63	0.14	-0.10	0.17	1
	Brazos River	JV-BR 16	65	K-Pg section	5100	100	-40.26	0.43					1
	Brazos River	JV-BR 14	50	K-Pg section	6700	200	-40.32	0.43					1
	Brazos River	JV-BR 28	45	K-Pg section	10100	200	-40.79	0.20	-21.19	0.25	-0.20	0.26	1
	Brazos River	JV-BR 9	40	K-Pg section	9000	200	-40.35	0.36					1
	Brazos River	JV-BR 38	28	K-Pg section	5800	100	-37.17	0.28					1
	Brazos River	JV-BR 49	18	K-Pg section	4400	100	-37.16	0.20					1
	Brazos River	JV-BR 19	15	K-Pg section	8800	200	-36.52	0.23	-18.98	0.17	-0.17	0.14	1
	Brazos River	JV-BR 68	13.4	K-Pg section	8600	50	-37.34	0.20	-19.44	0.15	-0.20	0.15	1
	Brazos River	JV-BR 60	10.9	K-Pg section	4300	100	-35.72	0.22					1
	Brazos River	JV-BR 30	5.5	K-Pg section	6000	100	-37.61	0.24	-19.64	0.12	-0.27	0.11	1
	Brazos River	JV-BR 50	2.5	K-Pg section	1610	40	-32.60	0.29					2
	Brazos River	JV-BR 51	1.5	K-Pg section	1560	40	-32.01	0.31					2
	Brazos River	JV-BR 66	0	K-Pg section	3580	80	-34.27	0.21					1
	Brazos River	JV-BR 36	-15	K-Pg section	27500	2200	-32.96	5.75	-19.51	0.25	-0.23	0.24	4
	Brazos River	JV-BR 29	-20	K-Pg section	3460	80	-35.20	0.40					2
	Brazos River	JV-BR 35	-26	K-Pg section	12900	300	-38.83	0.21	-20.09	0.09	-0.09	0.10	1
	Brazos River	JV-BR 22	-32	K-Pg section	8900	200	-38.47	0.49					1
	Brazos River	JV-BR 33	-40	K-Pg section	9800	200	-36.79	0.27	-19.06	0.14	-0.12	0.16	1
	Brazos River	JV-BR 20	-52.5	K-Pg section	14800	300	-39.18	0.24	-20.26	0.14	-0.08	0.11	1
	Brazos River	JV-BR 6	-125	K-Pg section	11000	200	-39.04	0.21	-20.27	0.10	-0.17	0.09	1
	Brazos River	JV-BR 7	-225	K-Pg section	12300	200	-36.68	0.16	-18.95	0.15	-0.08	0.15	1
N-Dakota, USA	Tanis	X-2761_1_0-1cm	12.5	Paleocene siltstone	1200	100	-0.80	0.18					1
	Tanis	X-2761_2_1-2cm	11.5	Paleocene siltstone	1800	100	-0.26	0.18					1
	Tanis	X-2761_3_2-3cm	10.5	Paleocene siltstone	2010	20	1.65	0.18					1
	Tanis	X-2761_4_3-4cm	9.5	Paleocene coal	7800	1100	4.36	0.20					2
	Tanis	X-2761_5_4-5cm	8.5	Paleocene coal	6500	1100	4.43	0.54					2
	Tanis	X-2761_6_5-6cm	7.5	Paleocene coal	7400	800	4.68	0.24					1
	Tanis	X-2761_7_6-7.25cm	6.375	Paleocene coal	6170	10	0.53	0.20					1
	Tanis	X-2761_8A_7.25-8cm	5.375	K-Pg tonstein	1720	10	-2.33	0.18					1
	Tanis	X-2761_8B_8-8.5cm	4.75	K-Pg tonstein	2570	10	-1.99	0.18					1
	Tanis	X-2761_8C_8.5-9cm	4.25	K-Pg tonstein	3300	100	-1.90	0.18					1
	Tanis	X-2761_9_9-10cm	3.5	Event deposit	600	10	-5.12	0.19					1
	Tanis	X-2761_10_10-11cm	2.5	Event deposit	640	20	-5.78	0.20					1
Haiti	Beloc	Goderis et al. (2013)[21]		K-Pg boundary clay	140	10	17.36	0.27	8.87	0.27	-0.07	0.24	1
Texas, USA	Brazos River	Goderis et al. (2013)[21]		K-Pg boundary clay	12000	100	-31.81	0.30	-16.52	0.20	-0.14	0.21	1
Colorado, USA	Long Canyon, Raton Basin	Goderis et al. (2013)[21]		K-Pg boundary clay	1460	10	4.01	0.29	2.06	0.17	-0.01	0.18	1
Wyoming, USA	Dogie Creek, Powder River Basin	Goderis et al. (2013)[21]		K-Pg boundary clay	3250	40	-0.89	0.30	-0.52	0.29	-0.06	0.23	2
Montana, USA	Brownie Butte, Hell Creek area	Goderis et al. (2013)[21]		K-Pg boundary clay	4170	40	-3.20	0.28	-1.71	0.18	-0.06	0.15	1
Montana, USA	Seven Blackfoot Creek, Hell Creek area	Goderis et al. (2013)[21]		K-Pg boundary clay	510	20	-1.98	0.22	-0.98	0.31	0.04	0.30	2
Italy	Frontale, Umbria-Marche	Goderis et al. (2013)[21]		K-Pg boundary clay	90	20	16.23	0.31	8.35	0.27	0.00	0.18	1
Italy	Fonte D'Olio, Umbria-Marche	Goderis et al. (2013)[21]		K-Pg boundary clay	170	20	15.81	0.26	8.22	0.37	0.08	0.38	1
Tunisia	Siliana	Goderis et al. (2013)[21]		K-Pg boundary clay	3580	40	12.72	0.30	6.29	0.26	-0.14	0.25	1
Tunisia	Elles	Goderis et al. (2013)[21]		K-Pg boundary clay	63200	600	18.00	0.26	9.02	0.26	-0.25	0.23	1

Table S3. Total reduced inorganic S (TRIS), TRIS-fraction (TRIS/bulk S concentration*100), sulfide-specific isotope ratio ($\delta^{34}S_{sulfide}$), isotope ratio difference between bulk and sulfide-specific sulfur isotope ratio ($\delta^{34}S_{bulk}$-$\delta^{34}S_{sulfide}$), and calculated sulfate-specific isotope ratio ($\delta^{34}S_{sulfate}$)[#] in different K-Pg boundary drill cores of the Chicxulub impact-structure and the Brazos River K-Pg boundary section.

Location	Section/Core	Sample ID	Depth cm	Lithological unit	TRIS µg g^{-1}	TRIS-fraction %	$\delta^{34}S_{sulfide}$ ‰	($\delta^{34}S_{bulk}$-$\delta^{34}S_{sulfide}$) ‰	$\delta^{34}S_{sulfate}$[#] ‰
Texas, USA	Brazos River	JV-BR 28	45	K-Pg section	4030	40	-42.00	1.2	-40.0
	Brazos River	JV-BR 19	15	K-Pg section	5060	57	-38.60	2.1	-33.7
	Brazos River	JV-BR 68	13.4	K-Pg section	8760	102	-38.80	1.5	-
	Brazos River	JV-BR 30	5.5	K-Pg section	2630	44	-35.60	-2.0	-39.2
	Brazos River	JV-BR 36	-15	K-Pg section	9430	34	-33.90	3.6	-28.3
	Brazos River	JV-BR 35	-26	K-Pg section	5680	44	-39.76	0.9	-38.1
	Brazos River	JV-BR 33	-40	K-Pg section	5180	53	-37.90	1.1	-35.5
	Brazos River	JV-BR 20	-52.5	K-Pg section	12450	84	-39.73	0.5	-36.4
	Brazos River	JV-BR 6	-125	K-Pg section	5380	49	-40.78	1.7	-37.4
	Brazos River	JV-BR 7	-225	K-Pg section	5270	43	-37.67	1.0	-35.9
			mbsf						
Mexico	IODP-ICDP Expedition 364	40_1_49_50	616.73	Transitional unit	510	36	-7.80	9.9	7.7
		40_2_100_103	618.67	Bedded suevite unit	6980	85	-9.20	1.9	2.9
		55_3_8_14	664.49	Graded suevite unit	140	29	-5.50	14.0	14.7
		68_1_67_70	692.13	Graded suevite unit	160	33	¤		
		90_2_48_50b	730.29	Granitoid clast inside UIM (Unit 3A)	780	59	-16.30	0.6	-15.0
		91_3_18_20	734.25	UIM (Unit 3A)	350	49	-2.30	2.1	1.8
		139_1_6_8	853	Dolerite	1100	61	-12.50	0.9	-10.3
		162_2_99.5_101.5	914.63	Dolerite	830	50	-1.60	0.5	-0.5
		192_1_56_58	997.65	LIMB	370	86	-20.10	2.9	-0.1
		273_2_78_80	1242	LIMB	180	29	-0.30	1.7	2.2
		276_3_93_95	1252.33	Metamorphic clast (gneiss/amphibolite)	170	22	0.70	1.4	2.5
		283_2_46_48	1272.97	LIMB	260	52	¤		
		303_3_17.5_19.5	1334.33	LIMB	360	25	¤		
Mexico	Yucatán-6	Y6_N14_P15	1208-1211	Suevite	52	1	¤		
	Yucatán-6	Y6_N17	1295.95-1299	Impact melt rock	24	0.1	¤		

[#] Sulfate specific isotope ratio was calculated using a simplified isotope dilution equation [$\delta^{34}S_{sulfate}$= $\delta^{34}S_{bulk}$-TRIS*($\delta^{34}S_{sulfide}$-$\delta^{34}S_{bulk}$)/(bulk S concentration-TRIS)] assuming that all the S that is not found in the reduced inorganic S phase in the samples is related to sulfates.

¤ Insufficient amount of material for reliable measurements.

Table S4. Bulk S, Co, Cr, and Ni concentrations; raw and background subtracted (BS) Ni/Cr ratios; and Ir and Re information values in different K-Pg boundary deposition sites. Error bars represent the standard deviation between two or more replicates.

Location	Section/Core	Sample ID	Depth cm	Lithological unit	Co µg g^{-1}	SD µg g^{-1}	Cr µg g^{-1}	SD µg g^{-1}	Ni µg g^{-1}	SD µg g^{-1}	Ni/Cr Raw	Ni/Cr BS	Ir ng g^{-1}	Re ng g^{-1}
Denmark	Stevns Klint A	SK KSA 50	27.5	K-Pg section	**4**	0	**38**	1	**42**	2	1.1	**1.1**		
	Stevns Klint A	SK KSA 40	19.5	K-Pg section	**6**	0	**74**	1	**58**	2	0.8	**0.7**		
	Stevns Klint A	SK KSA 43	16.5	K-Pg section	**26**	2	**50**	1	**88**	4	1.8	**1.8**		
	Stevns Klint A	SK KSA 45	14.5	K-Pg section	**22**	2	**56**	1	**95**	4	1.7	**1.7**		
	Stevns Klint A	SK KSA 47	12.5	K-Pg section	**34**	4	**74**	3	**325**	15	4.9	**5.0**		
	Stevns Klint A	SK KSA 20	9.5	K-Pg section	**21**	2	**85**	1	**310**	18	3.8	**3.8**		
	Stevns Klint A	SK KSA 23	7.5	K-Pg section	**32**	2	**92**	2	**464**	18	4.9	**5.0**		
	Stevns Klint A	SK KSA 2	0.75	K-Pg section	**33**	2	**202**	4	**457**	20	2.5	**2.5**		
	Stevns Klint A	SK KSA 1b	0.75	K-Pg section	**20**	1	**126**	1	**254**	11	2.1	**2.1**		
	Stevns Klint A	SK KSA 1	0.015	K-Pg section	**174**	13	**197**	3	**2288**	99	11.5	**11.6**		
	Stevns Klint A	SK KSB 98	-4.5	K-Pg section	**0**	0	**2**	0	**3**	0	1.3			
Spain	Caravaca	SM75 510	22	K-Pg section	**4**	0	**47**	2	**26**	2	0.6	**0.8**		
	Caravaca	SM75 507	7	K-Pg section	**28**	2	**159**	7	**184**	14	1.2	**1.4**		
	Caravaca	504	1	K-Pg section	**37**	3	**138**	6	**160**	12	1.1	**1.4**		
	Caravaca	503C	0.25	K-Pg section	**51**	4	**229**	10	**270**	21	1.2	**1.3**		
	Caravaca	503B	0	K-Pg section	**351**	26	**429**	19	**2065**	160	4.7	**5.1**		
	Caravaca	501A	-1	K-Pg section	**4**	0	**35**	4	**24**	3	0.7	**0.0**		
	Caravaca	SM75 515	-24	K-Pg section	**5**	0	**47**	1	**25**	1	0.6	**0.6**		
	Caravaca	SM75 517	-44	K-Pg section	**5**	4	**45**	0	**23**	2	0.5	**-0.2**		
Texas, USA	Brazos River	JV-BR 18	100	K-Pg section	**7**	1	**90**	5	**31**	2	0.3	**0.3**		
	Brazos River	JV-BR 41	75	K-Pg section	**11**	1	**110**	6	**44**	2	0.4	**0.4**		
	Brazos River	JV-BR 16	65	K-Pg section	**9**	1	**109**	6	**40**	2	0.4	**0.4**		
	Brazos River	JV-BR 14	50	K-Pg section	**9**	1	**102**	6	**37**	2	0.4	**0.3**		
	Brazos River	JV-BR 28	45	K-Pg section	**12**	0	**113**	6	**55**	3	0.5	**0.5**		
	Brazos River	JV-BR 9	40	K-Pg section	**8**	1	**95**	5	**34**	2	0.4	**0.3**		
	Brazos River	JV-BR 38	28	K-Pg section	**8**	1	**80**	5	**33**	2	0.4	**0.4**		
	Brazos River	JV-BR 49	18	K-Pg section	**10**	1	**98**	6	**36**	2	0.4	**0.3**		
	Brazos River	JV-BR 19	15	K-Pg section	**11**	1	**82**	2	**44**	2	0.5	**0.5**		
	Brazos River	JV-BR 68	13.4	K-Pg section	**0**	0	**85**	5	**50**	3	0.6	**0.7**		
	Brazos River	JV-BR 60	10.9	K-Pg section	**7**	1	**78**	4	**25**	1	0.3	**0.3**		
	Brazos River	JV-BR 30	5.5	K-Pg section	**8**	1	**66**	4	**30**	2	0.5	**0.5**		
	Brazos River	JV-BR 50	2.5	K-Pg section	**3**	0	**22**	1	**8**	0	0.4	**0.2**		
	Brazos River	JV-BR 51	1.5	K-Pg section	**3**	0	**25**	1	**9**	0	0.3	**0.2**		
	Brazos River	JV-BR 66	0	K-Pg section	**5**	0	**46**	3	**14**	1	0.3	**0.2**		
	Brazos River	JV-BR 36	-15	K-Pg section	**14**	2	**75**	12	**37**	11	0.5	**0.5**		
	Brazos River	JV-BR 29	-20	K-Pg section	**3**	0	**15**	1	**7**	0	0.5			
	Brazos River	JV-BR 35	-26	K-Pg section	**11**	1	**114**	7	**46**	2	0.4	**0.4**		
	Brazos River	JV-BR 22	-32	K-Pg section	**7**	1	**130**	7	**31**	2	0.2	**0.2**		
	Brazos River	JV-BR 33	-40	K-Pg section	**11**	1	**142**	5	**49**	3	0.4	**0.3**		
	Brazos River	JV-BR 20	-52.5	K-Pg section	**11**	1	**114**	7	**38**	2	0.3	**0.3**		
	Brazos River	JV-BR 6	-125	K-Pg section	**9**	1	**128**	3	**41**	2	0.3	**0.3**		
	Brazos River	JV-BR 7	-225	K-Pg section	**11**	1	**156**	9	**54**	3	0.4	**0.4**		
N-Dakota, USA	Tanis	X-2761_1_0-1cm	12.5	Paleocene siltstone	**3**	0	**23**	2	**14**	1	0.6		**3**	**1.0**
	Tanis	X-2761_2_1-2cm	11.5	Paleocene siltstone	**3**	0	**31**	4	**15**	1	0.5	**0.1**	**3**	**0.4**
	Tanis	X-2761_3_2-3cm	10.5	Paleocene siltstone	**5**	0	**37**	6	**26**	1	0.7	**0.9**	**1**	**0.7**
	Tanis	X-2761_4_3-4cm	9.5	Paleocene coal	**19**	0	**77**	2	**199**	1	2.6	**3.4**	**12**	**3.3**
	Tanis	X-2761_5_4-5cm	8.5	Paleocene coal	**22**	2	**65**	2	**146**	3	2.2	**3.1**	**6**	**0.6**
	Tanis	X-2761_6_5-6cm	7.5	Paleocene coal	**23**	1	**96**	6	**148**	7	1.5	**1.8**	**8**	**1.3**
	Tanis	X-2761_7_6-7.25cm	6.375	Paleocene coal	**18**	0	**70**	3	**91**	0	1.3	**1.6**	**22**	**6.0**
	Tanis	X-2761_8A_7.25-8cm	5.375	K-Pg tonstein	**22**	1	**25**	2	**20**	3	0.8	**2.7**	**5**	**0.5**
	Tanis	X-2761_8B_8-8.5cm	4.75	K-Pg tonstein	**4**	0	**19**	2	**12**	2	0.6	**0.6**	**2**	**0.0**
	Tanis	X-2761_8C_8.5-9cm	4.25	K-Pg tonstein	**3**	0	**25**	2	**16**	2	0.6	**0.7**	**4**	**0.4**
	Tanis	X-2761_9_9-10cm	3.5	Event deposit	**10**	0	**41**	4	**33**	1	0.8	**1.1**	**5**	**0.8**
	Tanis	X-2761_10_10-11cm	2.5	Event deposit	**10**	1	**36**	3	**34**	2	0.9	**1.5**	**4**	**0.3**
Haiti	Beloc	Goderis et al. (2013)[21]		K-Pg boundary clay	**15**	0	**51**	2	**55**	0	1.2			
Texas, USA	Brazos River	Goderis et al. (2013)[21]		K-Pg boundary clay	**9**	0	**69**	5	**34**	2	0.5			
Colorado, USA	Long Canyon, Raton Basin	Goderis et al. (2013)[21]		K-Pg boundary clay	**1**	0	**19**	1	**2**	0	0.1			
Wyoming, USA	Dogie Creek, Powder River Basin	Goderis et al. (2013)[21]		K-Pg boundary clay	**1**	0	**59**	6	**6**	1	0.1			
Montana, USA	Brownie Butte, Hell Creek area	Goderis et al. (2013)[21]		K-Pg boundary clay	**6**	0	**53**	4	**21**	1	0.4			
Montana, USA	Seven Blackfoot Creek, Hell Creek area	Goderis et al. (2013)[21]		K-Pg boundary clay	**7**	0	**21**	1	**19**	1	1.0			
Italy	Frontale, Umbria-Marche	Goderis et al. (2013)[21]		K-Pg boundary clay	**57**	1	**113**	8	**205**	10	1.9			
Italy	Fonte D'Olio, Umbria-Marche	Goderis et al. (2013)[21]		K-Pg boundary clay	**39**	1	**108**	6	**169**	1	1.7			
Tunisia	Siliana	Goderis et al. (2013)[21]		K-Pg boundary clay	**22**	0	**187**	13	**127**	6	0.7			
Tunisia	Elles	Goderis et al. (2013)[21]		K-Pg boundary clay			**93**	7	**154**	7	1.6			

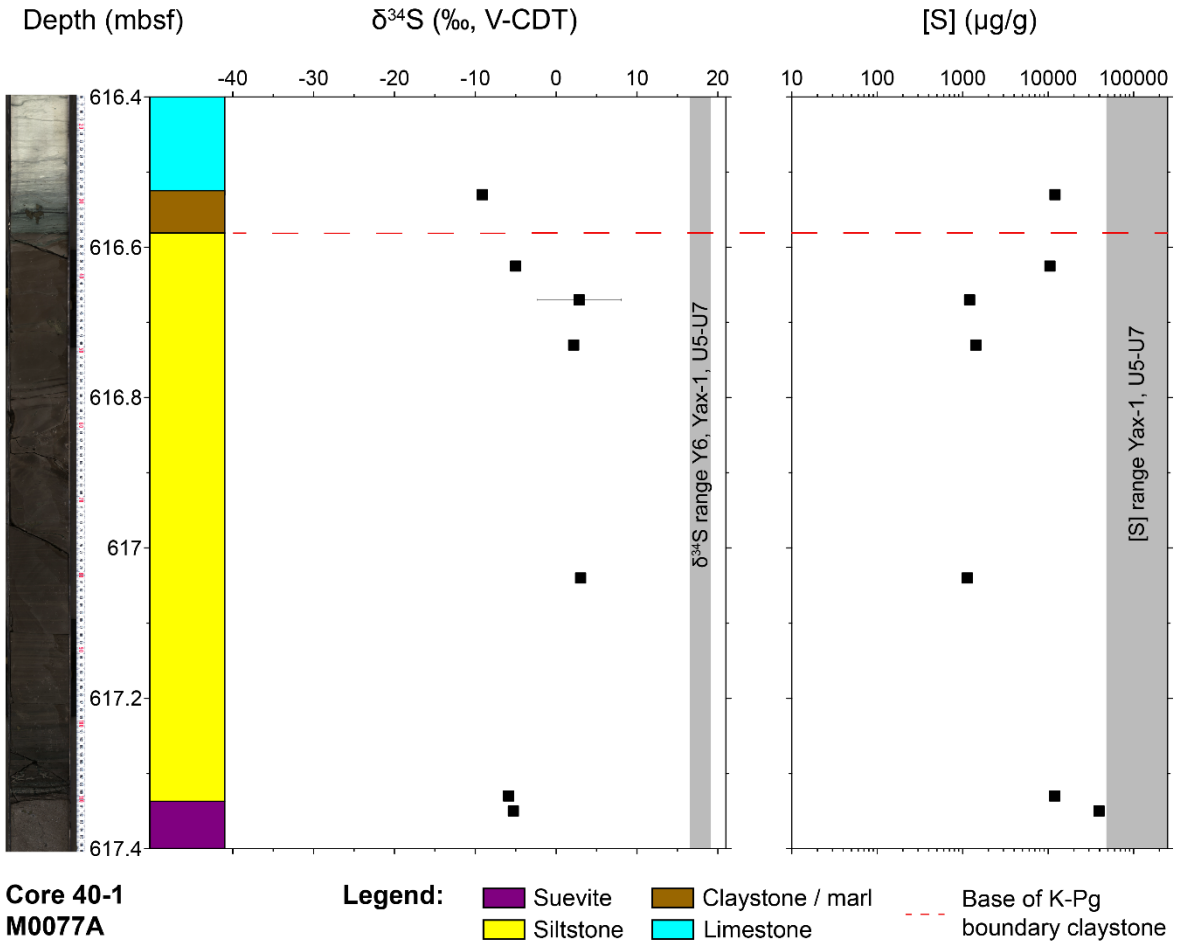

Fig. S1. Detailed bulk $\delta^{34}S$ values and S concentrations of the K-Pg boundary claystone interval of the top part of the impactite sequence of the IODP-ICDP Expedition 364 M0077A drill core, focusing on drill core section 40R1 between 616.4 and 617.4 meters below sea floor (mbsf). Full profiles of the M0077A drill core can be found in Fig. 1B.

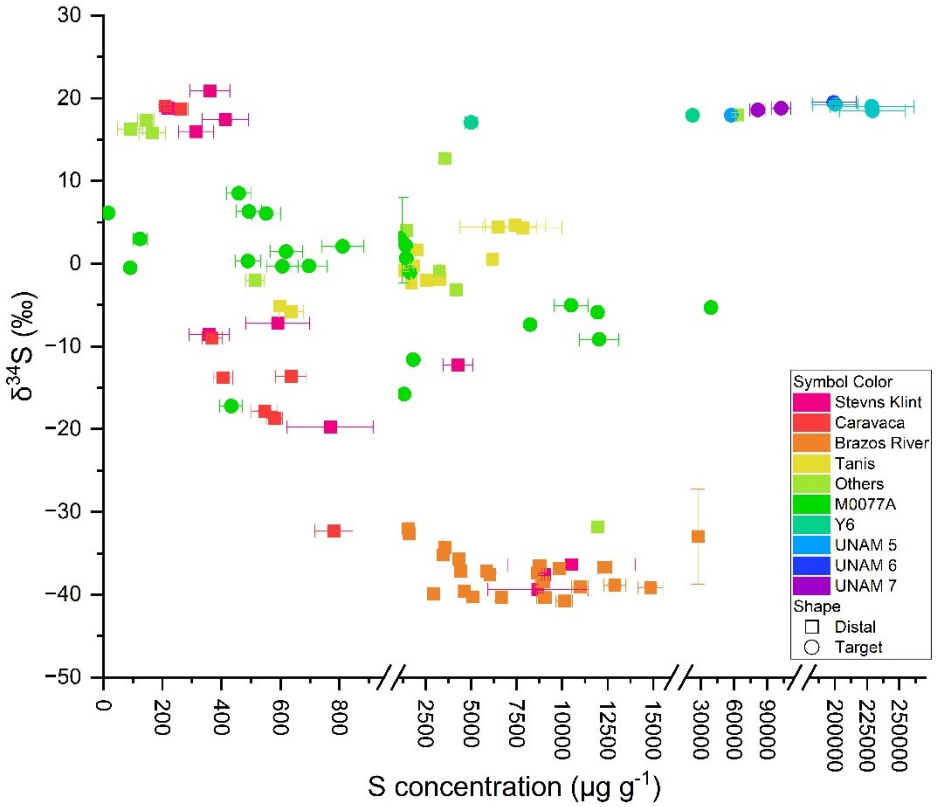

Fig. S2. Bulk S concentration and S isotope ratio, expressed as $\delta^{34}S$, for all the impact target drill cores and K-Pg distal sites analyzed. It is suggested that the onshore impact target drill cores (Y6, UNAM-5,6,7, and YAX-1) mostly have high S concentrations and $\delta^{34}S$ values, while the values for the offshore impact target drill core (M0077A) cover a wider range of values. The former indicates high amounts of anhydrite, consistent with lithological observations, and the latter indicates inclusion of many different S species. For the M0077A drill core, values with medium S concentrations and low $\delta^{34}S$ values indicate influence of pyrite sedimentation, occurring during microbial reduction, while low S concentrations and $\delta^{34}S$ values near to zero indicate the influence of igneous rock. Similar observations can be made for the distal sites, with the inclusion of low S concentration and high $\delta^{34}S$ values, which indicate inclusion of marine sulfate and/or anhydrite deposition.

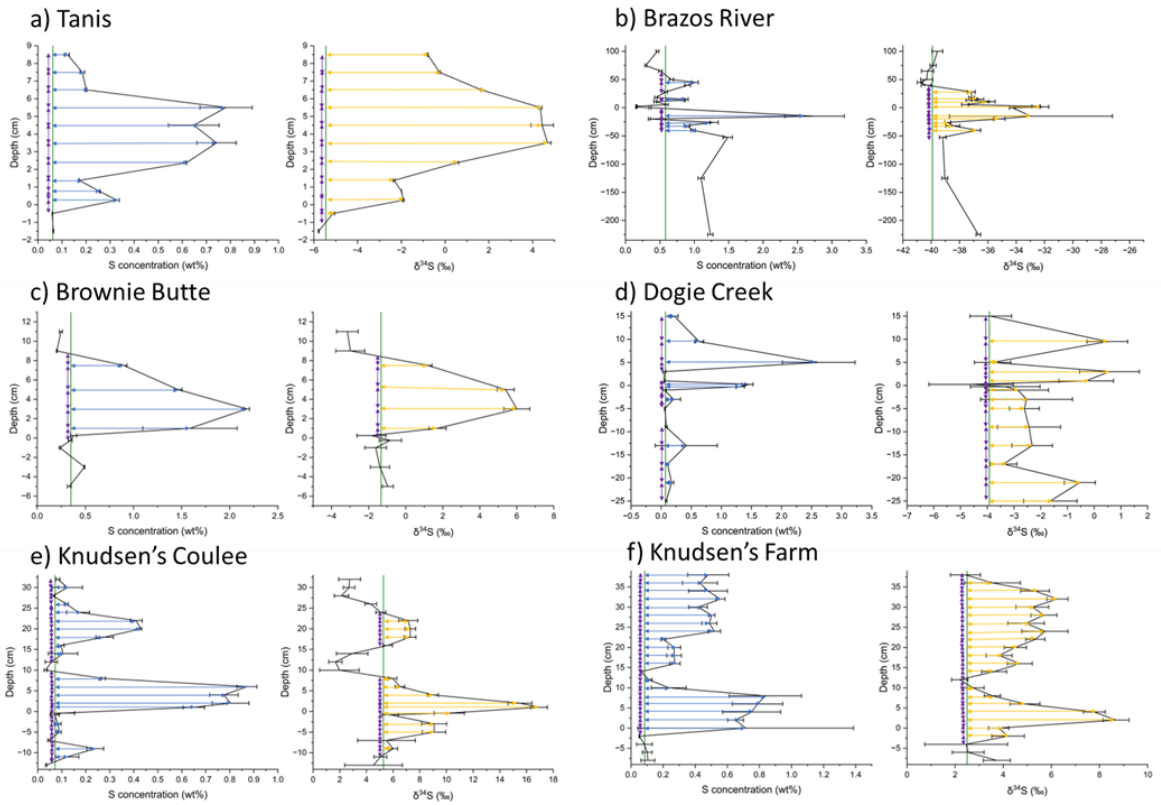

Fig. S3. Bulk S concentration (blue) and S isotope ratio, expressed as $\delta^{34}S$, (yellow) profiles in the **a)** Tanis (based on values obtained in this study), **b)** Brazos River (based on values obtained in this study), **c)** Brownie Butte (based on values obtained from a previously published study[34]), **d)** Dogie Creek (based on values obtained from a previous published study[34]), **e)** Knudsen's Coulee Section (based on values obtained from a previous study[35]), and **f)** Knudsen's Farm Section (based on values obtained from a previous study[35]) impact event deposit. The error bars for the concentration correspond to 2SD and for $\delta^{34}S$ to expanded uncertainty. The green lines indicate the background values before the impact event deposition for the site, the purple lines indicate the vertical thickness of each sample unit ($VL_{Per\ sample}$), and the blue and orange lines indicate background-corrected S concentration ($C_{K-Pg\_site\_deposit}$) and $\delta^{34}S$ values ($\delta^{34}S_{K-Pg\_site\_deposit}$), respectively, as a result of the deposition. These data are used for the mass balance calculation to estimate the amount of impact-vaporized S.

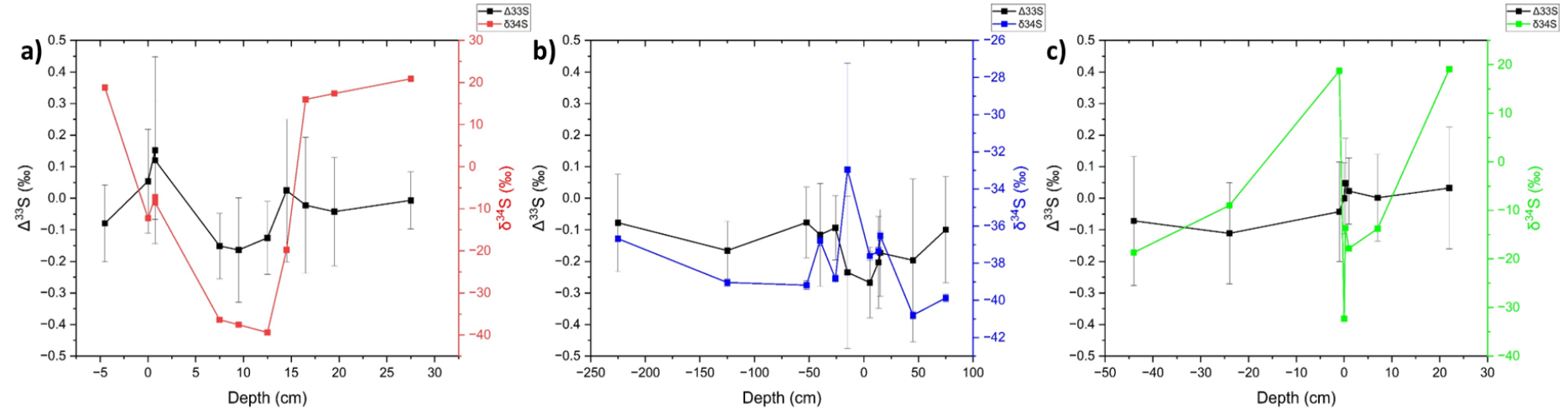

Fig. S4. Bulk $\delta^{34}S$ and $\Delta^{33}S$ (mass-independent fractionation tracer) in K-Pg boundary profiles at **a)** Stevns Klint (red), **b)** Brazos River (blue), and **c)** Caravaca (green) K-Pg deposition sites. Error bars represent the external uncertainty and are sometimes smaller than the markers.

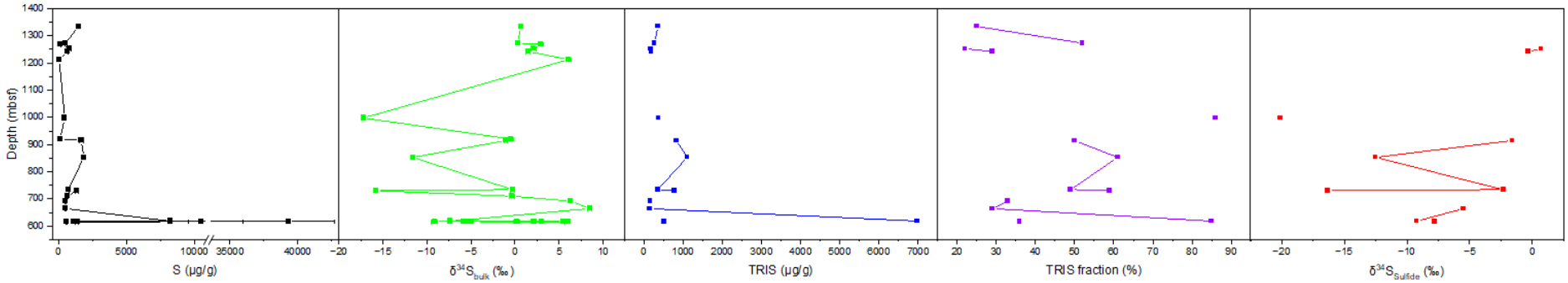

Fig. S5. Bulk S concentration (black), bulk $\delta^{34}S$ (green), total reduced inorganic S (TRIS, blue), TRIS-fraction (TRIS/bulk S concentration*100, violet), and sulfide-specific isotope ratio ($\delta^{34}S_{sulfide}$, red) profiles of the IODP-ICDP Expedition 364 M0077A drill core.

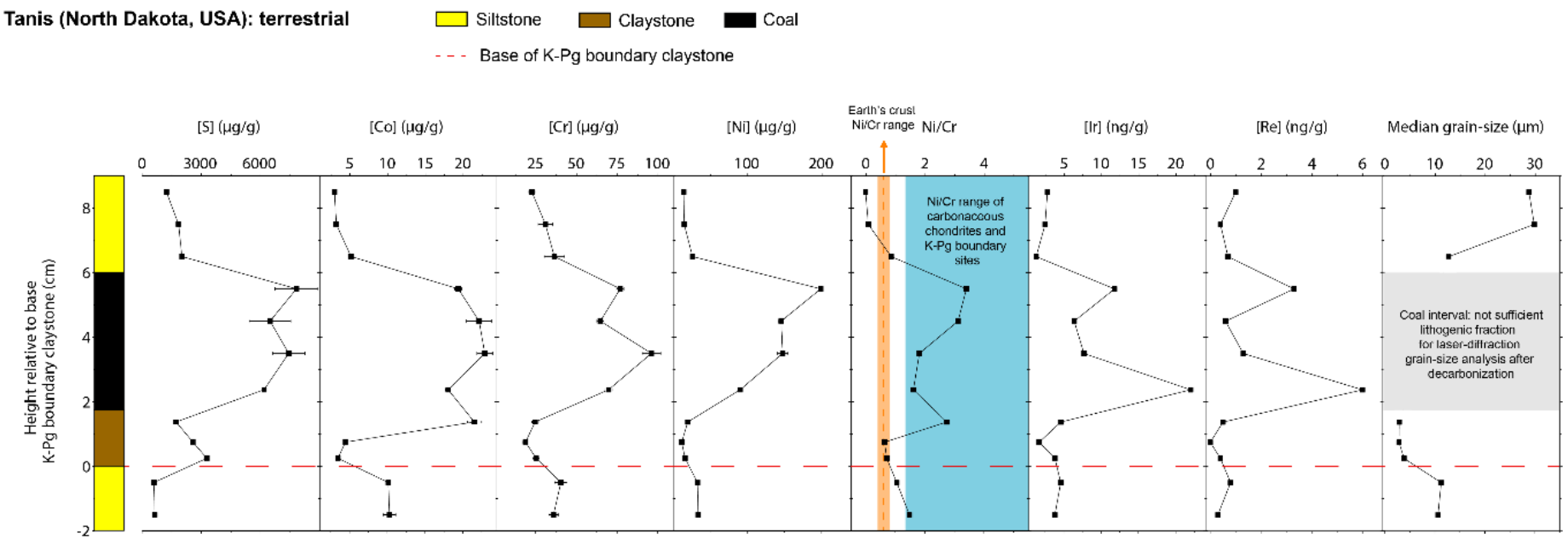

Fig. S6. Geochemistry and sedimentology of the Tanis K-Pg boundary site, showing bulk S, Co, Cr, and Ni concentrations; background subtracted Ni/Cr ratios; Ir and Re information values; and previously published[33] median grain-size values. Error bars represent the standard deviation for two or more replicates and are often smaller than the markers. The dashed red line represents the K-Pg boundary claystone equivalent, based on sedimentological constrains and microkrystitesand shocked minerals[36]. Typical Ni/Cr values for the upper continental (UCC) crust[29] are marked with an orange dashed line and the range is marked by an orange interval. The blue region marks the previously published range for Ni/Cr values from other K-Pg boundary sites and for carbonaceous chondrites[21,30,31]. The gray region for the median grain-size represents the Paleocene coal interval, where measurement points are missing as there was not a sufficient lithogenic fraction left for accurate laser-diffraction grain-size analysis after decarbonization[33].

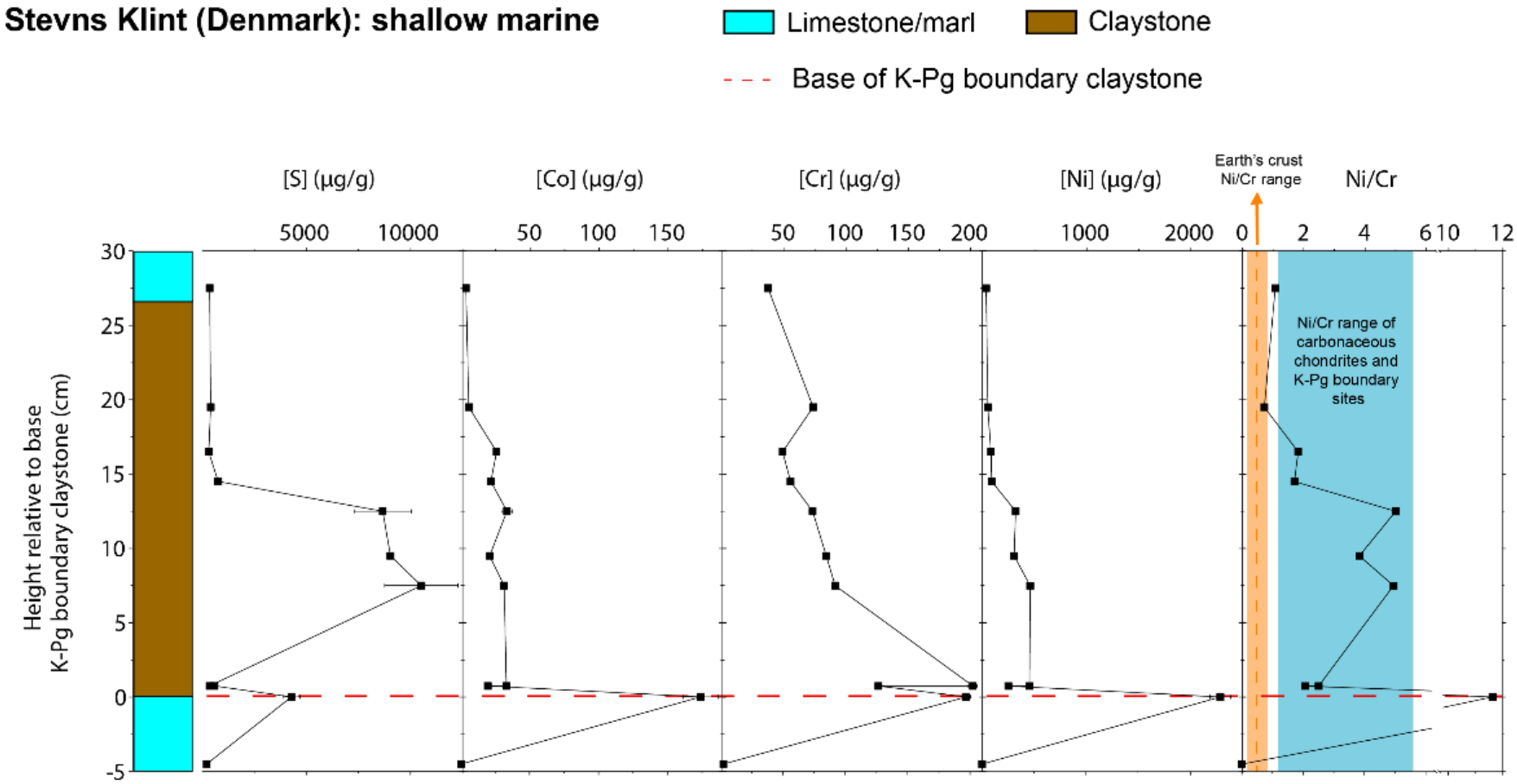

Fig. S7. Geochemistry of the Stevns Klint K-Pg boundary site, showing bulk S, Co, Cr, and Ni concentrations and background subtracted Ni/Cr ratios. Error bars represent the standard deviation for two or more replicates and are often smaller than the markers. The dashed red line represents the base of the K-Pg boundary claystone, based on the 'start' of the sedimentological criteria, the presence of microkrystites, and the previously measured Ir anomaly[16]. Typical Ni/Cr values for the upper continental (UCC) crust[29] are marked with an orange dashed line and the range is marked by an orange interval. The blue region marks the previously published range for Ni/Cr values from other K-Pg boundary sites and for carbonaceous chondrites[21,30,31].

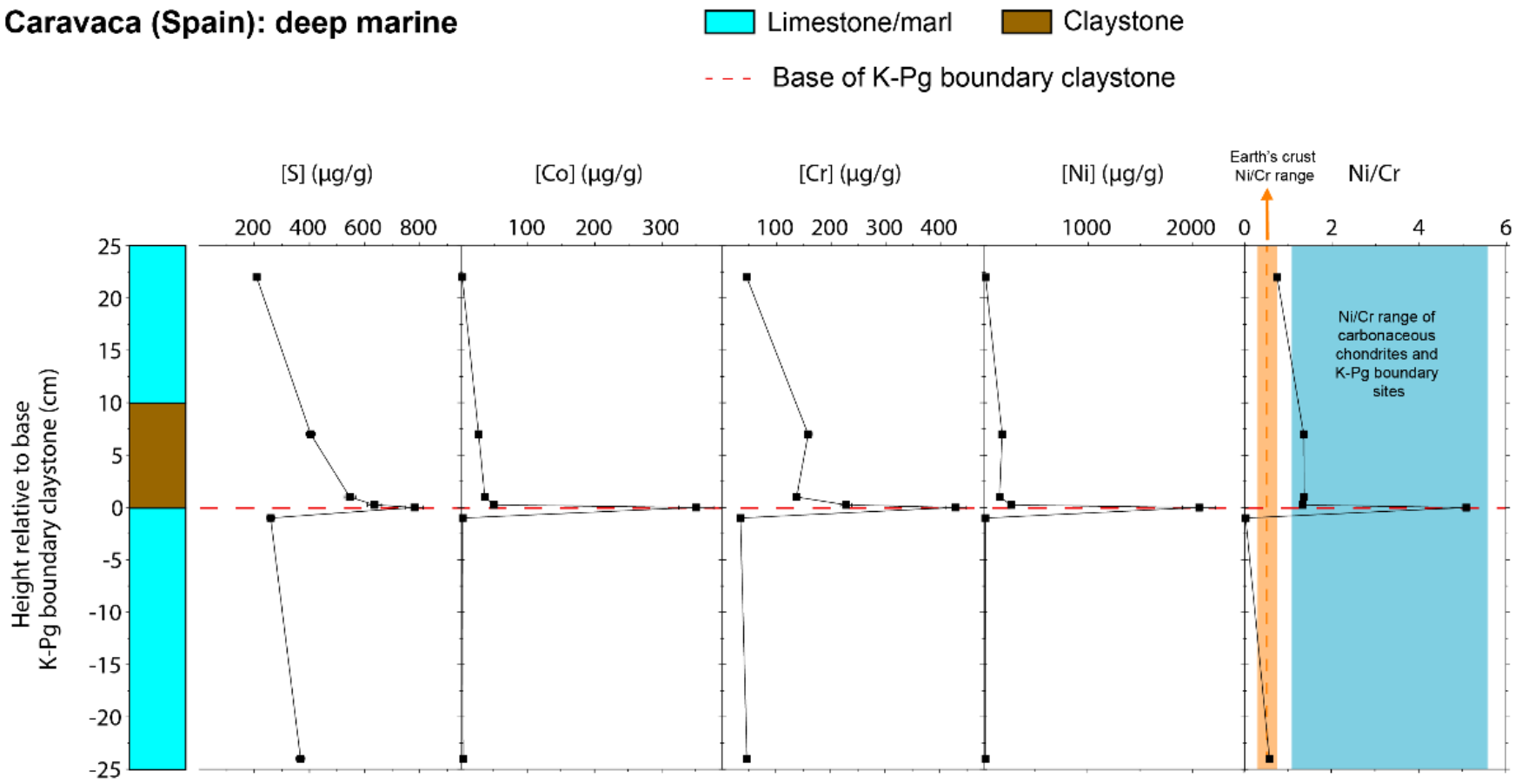

Fig. S8. Geochemistry of the Caravaca K-Pg boundary site, showing bulk S, Co, Cr, and Ni concentrations and background subtracted Ni/Cr ratios. Error bars represent the standard deviation for two or more replicates and are often smaller than the markers. The dashed red line represents the base of the K-Pg boundary claystone, based on the 'start' of the sedimentological criteria, the presence of microkrystites, and the previously measured Ir anomaly[16]. Typical Ni/Cr values for the upper continental (UCC) crust[29] are marked with an orange dashed line and the range is marked by an orange interval. The blue region marks the previously published range for Ni/Cr values from other K-Pg boundary sites and for carbonaceous chondrites[21,30,31].

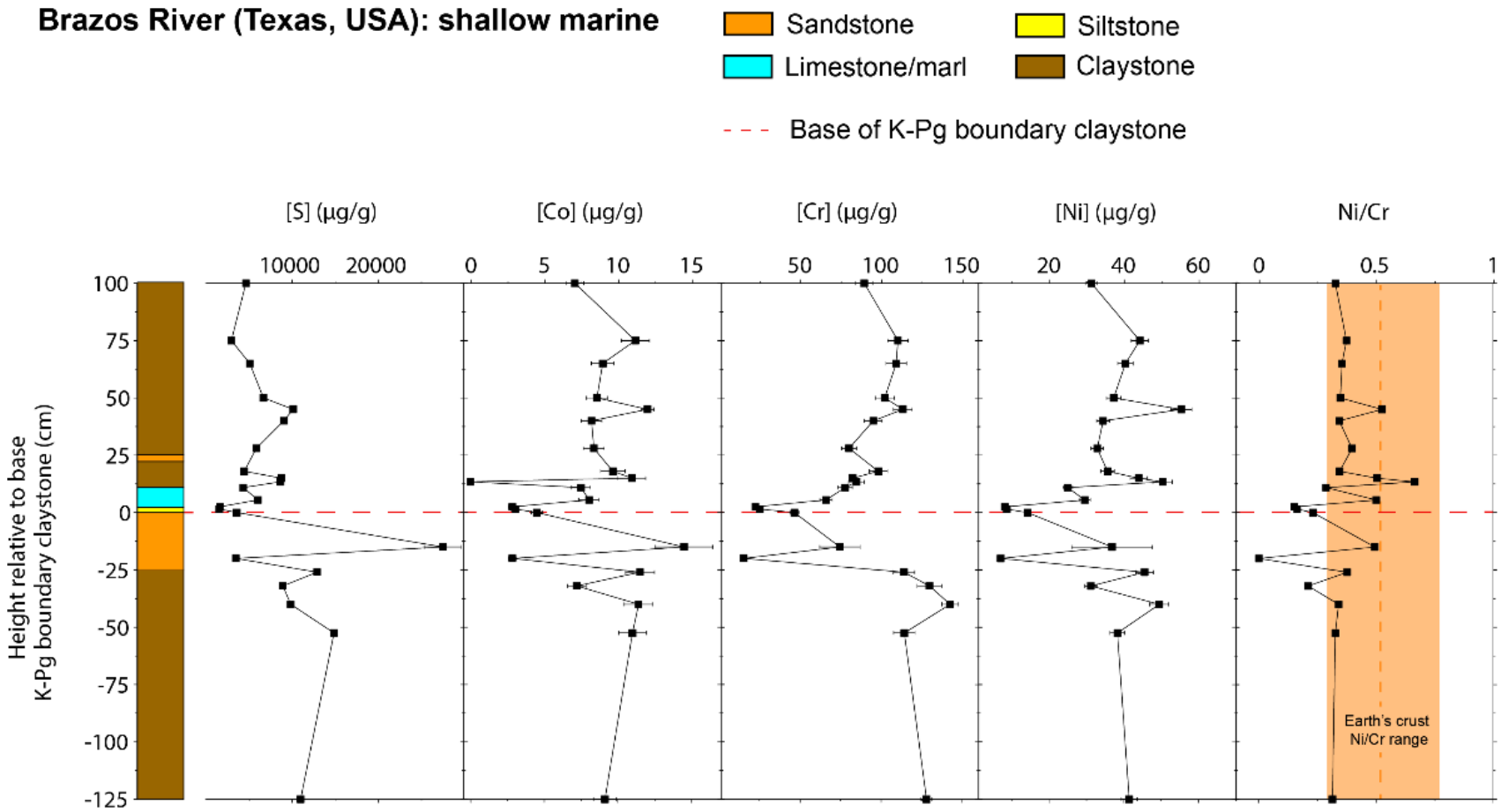

Fig. S9. Geochemistry of the Brazos River K-Pg boundary site, showing bulk S, Co, Cr, and Ni concentrations and background subtracted Ni/Cr ratios. Error bars represent the standard deviation for two or more replicates and are often smaller than the markers. The dashed red line represents the base of the K-Pg boundary claystone, based on the 'start' of the sedimentological criteria and the previously measured Ir anomaly[16]. Typical Ni/Cr values for the upper continental (UCC) crust[29] are marked with a orange dashed line and the range is marked by an orange interval.

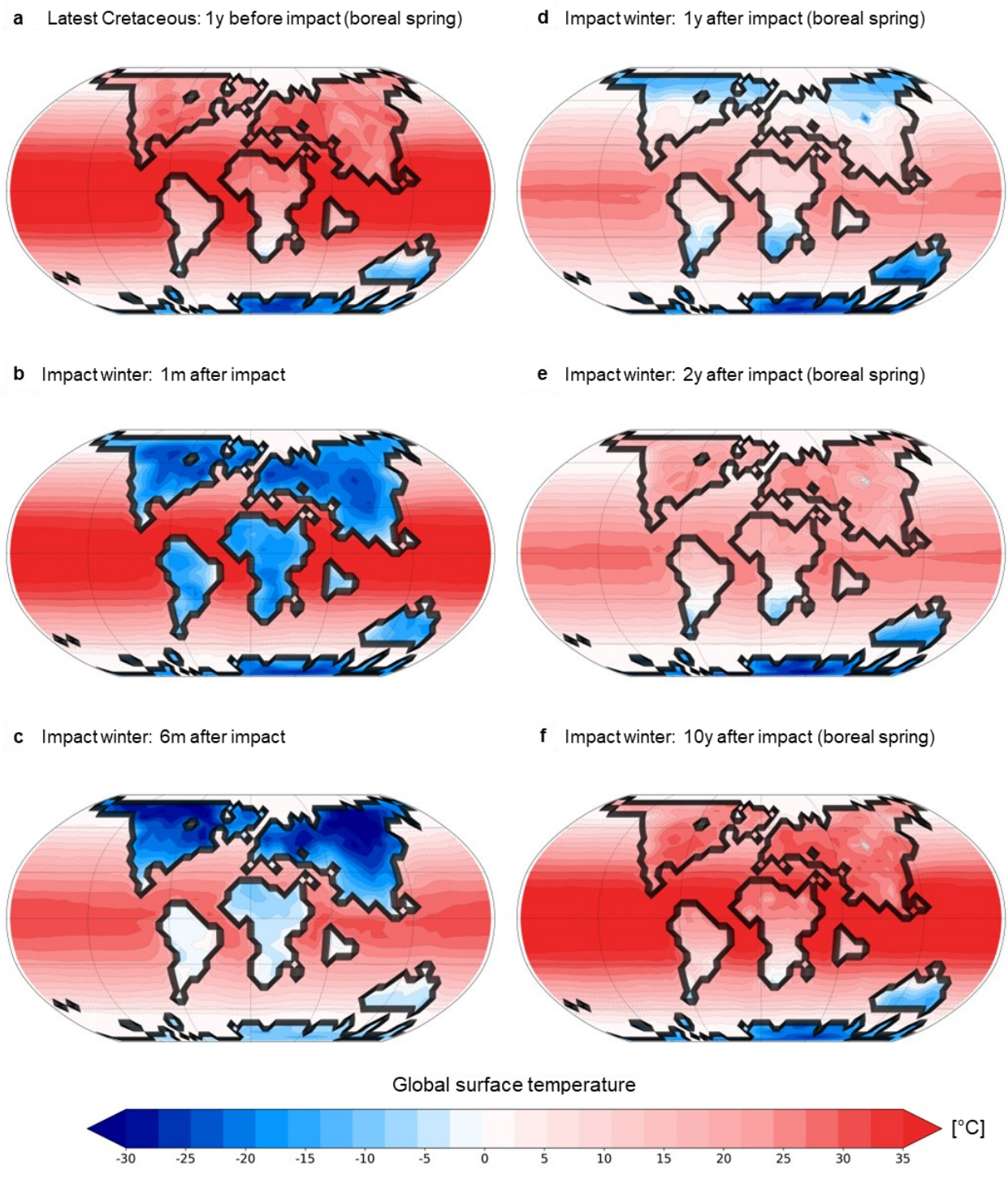

Fig. S10. Simulated global temperatures at different time points before and after the Chicxulub impact event, using the minimum estimate of 30 Gt of released S. The time points include: **a)** 1 year before impact as well as **b)** 1 month, **c)** 6 months, **d)** 1 year, **e)** 2 years, and **f)** 10 years after impact.

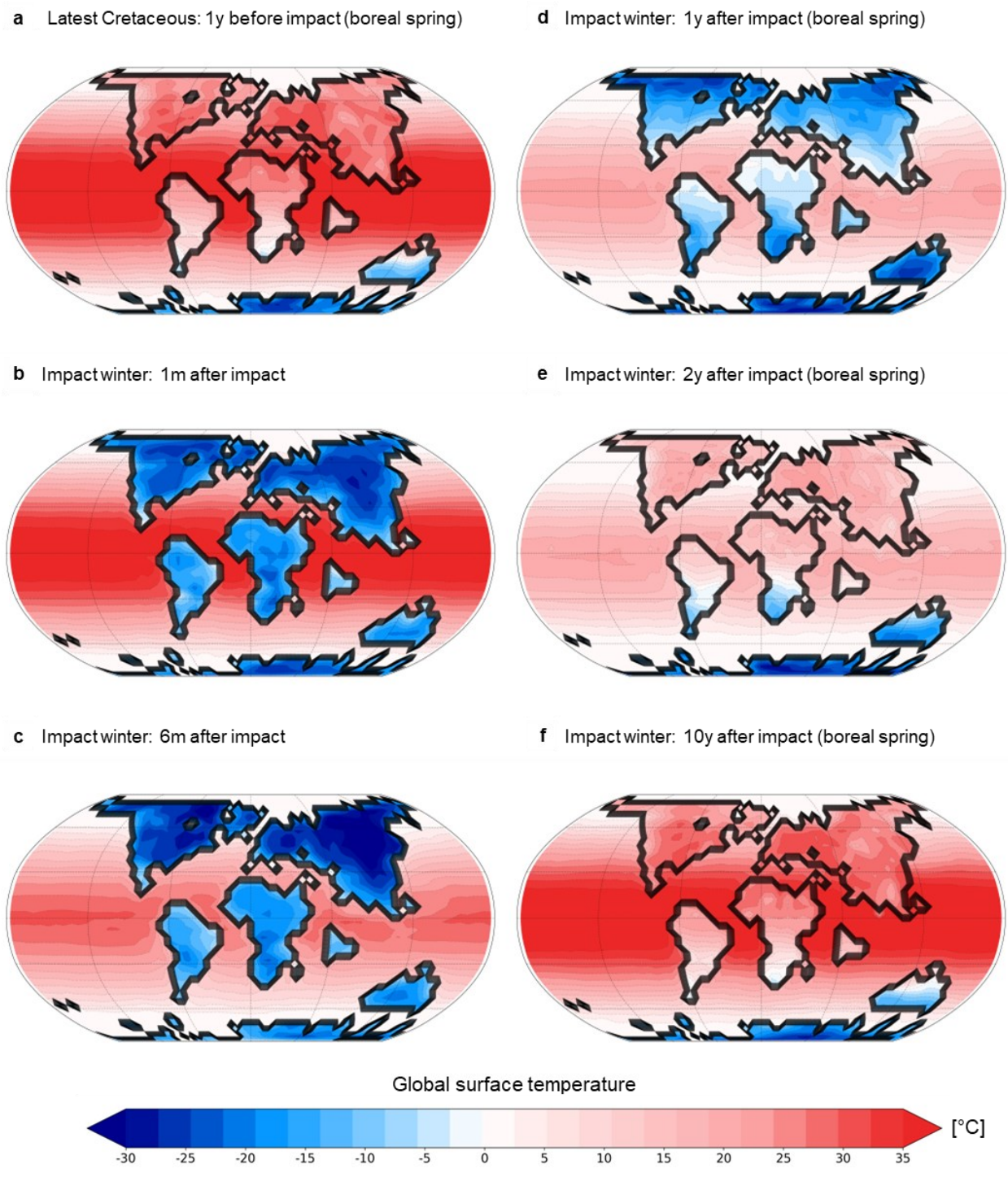

Fig. S11. Simulated global temperatures at different time points before and after the Chicxulub impact event, using the maximum estimate of 110 Gt of released S. The time points include: **a)** 1 year before impact as well as **b)** 1 month, **c)** 6 months, **d)** 1 year, **e)** 2 years, and **f)** 10 years after impact.

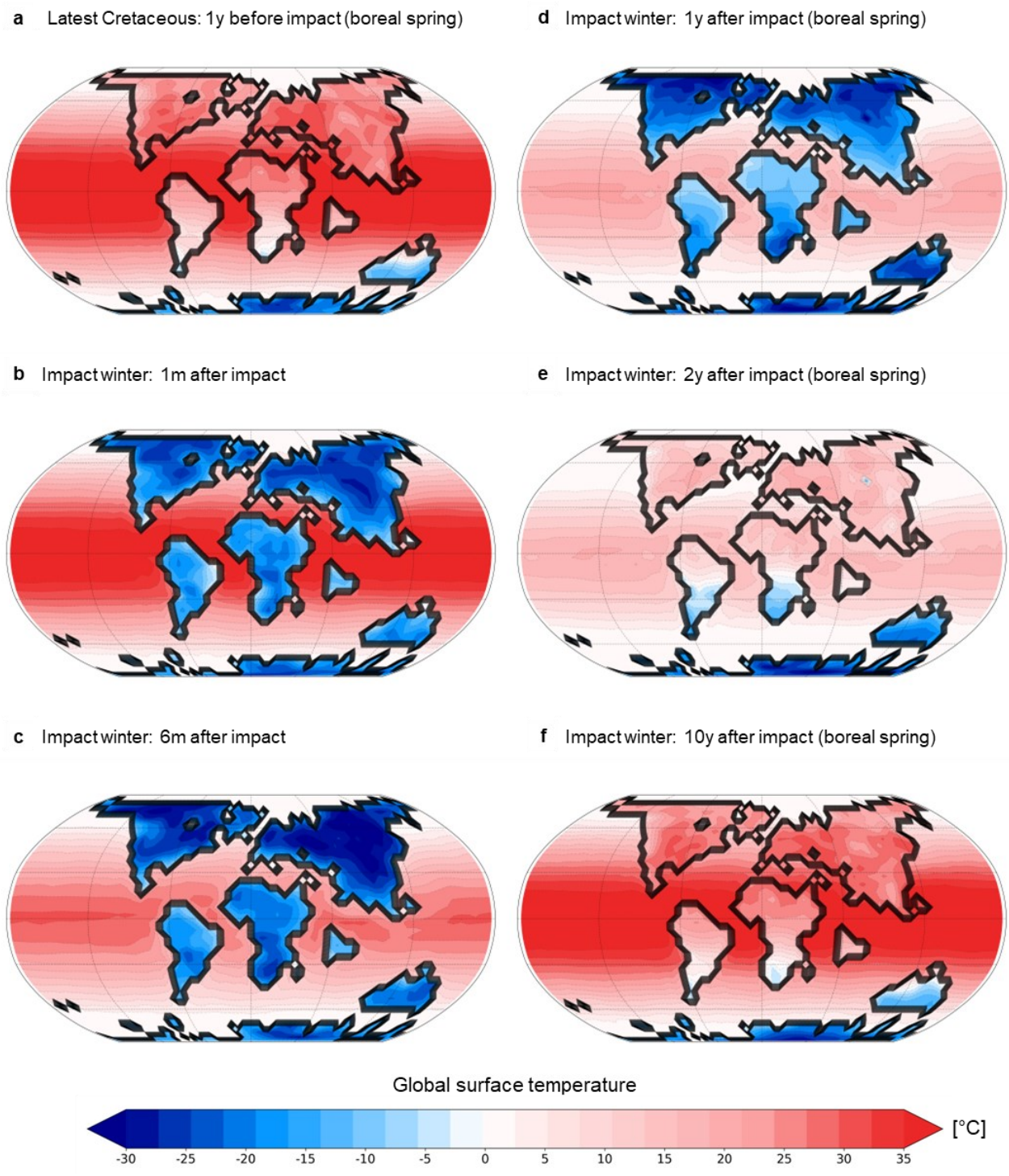

Fig. S12. Simulated global temperatures at different time points before and after the Chicxulub impact event, using the minimum value of 200 Gt for the recently simulated value from Artemieva *et al.*, 2017 (325 ± 130 Gt[24]). The time points include: **a)** 1 year before impact as well as **b)** 1 month, **c)** 6 months, **d)** 1 year, **e)** 2 years, and **f)** 10 years after impact.

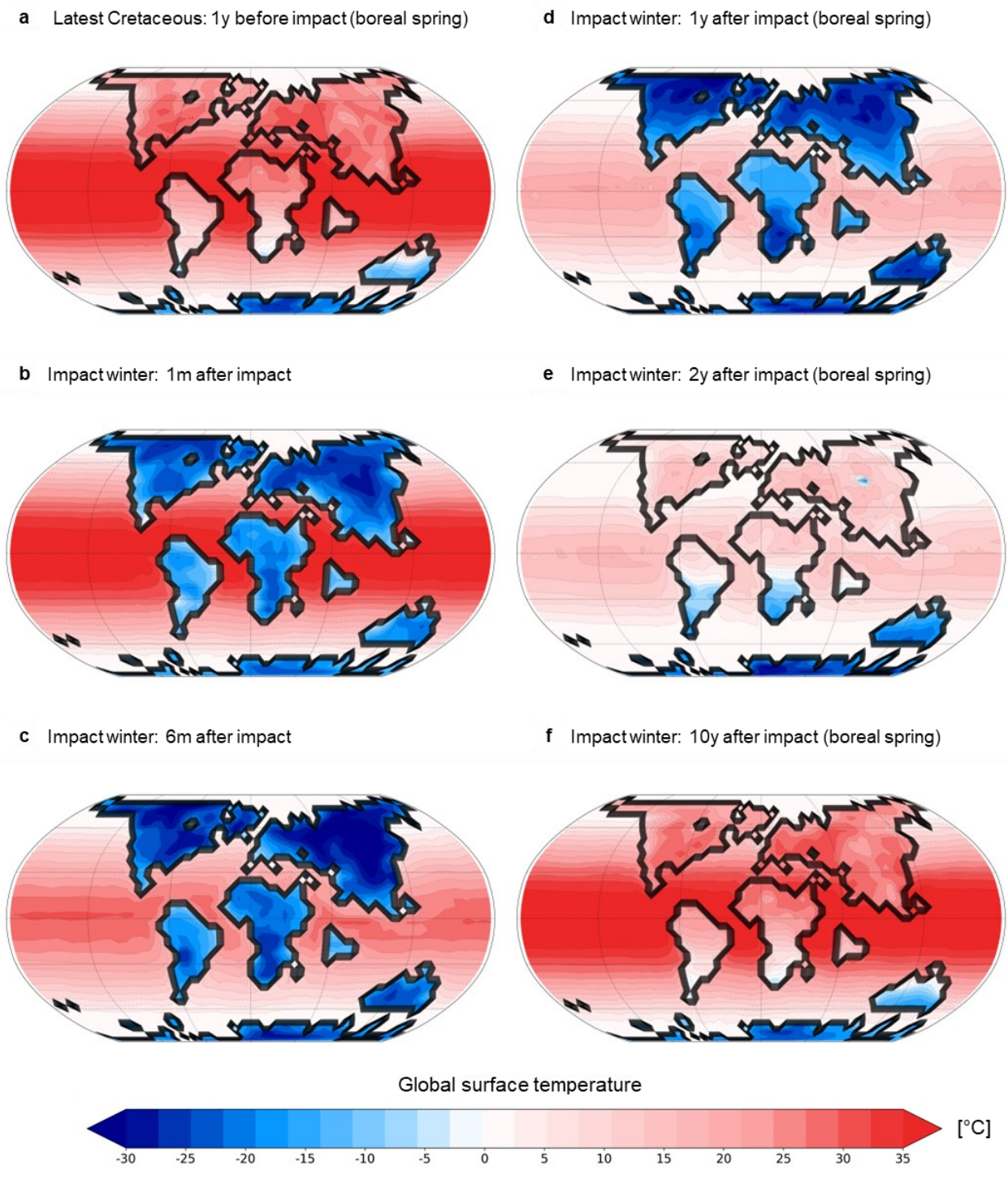

Fig. S13. Simulated global temperatures at different time points before and after the Chicxulub impact event, using the recently published estimate of 325 Gt of released S[37]. The time points include: **a)** 1 year before impact as well as **b)** 1 month, **c)** 6 months, **d)** 1 year, **e)** 2 years, and **f)** 10 years after impact.

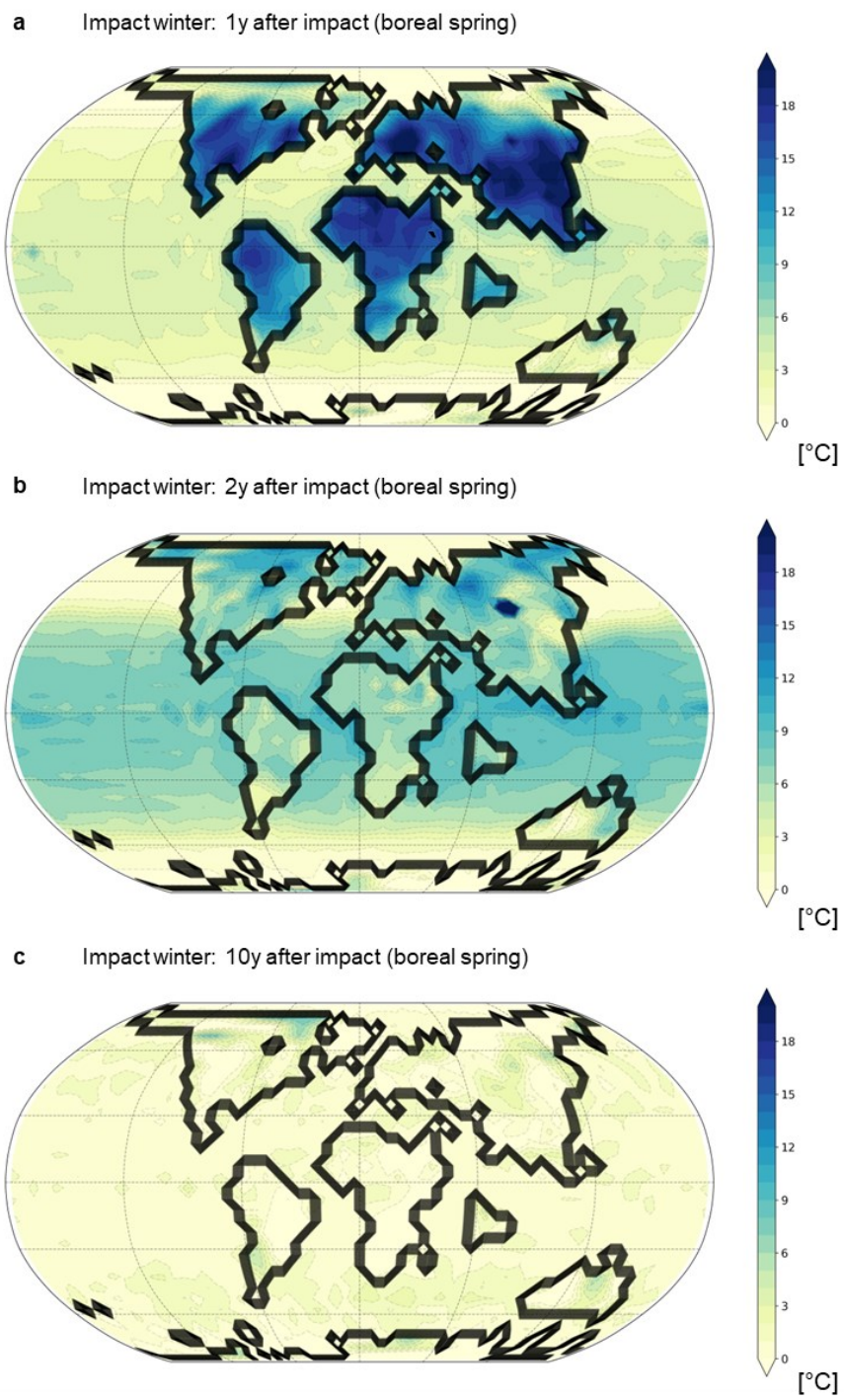

Fig. S14. Global surface temperature difference between simulations based on the previously published estimate of Chicxulub impact-released S of 325 Gt by Artemieva *et al.* 2017[37], and the average empirical estimate obtained in this study, based on 70 Gt of impact-released S, at **a)** 1, **b)** 2, and **c)** 10 years after the impact.

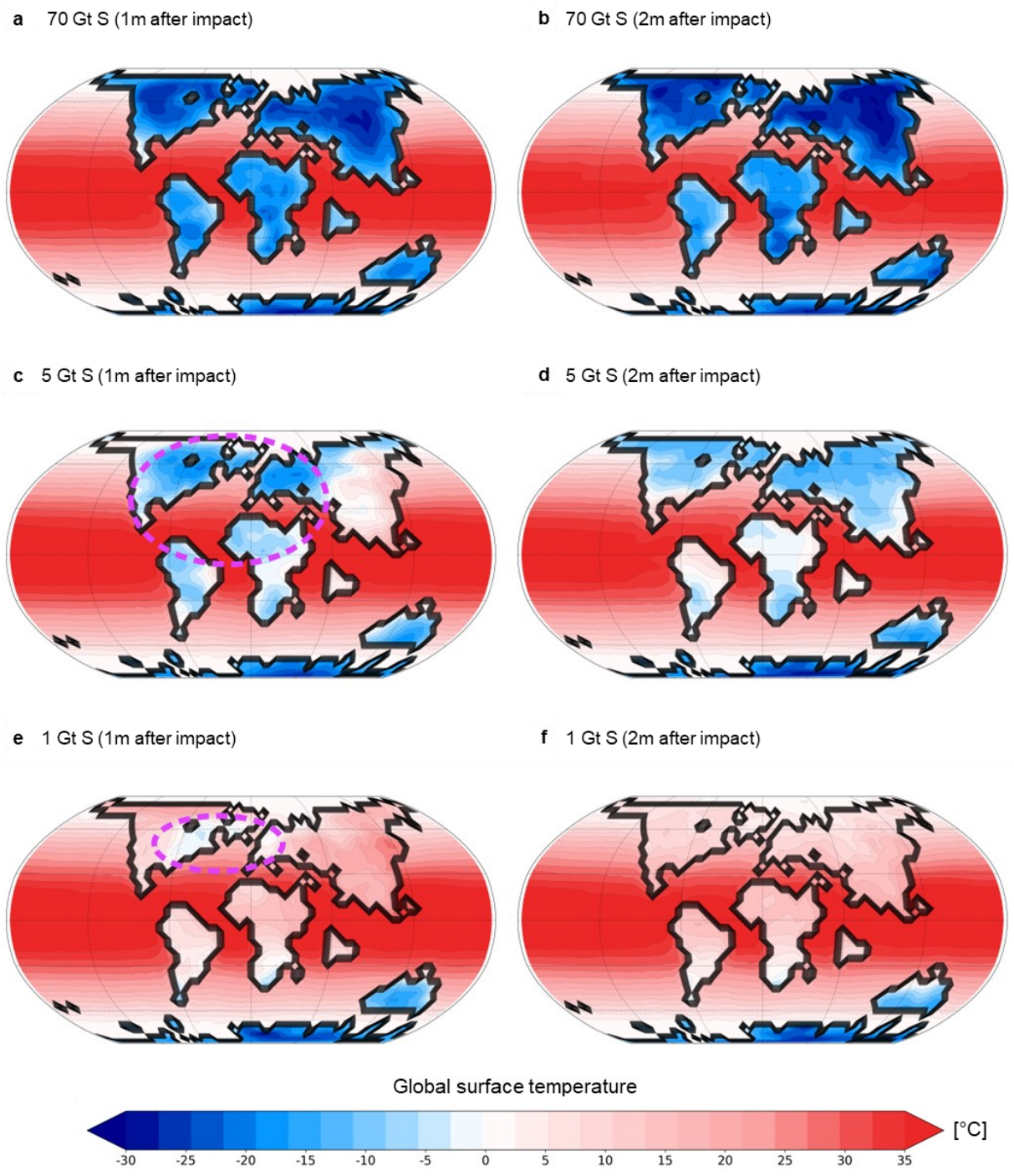

Fig. S15. Simulated global temperatures based on estimations of 70, 5, and 1 Gt impact-released S at **a)**, **b)**, and **c)** 1 and **d)**, **e)**, and **f)** 2 months after the Chicxulub impact event. For 70 Gt and 5 Gt of S, global cooling effects are observed, while only local cooling effects are observed for 1 Gt (pink dashed circle). The threshold for global effects is therefore estimated to be between 1-5 Gt of released S.

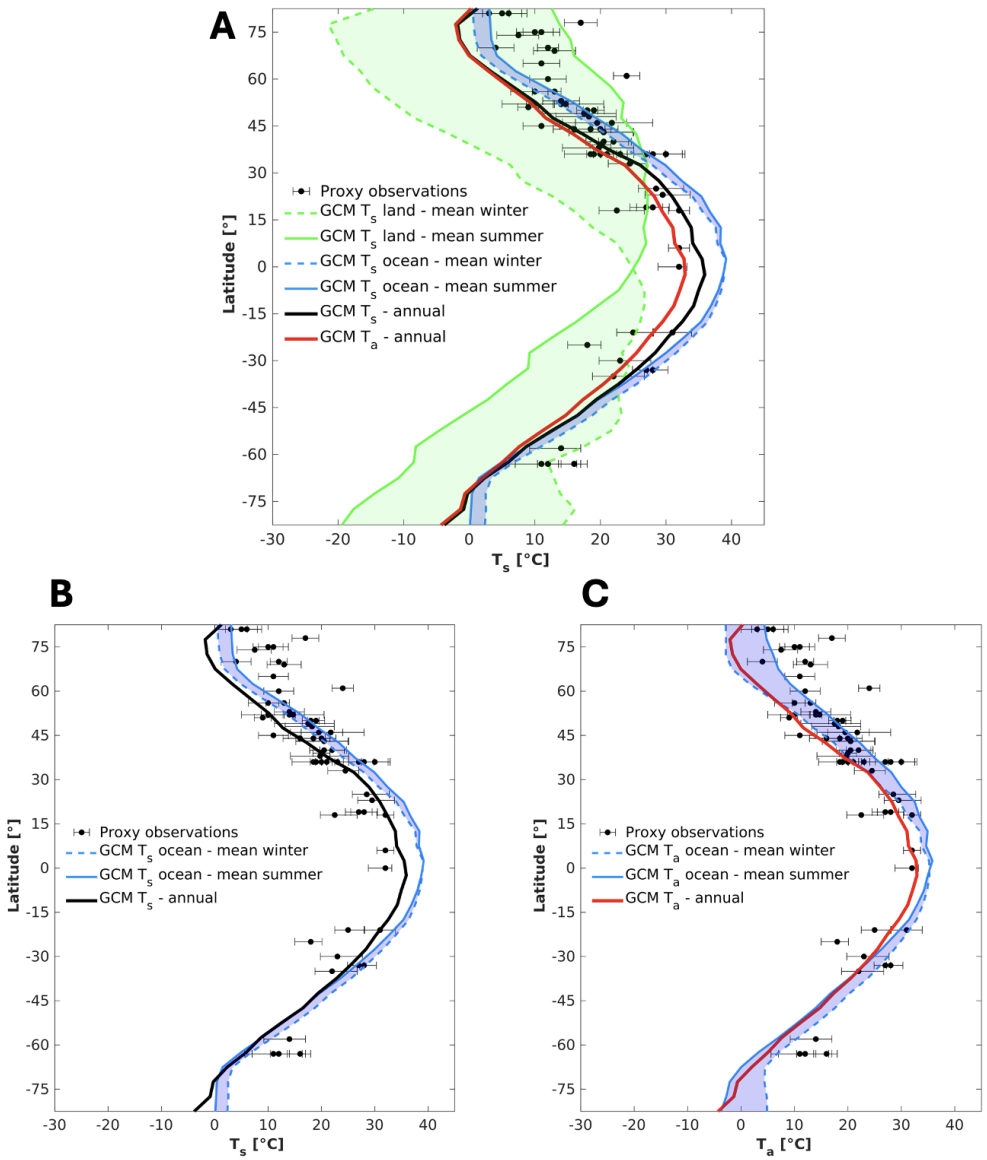

Fig. S16. Late Cretaceous model-proxy comparison a Modeled surface temperatures (T_s) on lands and oceans one year before impact are compared with Late Cretaceous proxy observations[38] as presented in Senel *et al.* 2023[33]. To evaluate the response of surface air temperature at 2 meters (T_a), the pre-impact annual mean of T_a is appended to the same figure[33] by a solid red line. **b** same as **a**, but only the ocean surface temperatures (T_s). **c** same as **a**, but only the ocean surface air temperature at 2 meters (T_a). Note that proxy data are displayed by black circles and horizontal error bars. Green solid and dashed lines show zonal means of modeled land temperatures in the boreal summer and winter seasons. Blue solid (boreal summer) and dashed (boreal winter) lines display zonal means of modeled ocean temperatures.

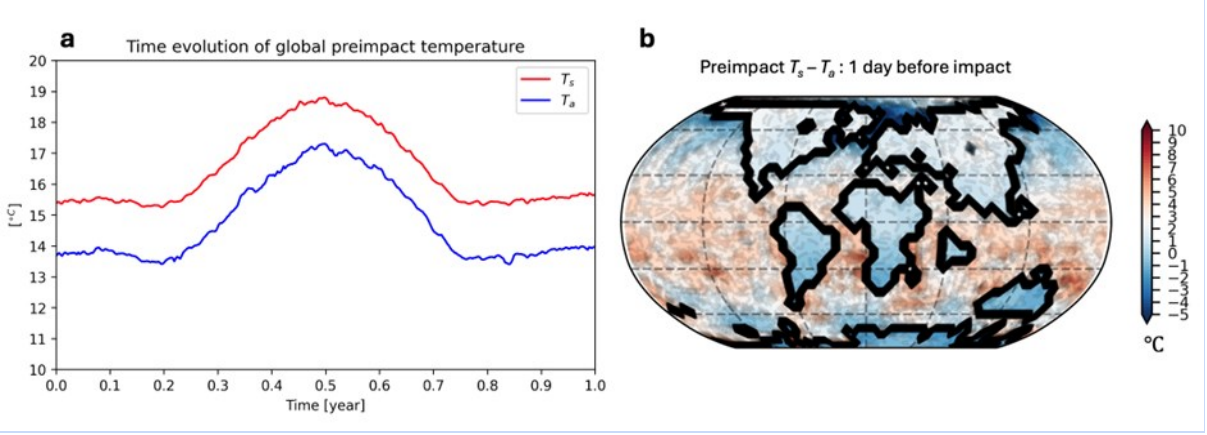

Fig. S17. a Global average surface temperatures (T_s) and (T_a) for the year before impact. **b** The difference between T_s and T_a, 1 day before impact.

References

Paytan, A. & Gray, E. T. Sulfur isotope stratigraphy. in *The Geologic Time Scale 2012* (eds. Gradstein, F. M., Ogg, J. G., Schmitz, M. & Ogg, G.) 167–180 (Elsevier B.V., 2012). doi:10.1016/B978-0-444-59425-9.00009-3.

Strauss, H. & Deutsch, A. The Chicxulub event—sulfur-bearing minerals and lithologies. *Gephysical Research Abstracts* **5**, (2003).

Paytan, A., Kastner, M., Campbell, D. & Thiemens, M. H. Seawater Sulfur Isotope Fluctuations in the Cretaceous. *Science* **304**, 1663–1665 (2004).

Gulick, S. P. S. *et al.* The first day of the Cenozoic. *Proc Natl Acad Sci U S A* **116**, 19342–19351 (2019).

Kaskes, P. *et al.* Formation of the crater suevite sequence from the Chicxulub peak ring: A petrographic, geochemical, and sedimentological characterization. *Bulletin of the Geological Society of America* **134**, 895–927 (2022).

Schaefer, B. *et al.* Microbial life in the nascent Chicxulub crater. *Geology* **48**, 328–332 (2020).

Kring, D. A., Whitehouse, M. J. & Schmieder, M. Microbial Sulfur Isotope Fractionation in the Chicxulub Hydrothermal System. *Astrobiology* **21**, 103–114 (2021).

Kring, D. A. *et al.* Probing the hydrothermal system of the Chicxulub impact crater. *Sci. Adv* **6**, 3053–3082 (2020).

Wang, W. *et al.* Sulfur isotopic signature of Earth established by planetesimal volatile evaporation. *Nat Geosci* **14**, 806–811 (2021).

Labidi, J., Cartigny, P. & Moreira, M. Non-chondritic sulphur isotope composition of the terrestrial mantle. *Nature* **501**, 208–211 (2013).

Labidi, J., Cartigny, P., Hamelin, C., Moreira, M. & Dosso, L. Sulfur isotope budget (32S, 33S, 34S and 36S) in Pacific-Antarctic ridge basalts: A record of mantle source heterogeneity and hydrothermal sulfide assimilation. *Geochim Cosmochim Acta* **133**, 47–67 (2014).

Labidi, J. & Cartigny, P. Negligible sulfur isotope fractionation during partial melting: Evidence from Garrett transform fault basalts, implications for the late-veneer and the hadean matte. *Earth Planet Sci Lett* **451**, 196–207 (2016).

Kring, D. A. Hypervelocity collisions into continental crust composed of sediments and an underlying crystalline basement: Comparing the Ries (~24 km) and Chicxulub (~180 km) impact craters. *Chemie der Erde* **65**, 1–46 (2005).

Junium, C. K. *et al.* Massive perturbations to atmospheric sulfur in the aftermath of the Chicxulub impact. *PNAS* **119**, 1–7 (2022).

Goderis, S. *et al.* Globally distributed iridium layer preserved within the Chicxulub impact structure. *Sci Adv* **7**, 1–13 (2021).

Smit, J. The global stratigraphy of the Cretaceous-Tertiary boundary impact ejecta. *Annu. Rev. Earth Planet. Sci* **27**, 75–113 (1999).

Lin, M. *et al.* Five-S-isotope evidence of two distinct mass-independent sulfur isotope effects and implications for the modern and Archean atmospheres. *Proc Natl Acad Sci U S A* **115**, 8541–8546 (2018).

Endo, Y., Danielache, S. O. & Ueno, Y. Total Pressure Dependence of Sulfur Mass-Independent Fractionation by SO 2 Photolysis. *Geophys Res Lett* **46**, 483–491 (2019).

Glasspool, I. J. & Scott, A. C. Phanerozoic concentrations of atmospheric oxygen reconstructed from sedimentary charcoal. *Nat Geosci* **3**, 627–630 (2010).

Vellekoop, J. *et al.* Shelf hypoxia in response to global warming after the Cretaceous- Paleogene boundary impact. *Geology* **46**, 683–686 (2018).

Goderis, S. *et al.* Reevaluation of siderophile element abundances and ratios across the Cretaceous-Paleogene (K-Pg) boundary: Implications for the nature of the projectile. *Geochim Cosmochim Acta* **120**, 417–446 (2013).

Rocchia, R., Robin, E., Froget, L. & Gayraud, J. Stratigraphic distribution of extraterrestrial markers at the Cretaceous-Tertiary boundary in the Gulf of Mexico area: Implications for the temporal complexity of the event. *Geological Society of America Special Paper* **307**, 279–286 (1996).

Asaro, F. *et al.* Iridium and other geochemical profiles near the Cretaceous-Tertiary boundary in a Brazos river section in Texas. in *exas ostracoda, International Symposium on Ostracoda, 8th, Guidebook of Excursion and Related Papers* (ed. Maddocks, R. F.) 238–241 (University of Houston, Houston, 1982).

Ganapathy, R., Gartner, S. & Jiang, M. Iridium anomaly at the Cretaceous-Tertiary boundary in Texas. *Earth Planet Sci Lett* **54**, 393–396 (1981).

Heymann, D. *et al.* Geochemical markers of the Cretaceous-Tertiary boundary event at Brazos River, Texas, USA. (1998).

Gertsch, B., Keller, G., Adatte, T. & Berner, Z. Platinum Group Element (PGE) Geochemistry of Brazos Sections, Texas, U.S.A. in *The End-Cretaceous Mass Extinction and the Chicxulub Impact in Texas. Special Publication 100* (eds. Keller, G. & Adatte, T.) 227–249 (SEPM (Society for Sedimentary Geology), 2011). doi:10.2110/sepmsp.100.227.

Premović, P. I., Ilić, B. S. & Dordević, M. G. Iridium anomaly in the Cretaceous-Paleogene boundary at Højerup (Stevns Klint, Denmark) and Woodside Creek (New Zealand): The question of an enormous proportion of extraterrestrial component. *Journal of the Serbian Chemical Society* **77**, 247–255 (2012).

Schmitz, B., Andersson, P. & Dahl, J. Iridium, sulfur isotopes and rare earth elements in the Cretaceous-Tertiary boundary clay at Stevns Klint, Denmark. *Geoehimica et Cosmochimica Acta* **52**, 229–236 (1988).

Rudnick, R. L. & Gao, S. Composition of the Continental Crust. in *Treatise on Geochemistry* (eds. Holland, H. D. & Turekian, K. K.) 1–64 (Elsevier-Pergamon, Oxford, 2003). doi:10.1016/B0-08-043751-6/03016-4.

Ritter, X., Deutsch, A., Berndt, J. & Robin, E. Impact glass spherules in the Chicxulub K-Pg event bed at Beloc, Haiti: Alteration patterns. *Meteorit Planet Sci* **50**, 418–432 (2015).

Tagle, R. & Berlin, J. A database of chondrite analyses including platinum group elements, Ni, Co, Au, and Cr: Implications for the identification of chondritic projectiles. *Meteorit Planet Sci* **43**, 541–559 (2008).

Desch, S., Jackson, A., Noviello, J. & Anbar, A. The Chicxulub impactor: comet or asteroid? *Astronomy & Geophysics* **62**, 3.34-3.37 (2021).

Senel, C. B. *et al.* Chicxulub impact winter sustained by fine silicate dust. *Nat Geosci* (2023) doi:10.1038/s41561-023-01290-4.

Maruoka, T., Koeberl, C., Newton, J., Gilmour, I. & Bohor, B. F. Sulfur isotopic compositions across terrestrial Cretaceous-Tertiary boundary successions. *Geological Society of America* **Special Paper 356**, 337–344 (2002).

Cousineau, M. L. Tracing biogeochemical processes using sulfur stable isotopes: two novel applications. (University of Ottawa, Ottawa, Ontario, 2013).

DePalma, R. A. *et al.* A seismically induced onshore surge deposit at the KPg boundary, North Dakota. *Proc Natl Acad Sci U S A* **116**, 8190–8199 (2019).

Artemieva, N., Morgan, J. & Expedition 364 Science Party. Quantifying the Release of Climate-Active Gases by Large Meteorite Impacts With a Case Study of Chicxulub. *Geophys Res Lett* **44**, 10,180-10,188 (2017).

Upchurch, G. R., Kiehl, J., Shields, C., Scherer, J. & Scotese, C. Latitudinal temperature gradients and high-latitude temperatures during the latest Cretaceous: Congruence of geologic data and climate models. *Geology* **43**, 683–686 (2015).